Centro de Investigación Científica y de Educación Superior de Ensenada, Baja California

Maestría en Ciencias
en Óptica con orientación en Optoelectrónica

Study of antireflective coatings for optical communications

Tesis
para cubrir parcialmente los requisitos necesarios para obtener el grado de Maestro en Ciencias

Presenta:

Germán Nolasco Jáuregui

Ensenada, Baja California, México
2020

Tesis defendida por

Germán Nolasco Jáuregui

y aprobada por el siguiente Comité

Dr. Heriberto Márquez Becerra	**Dr. Karl William Koch**
Codirector de tesis	Codirector de tesis

Miembros del comité

Dra. Carolina Álvarez Delgado

Dra. Alma Georgina Navarrete Alcalá

Dr. Horacio Soto Ortiz

Dr. Javier Alonso López Medina

Dr. Israel Rocha Mendoza
Coordinador del Posgrado en Óptica

Dra. Rufina Hernández Martínez
Directora de Estudios de Posgrado

Germán Nolasco Jáuregui © 2020
Queda prohibida la reproducción parcial o total de esta obra sin el permiso formal y explícito del autor y director de la tesis.

Resumen de la tesis que presenta **Germán Nolasco Jáuregui** como requisito parcial para la obtención del grado de Maestro en Ciencias en Óptica con orientación en Optoelectrónica.

Estudio de películas antirreflectoras para comunicaciones ópticas

Resumen aprobado por:

_____	_____
Dr. Heriberto Márquez Becerra	**Dr. Karl William Koch**
Codirector de tesis	Codirector de tesis

Los recubrimientos antirreflectores (AR) llevan décadas siendo ampliamente estudiados debido a su importancia tecnológica en numerosas aplicaciones, incluyendo microelectrónica, comunicaciones, celdas solares, etc. Este trabajo presenta un estudio completo de los recubrimientos AR: desde su teoría, diseño, simulación, fabricación y su caracterización. Un concepto fundamental en el funcionamiento de los recubrimientos AR es el contraste entre los índices de refracción de los materiales que componen a éstos. Con respecto a la fabricación, este contraste se puede obtener evaporando diferentes materiales o manipulando la estequiometría del material evaporado. Esta tesis explora ambos. Para el primero, se fabricó en las instalaciones de Corning Reynosa un diseño antirreflector de banda ancha de cuatro capas para el rango de 1200 a 1600 nm, utilizando Nb_2O_5 y SiO_2 como materiales fuente mediante la técnica de Depósito Asistido por Haz de Iones (IBAD, por sus siglas en inglés). Por otro lado, en el laboratorio de películas delgadas del CICESE, se utilizaron por primera vez películas delgadas de SiO_x ($1 < x < 2$) en recubrimientos antirreflectores de doble y triple capa para la línea de comunicaciones ópticas de 850nm. Al modificar la atmósfera, la velocidad de deposición o el vacío en la cámara al evaporar el monóxido de silicio mediante la técnica de evaporación térmica, se obtiene un rango de índices de refracción desde 1.47 hasta 1.92. Las películas delgadas de SiO_x se han estudiado ampliamente pero no se habían utilizado con fines antirreflectivos. Después de la caracterización óptica de las muestras mediante elipsometría y espectrofotometría, se concluyó que las películas delgadas de SiO_x ofrecen un buen rendimiento óptico (reflectividad), mas no mecánico (adhesión, densidad de empaquetamiento, etc.), ocasionado muy probablemente por la naturaleza misma de la técnica de evaporación térmica. Por esta razón, se prefieren los métodos energéticos como IBAD para obtener recubrimientos antirreflectores de alta calidad. IBAD ofreció una deposición rápida, repetible y con una baja temperatura del sustrato, que son algunos de los requerimientos actuales para el mercado de recubrimientos antirreflectores para comunicaciones ópticas.

Palabras clave: Películas delgadas antirreflectoras, evaporación térmica, Depósito Asistido por Iones, comunicaciones ópticas, películas delgadas de SiO_x.

Abstract of the thesis presented by **Germán Nolasco Jáuregui** as a partial requirement to obtain the Master of Science degree in Optics with orientation in Optoelectronics.

Study of antireflective coatings for optical communications

Abstract approved by:

_____	_____
Dr. Heriberto Márquez Becerra	**Dr. Karl William Koch**
Codirector de tesis	Codirector de tesis

Antireflective (AR) coatings have been widely studied due to their technological importance in numerous applications, including microelectronics, optical telecommunications, solar cells, etc. This work presents a complete study of AR coatings, including their theory, design, simulation, synthesis, and characterization. An essential subject in the operation of AR coatings is the contrast between the refractive indices of the materials used to make the layers of the coatings. Regarding synthesis, this contrast can be obtained either by evaporating different source materials or by manipulating the stoichiometry of the evaporated material. This thesis explores both fabrication approaches. For the former, a four-layer broadband AR design for the range from 1200 to 1600nm was fabricated at Corning Reynosa facilities using Nb_2O_5 and SiO_2 as source materials by Ion Beam Assisted Deposition (IBAD) technique. On the other hand, at the Thin-Films laboratory at CICESE, the application of SiO_x ($1 < x < 2$) thin-films on double- and triple-layer antireflective coatings designs for optical communications wavelength of 850nm was used for the very first time. Manipulation of the atmosphere, deposition rate, or the vacuum level in the chamber while evaporation of silicon monoxide by thermal evaporation technique can produce a range of refractive indices from 1.47 to 1.92. SiO_x thin films have been widely studied but not used for antireflective purposes. After optical characterization of the samples by ellipsometry and spectrophotometry, was conclude that SiO_x thin-films offer a good optical (reflectivity), but no mechanical (adhesion, packing density, etc.) AR performance, most probably due to the nature of the thermal evaporation technique. For this reason, energetic methods like IBAD are preferred to get high-quality antireflective coatings. IBAD offered rapid, repeatable, and low- substrate temperature deposition, which are some of the current requirements for the market of antireflective coatings for optical communications.

Keywords: Antireflective thin films, thermal evaporation, Ion Beam Assisted Deposition, optical communications, SiO_x thin films.

Dedication

A mi padre,
A mi madre,
A mis hermanos.

Acknowledgments

Primero que nada, quiero agradecer a Dios y a la vida misma por permitirme llegar hasta aquí y el poder cumplir mi sueño de graduarme de un posgrado.

Agradezco al Centro de Investigación Científica y de Educación Superior de Ensenada (CICESE) por la maravillosa oportunidad y confianza en mí para realizar mi maestría en sus instalaciones; al Consejo Nacional de Ciencia y Tecnología (CONACYT) por los recursos facilitados a través de la beca 899741 que se me otorgó; proyecto interno F0F170; proyectos de ciencia básica (2017 – 2018) A1-S-21323, A1-S-21084 y A1-S-26789; proyecto FORDECYT - CONACYT 272894; a DGAPA-UNAM a través de los proyectos de investigación PAPIIT IN103220, IG200320, IN110018 y IN113219. Sin estos apoyos, nada de esto habría sido posible.

A mi familia, que sin ellos no sería nada, no sería el que hoy soy. Mil gracias a mis padres Ma. Del Carmen y Juan Manuel, gracias por toda su ayuda, por todo su amor, por su buen ejemplo; gracias por todo lo que han trabajado y los sacrificios que han tenido qué hacer para que no nos faltara nada a mí ni a mis hermanos y siempre velar por nuestro bienestar. A mis hermanos Oralia, Fanny y Néstor, por su apoyo, y por siempre creer en mí; son mi ejemplo de superación y perseverancia. Ustedes, mi familia, han sido, son y serán mi motivación, mis héroes, mi orgullo.

Quiero expresar mi profundo respeto, admiración y agradecimiento a mi director de tesis, el Dr. Heriberto Márquez Becerra, por su enorme paciencia y voluntad de compartir su conocimiento en todo momento desde que lo conocí en 2017 cuando tuve la fortuna de trabajar con él en el verano científico. Gracias por su amistad, sus consejos, regaños, recomendaciones, charlas y sobre todo por su honestidad y transparencia, siempre se agradece convivir con personas así. A thousand of thanks to my thesis co-director, Dr. Karl W. Koch, who I also admire for all his achievements and professionalism. Although I did not have the opportunity to meet him personally, he always had a positive attitude, confidence in me and a great enthusiasm for my learning and for guiding me in the best way during the thesis work.

Agradezco también enormemente a mi comité de tesis, por todo su apoyo, recomendaciones y consejos con la intención de llevar a los mejores términos posibles mi tesis. Muchas gracias, Dra. Carolina Álvarez, Dr. Horacio Soto, Dra. Georgina Navarrete y especialmente al Dr. Javier López por su incesante ayuda, voluntad y colaboración con mi proyecto.

Quiero agradecer a todo el personal tanto de CICESE como de Corning por todo el esfuerzo realizado para que este acuerdo institucional se llevara a cabo: Leslie Vázquez, María Concepción Mendoza, Kevin Sparks

y sobre todo a Luis Zenteno y Costas Saravanos. Gracias también a los miembros de Corning Reynosa por su hospitalidad y ayuda con el proyecto, gracias a Yan Hua, Alma Sánchez, Roberto Soto, Luis Arredondo y Paloma Solano.

Gracias a todos los miembros de CICESE y del Centro de Nanociencias y Nanotecnología CNyN-UNAM que una u otra manera me ayudaron en mi tesis: Dr. Luis Ríos, Ing. Fernando Solorio, Dr. Javier Camacho, Dr. Hugo Tiznado, Miguel Farfán, Jessica Ángel. Y también a todos los investigadores y técnicos que me compartieron sus enseñanzas en clases o laboratorios, todos ustedes han contribuido en mi crecimiento intelectual, profesional y personal. También agradezco al Dr. Nicola Radnev de la UABC Mexicali por su amabilidad y por facilitarnos el acceso a su laboratorio y a su elipsómetro.

Aquí conocí a personas maravillosas a las cuales admiro por su generosidad, intelecto, humanidad y solidaridad. Millones de gracias a Víctor Ruiz por su amistad sincera, por los consejos, sugerencias y por toda la ayuda que me brindó; gracias a mis compañeros de clase Abigail, Danna, Gerson, Arturo, Gisell, Alberto, Eduardo, Jordan y Roberto, por aguantarme en el salón, y sobre todo a Caro y Marino por todas las locuras y por ser parte del extraño pero funcional *trío dinámico*. Muchas gracias a mis compañeros del *Cubo De Los Lamentos:* Miriam, Charlie y Anna, por hacer de ése un lugar especial y ameno para sobrellevar la carga del día a día. A Isaac por siempre apoyarnos en el aula de cómputo y con problemas de nuestras PC's. A Edgardo, Frida, Estefanía y a Claudia por esas largas y agradables charlas. Y todo el resto de compañeros del posgrado en óptica, gracias por su amistad en las buenas y en las malas. También agradezco a mis amigos de otros posgrados, especialmente Ciencias de la Tierra.

A *la familia*: Karina, Nere, Sebastián, Lalo y a Paul por su amistad desde hace más de tres años. Gracias a todos ustedes por todos esos momentos especiales, las risas, su compañía, su ayuda. Gracias por ser como son, por abrirme las puertas de su hogar y por haberme brindado su cariño; siempre estarán en mi corazón, los voy a extrañar mucho cuando ya no los pueda ver en mi día a día.

Y, por último, mas no menos importante, muchas gracias al personal administrativo de CICESE, especialmente a nuestras queridas secretarias del departamento de óptica, que siempre nos reciben con una sonrisa y con ánimos de ayudarnos en todo lo posible; gracias por todo Carmen, Marla y Cruz.

Todos los enlistados aquí (y los que se me pasaron), directa o indirectamente hicieron de esta etapa una de las mejores. Mi vida en Ensenada no habría sido tan bonita como lo fue si no fuera por ustedes y su compañía, ayuda y amistad. Por eso, les repito: muchas gracias.

Table of contents

List of figures

List of tables

Chapter 1. Introduction

Today's society relies on a fast and reliable exchange of information. Advanced communication systems support the operation of industries, businesses and banks, vehicles and transportation systems, household entertainment electronics, and the global flow of news and knowledge (Agrell et al., 2016). For this reason, the previous decades have witnessed an explosive increment in the volume of global network traffic. The amount of annual worldwide data center traffic in 2015 was estimated to be 4.7 Zettabyte and will triple to be 15.3 Zettabyte by 2020. Transporting such an increasing volume of data with existing technologies – such as the conventional metallic interconnects, as the finite resistance and capacitance limit them – will soon reach its limit. Therefore, they will not be able to satisfy the exponentially increasing capacity demands (Zhou et al., 2018). The only known reliable devices that can hold that massive data requirement are optical fibers. Besides, an efficient interconnection scheme with low cost, high energy efficiency, and high bandwidth capacity is in great need. Both optical fibers and their interconnections are the backbone of the optical communications.

Reflection on the surface of an optical device is mainly due to a sharp change in the refractive index at the incident-medium/substrate interface. This surface reflection loss leads to power reduction, and hence, to the signal degradation, ergo the performance of the optical system. To reduce undesired reflection loss in optical devices, their interfaces can be coated by very thin films of material (Figure 1) called *antireflective (AR) coatings* (Liou et al., 2009).

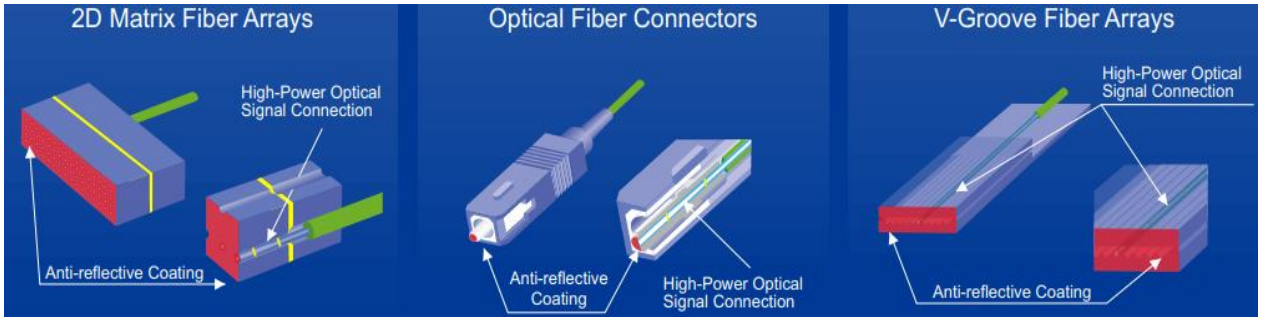

Figure 1 Typical examples of fiber optic components with antireflective coating.

AR coatings are widely used in infrastructure, imaging industry, and optical communications. Besides, they are the fastest-growing type of global optical coatings in the market. It was valued at $2,818 million in 2015 and is expected to garner $4,858 million by 2022 (Doshi, 2017).

The optics market requires three properties in particular of the AR coatings: (1) ultrathin thickness, (2) insensitivity to the angle of incidence of the light, and (3) broadband (Hedayati and Elbahri, 2016). While optical coatings can, in theory, provide perfect antireflection function at a single wavelength, the final performances will then be profoundly affected by the width of the spectral range of interest.

Antireflection coatings can be based on homogeneous or inhomogeneous coatings (Dobrowolski, 1995). Throughout the last century, various methods and strategies have been developed in order to enhance AR coatings performance (Hedayati and Elbahri, 2016). Homogeneous thin films exhibit identical optical constants within their volumes (e.g., single-layer, double-layer, and multilayer). On the other hand, the optical constants of inhomogeneous thin films change within their volumes (e. g., patterned or gradient). The inhomogeneous films of suitable materials often exhibit better optical properties compared with those of multilayer coatings, such as smaller light scattering and insensitivity to the angle of incidence (Ohlídal et al., 2020). However, AR homogeneous layers are still the predominant technology. For this reason, the scope of this thesis is to design, simulate, fabricate, and characterize only homogeneous antireflective coatings.

There are various factors which limit the usage of multilayer (also called broadband) AR coatings, such as the multilayer stack adhesion strength at interfaces, mismatch in thermal properties of different oxide coatings, intricate fabrication process, mechanical stability decrement due to multilayer stacks, and expensive cost (Bashir Khan et al., 2017). Despite the extensive range of developments that have been carried out over the past 30 years, the production of multilayer antireflection coatings for visible and infrared spectra remains a challenge, and the requirements issued from the community are frequently at the limit if not beyond theoretical and manufacturing capabilities (Lemarquis et al., 2019).

Multilayer antireflective coatings are comprised of alternatively high and low refractive index material to create destructive interference of reflected light and generate AR efficiency in the broader wavelength region in the desired wavelength range (Bashir Khan et al., 2017). Thus, the performance of multilayer AR coatings that can be achieved depends on the refractive index of the materials used in the design. The best results are obtained using the lowest and highest possible indices. For this reason, considering oxide materials, the combination of SiO_2 and Nb_2O_5 ($n \approx 1.47$ and 2.35) appears, to date, as the best solution for the visible and near-IR ranges, e.g., 400 – 1100 nm. Besides, low-index substrates such as silica are frequently used in the visible/NIR range and the refractive index of the high-index coating material is then much higher than that of the substrate (Lemarquis et al., 2019).

One way to use a different combination of high and low refractive index of dielectric films is by tuning the refractive index. In recent years, non-stoichiometric silicon oxide films (SiO_x, $1 < x < 2$) have been studied due to their technological importance in numerous applications, including microelectronics, communication, and packaging industries (Carneiro et al., 2019). SiO_x thin-films optical properties are highly dependent on the fabrication process; for example, in a vacuum evaporation process of silicon monoxide (SiO), the optical and physical properties are sensitive to the fabrication conditions: vacuum, deposition rate, substrate temperature, and reactive evaporation. Indeed, the index of refraction of a deposited SiO_x thin film increases as the stoichiometric relation *x* decreases. Among the typical deposition processes that modify the chemical stoichiometry of the SiO_x thin films are physical vapor deposition (PVD), chemical vapor deposition (CVD), and ion implantation (E. G. Lizarraga-Medina et al., 2015). Although SiO_x thin films have also been studied for applications on silicon-based optoelectronic devices like waveguides (Eder G. Lizarraga-Medina et al., 2016), they have not been used in applications on antireflective coatings yet. Therefore, this thesis explores the viability of applying SiO_x thin films on double- and triple-layer AR designs; thermal evaporation technique will be used. Besides, manipulation of the vacuum, deposition rate, and reactive atmosphere to modulate the SiO_x refractive index, taking as guide the SiO_x modulation results reported by Salazar et al. (2016).

The performances of antireflection coatings are also very sensitive to thickness variations of the layers. Consequently, increasing the number of layers of a coating stack to theoretically improve its spectral performances might finally result, when considering manufacturing thickness errors, in poorer performances than a simpler design. Thus, the production of high-performance antireflection coatings requires an accurate thickness control of each layer of the stack. Oxide materials are fully transparent in the visible/NIR spectral range and fully compatible with ion-assisted or sputtering deposition techniques, resulting in excellent mechanical and environmental behavior of the coatings. (Lemarquis et al., 2019). One of the major problems with thin films of dielectric materials fabricated by PVD is the porosity, which usually forms columnar porosities with different diameters. The residual air or water in these porosities can affect optical and other properties. Therefore, a significantly higher temperature is provided to the substrate temperature during the PVD process (Syed et al., 2017).

For this reason, high-quality multilayer AR coatings are nowadays mostly manufactured using energetic processes like Ion Beam Assisted Deposition (IBAD) technique using materials like Nb_2O_5, SiO, SiO_2, Al_2O_3, ZrO_2, TiO_2, and Ta_2O_5. Another scope of this thesis is to manufacture and study the optical properties of four- and five-layer AR designs for the band from 1200 to 1600nm, mainly used for optical communications purposes, made of Nb_2O_5 and SiO_2, using the IBAD technique. This design was fabricated at the Corning

Reynosa facilities due to the current collaboration between Corning Incorporated and the Optics Department of CICESE.

1.1 Hypothesis

The SiO_x ($1 < x < 2$) thin films deposited by reactive thermal evaporation can be used on antireflective coatings. Besides, the greater the number of SiO_x layers deposited on the substrate, the greater the antireflective bandwidth.

1.2 Goal

Analysis of theoretical and experimental fundamentals of AR coatings for optical communications using materials like Nb_2O_5, SiO, SiO_2, Al_2O_3, TiO_2, and MgF_2. In addition, determination of the influence of manufacturing parameters on the optical properties of SiO_x thin films deposited by thermal evaporation. Then, use them on AR coatings designs.

1.2.1 Specific goals

- Theoretical analysis of AR coatings.
- Design and simulate a wide variety of AR coatings, from 1 to 5 layers, using the following materials: Nb_2O_5, SiO, SiO_2, Al_2O_3, TiO_2, and MgF_2.
- Produce SiO_x thin films by the thermal evaporation technique and use them on double- and triple-layer AR designs.
- Manufacture a four-layer BBAR coating by the IBAD technique at Corning Reynosa facilities using Nb_2O_5 and SiO_2.
- Characterize the optical properties of the obtained samples by spectroscopic ellipsometry (SE) and spectrophotometry.

Next is described the information about the chapters of this document to give a perspective of the thesis work. In Chapter 2 are presented the theoretical fundamentals for the study of the optical features of thin films. It begins with the electromagnetic theory; then it goes through concepts like refractive index, optical

admittance, polarization of light, and finishes with something called characteristic matrix, which is an essential concept in the study of thin films.

Chapter 3 presents an explanation of the methods used to fabricate and characterize the deposited films. The experimental stage was divided into two different locations, CICESE and Corning Reynosa. So, it is shown which deposition technique and which characterization equipment was used at each site. Also, an overview of the optical properties of the materials used to manufacture, which are Nb_2O_5, SiO_2, and SiO_x.

Chapter 4 presents several results that were important in the achievement of this thesis, such as theoretical AR designs (layers' thicknesses, refractive indices, etc.), simulation, fabrication for each location previously mentioned, and the results of the optical characterization. Besides, a discussion of these results is presented as well.

The last chapter is the 5^{th} one, where general conclusions of this work are exposed, and a comparison between deposition techniques used for the experiments. In addition, some future work is also shown.

Chapter 2. Theoretical Basis

Antireflective coatings (AR) are widely applied to eliminate the unwanted surface reflections from the AR coated substrate. Nowadays, AR coatings have potential applications in photovoltaic solar cells, sensors, display-devices, automobile industries, and they have been employed as an integral segment to increase the output efficiency of different electro-optical devices (Bashir Khan et al., 2017). This chapter shows the theory of AR coatings, departing from the fundamentals based on Maxwell equations and some basic concepts related to, such as refractive index, optical admittance, irradiance, reflection, reflectance, and characteristic matrix.

2.1 Electromagnetic waves and Maxwell's equations

Michael Faraday, an English chemist and physicist, was the first to use magnetic fields to produce an electric current, which led him to theorize that magnetism and electricity are aspects of one force. He also speculated that light may be yet another aspect of this force. James Clerk Maxwell, a Scottish mathematician and physicist, followed up on Faraday's speculations and provided a unified theory of electromagnetism in 1865, which predicted the existence of a new phenomenon: electromagnetic waves. Maxwell predicted that these new waves would travel at approximately the same speed as the speed of light. Not believing this to be a coincidence, he predicted that experiments would show light to be a form of electromagnetic wave (Figure 2). In 1862 Maxwell wrote:

"We can scarcely avoid the conclusion that light consists in the transverse ondulations of the same medium, which is the cause of electric and magnetic phenomena."

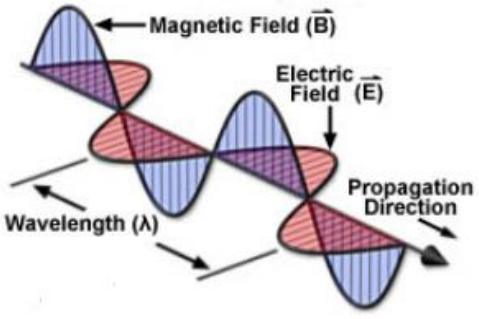

Figure 2 Electromagnetic wave

Maxwell began to see the connections between the approaches of Faraday, Riemann, and Gauss. As a result, he was able to derive one of the most elegant theories yet formulated. Using four equations, he described and quantified the relationships between electricity, magnetism, and the propagation of electromagnetic waves. The equations are now known as **Maxwell's Equations**. These equations describe the behavior of a wave in the vacuum or in a media. In this thesis, the media is dielectric (absence of space charge, ρ=0), isotropic, and homogenous. Considering these properties, Maxwell's equations (Table 1) are:

Table 1 Maxwell's equations for a dielectric, isotropic and homogenous media

Name	Equation
Ampère's Law	$\vec{\nabla} \times \vec{H} = \vec{j} + \frac{\partial \vec{D}}{\partial \vec{t}}$
Faraday's Law	$\vec{\nabla} \times \vec{E} = -\frac{\partial \vec{B}}{\partial \vec{t}}$
Gauss' Law	$\vec{\nabla} \cdot \vec{D} = \rho = 0$
Gauss' Law for magnetic fields	$\vec{\nabla} \cdot \vec{B} = 0$

Where:

$$\vec{j} = \sigma \vec{E} \quad (1)$$

$$\vec{D} = \varepsilon \vec{E} \quad (2)$$

$$\vec{B} = \mu \vec{H} \quad (3)$$

Table 2 shows the definitions of the quantities used in previous equations using the International System of Units (SI). All the equations presented in this manuscript are based on the meter, kilogram, and second (MKS) system of units.

Table 2 SI units and symbols

Symbol	Physical Quantity	SI Unit	Symbol for SI Unit
E	Electric field strength	Volt per meter	V/m
D	Electric displacement	Coulomb per square meter	C/m^2
H	Magnetic field strength	Ampere per meter	A/m
j	Electric current density	Ampere per square meter	A/m^2
B	Magnetic flux density or magnetic induction	Tesla	T
ρ	Electric charge density	Coulomb per cubic meter	C/m^3
σ	Electric conductivity	Siemens per meter	S/m
μ	Magnetic permeability	Newton per square ampere	N/A^2
ε	Electric permittivity	Farad per meter	F/m

To the equations, we can add

$$\varepsilon = \varepsilon_r \varepsilon_0 \tag{4}$$

$$\mu = \mu_r \mu_0 \tag{5}$$

$$\varepsilon_0 = \frac{1}{\mu_0 c^2} \tag{6}$$

Where ε_0 and μ_0 are the electric permittivity and magnetic permeability of free space, respectively; ε_r and μ_r are the relative permittivity and permeability, respectively, and c is the velocity of light in the free space. The values of these constants are important; those are:

$$c = 299\,792\,458 \text{ m/s}$$
$$\varepsilon_0 = 8.854\,187\,8182 \text{ x}10^{-12} \text{ F/m}$$
$$\mu_0 = 1.256\,637\,062\,12 \text{ x}10^{-6} \text{ N}/A^2$$

2.2 The complex refractive index

Recalling from Gauss' Law and Equation 2, we have

$$\vec{\nabla} \cdot \vec{D} = \varepsilon\left(\vec{\nabla} \cdot \vec{E}\right) = 0 \quad \Rightarrow \quad \vec{\nabla} \cdot \vec{E} = 0 \tag{7}$$

Applying the curl operator ($\vec{\nabla} \times$) and using the vector property $\vec{\nabla} \times \vec{\nabla} \times \vec{E} = \vec{\nabla}\left(\vec{\nabla} \cdot \vec{E}\right) - \vec{\nabla}^2\vec{E}$ we can get

$$\vec{\nabla}\left(\vec{\nabla} \cdot \vec{E}\right) - \vec{\nabla}^2\vec{E} = -\mu\frac{\partial}{\partial \vec{t}}\left(\vec{\nabla} \times \vec{H}\right) \tag{8}$$

We substitute the Ampère's Law and the Equation 7 on Equation 8; we arrive to

$$\vec{\nabla}^2\vec{E} = \mu\varepsilon\frac{\partial^2\vec{E}}{\partial \vec{t}^2} + \mu\sigma\frac{\partial \vec{E}}{\partial \vec{t}} \tag{9}$$

We look for a solution to Equation 9; we propose it in the form of a linearly polarized harmonic wave represented in the complex form,

$$\vec{E} = E_0 e^{-i\omega\left(t-\frac{z}{v}+\varphi\right)} = E_0 e^{-i\varphi} e^{-i\omega\left(t-\frac{z}{v}\right)} \tag{10}$$

Which represents a wave propagating along the z-axis with velocity v. E_0 is the vector amplitude, ω is the angular frequency, φ the relative phase, and the expression $E_0 e^{-i\varphi}$ is the complex vector amplitude. Note that we are dealing with linear phenomena, ω is invariant as the wave propagates through media with different properties.

Assuming $\varphi = 0$ and substituting Equation 10 in Equation 9 and working it out, will be arriving at the point where it is necessary that

$$\frac{\omega^2}{v^2} = \omega^2\varepsilon\mu - i\omega\mu\sigma \tag{11}$$

In vacuum, we have $\sigma = 0$ and $v = c$, so that from Equation 11,

$$c^2 = \frac{1}{\mu_0\varepsilon_0} \tag{12}$$

which is identical to Equation 6. Multiplying Equation 12 by Equation 11 and dividing through by ω^2, we obtain

$$\frac{c^2}{v^2} = \frac{\varepsilon\mu}{\varepsilon_0\mu_0} - i\frac{\mu\sigma}{\omega\varepsilon_0\mu_0} \tag{13}$$

Where c/v is a dimensionless parameter of the medium, which can be denoted by N:

$$N^2 = \varepsilon_r\mu_r - i\frac{\mu_r\sigma}{\omega\varepsilon_0} \tag{14.1}$$

That implies that N is of the form

$$N = \frac{c}{v} = n - ik \tag{14.2}$$

N is known as the *complex refractive index*, n is the real part of the refractive index (or often merely as refractive index, because N is real in a dielectric material), and k is known as the extinction coefficient.

Knowing that $N = \frac{c}{v} = n - ik \quad \Rightarrow \quad v = \frac{c}{N}$; therefore, Equation 10 can be written

$$\vec{E} = E_0 e^{-i\omega\left(t-\frac{Nz}{c}\right)} = E_0 e^{-i\omega\left(t-\frac{nz-ikz}{c}\right)} = E_0 e^{-\frac{\omega kz}{c}} e^{-i\omega\left(t-\frac{nz}{c}\right)} \tag{15}$$

Then, from the dispersion equation of a wave in a medium

$$c = \frac{\omega}{k} = \frac{\omega}{\frac{2\pi}{\lambda}} \quad \Rightarrow \quad \frac{2\pi}{\lambda} = \frac{\omega}{c} \tag{16}$$

Where λ is the wavelength in free space. Thus, Equation 15 can be written as

$$\vec{E} = E_0 e^{-\frac{2\pi}{\lambda}kz} e^{i\left(\omega t-\frac{2\pi}{\lambda}nz\right)} \tag{17}$$

Moreover, the significance of k emerges as being a measure of absorption in the medium (Figure 3). The distance $\lambda/2\pi k$ is that in which the amplitude of the wave falls to $1/e$ of its original value (also known as skin depth). The change in phase produced by a traversal of distance z in the medium is the same as that produced by a distance nz in the vacuum. Because of this, nz is known as the optical distance, as distinct of physical distance.

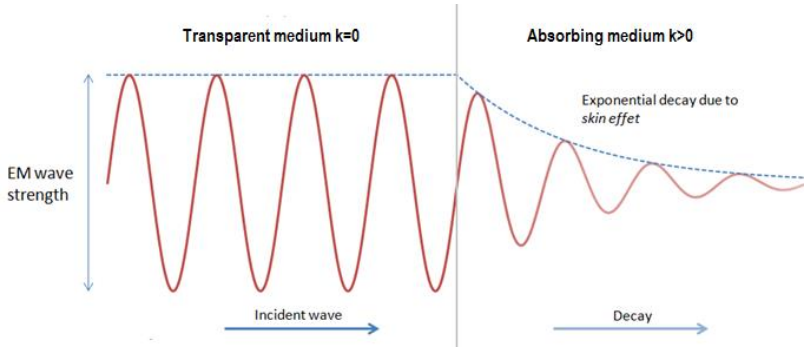

Figure 3 Propagation of an electromagnetic wave through a transparent medium (left) and absorbing medium (right).

2.3 Optical Admittance

From Equation 15, we know that $\vec{E} = E_0 e^{-i\omega\left(t-\frac{Nz}{c}\right)}$. Substituting it in Ampère's Law, we obtain

$$\vec{\nabla} \times \vec{H} = (\sigma + i\omega\varepsilon)\vec{E} \tag{18}$$

Besides, from Equations 13 and 6,

$$\vec{\nabla} \times \vec{H} = (\sigma + i\omega\varepsilon)\vec{E} = \frac{i\omega}{c^2\mu} N^2 \vec{E} \tag{19}$$

On the other hand, assuming that the magnetic field has a similar expression that Equation 15, and it is propagating as well through the z-axis; such as $\vec{H} = H_0 e^{-i\omega\left(t-\frac{Nz}{c}\right)}$, applying the curl using the vector product we obtain

$$\vec{\nabla} \times \vec{H} = -i\frac{\omega N}{c}\hat{\jmath} = -i\frac{\omega N}{c}\left(\hat{s} \times \vec{H}\right) \tag{20}$$

Where the unit vector $\hat{s}$ gives the direction of propagation of the wave, and $\hat{\jmath}$ is the unit vector along the y-axis.

Notice that Equations 20 and 19 are equal. So,

$$-i\frac{\omega N}{c}\left(\hat{s} \times \vec{H}\right) = \frac{i\omega}{c^2\mu} N^2 \vec{E} \tag{21}$$

This is

$$\left(\hat{s} \times \vec{H}\right) = -\frac{N}{c\mu}\vec{E} \tag{22}$$

For this type of wave, therefore, $\vec{H}, \vec{E}$ and $\hat{s}$ are mutually perpendicular like any other electromagnetic wave propagating through a dielectric and isotropic media. The quantity $N/c\mu$ has the dimensions of admittance and is known as the characteristic optical admittance of the medium, written y. So,

$$y = \frac{N}{c\mu} \tag{23}$$

In free space, the optical admittance is

$$\mathcal{Y}_0 = \sqrt{\frac{\varepsilon_0}{\mu_0}} = 2.6544 \times 10^{-3}\, S \tag{24}$$

Now, we can also write

$$y = \mathcal{Y}_0 N \tag{25}$$

Thus,

$$\vec{H} = y\left(\hat{s} \times \vec{E}\right) = \mathcal{Y}_0 N\left(\hat{s} \times \vec{E}\right) \tag{26}$$

2.4 The Poynting Vector

An essential feature of electromagnetic radiation is that it is a form of energy transport, and it is the energy associated with the wave, which is typically observed. The instantaneous rate of flow of energy across unit area is given by the Poynting vector

$$\vec{S} = \vec{E} \times \vec{H} \tag{27}$$

The direction of the vector is in the same direction of the energy flow.

Multiplication of two complex numbers mixes the real and imaginary parts in the result. Such operations are known as nonlinear, as is the case of the Poynting vector. So, we have a problem with the complex form of the wave. Either the real or the imaginary part of the wave expression should be used. The real sine or cosine form of the wave implies its square in the result, and so the instantaneous value of the

Poynting vector must oscillate at twice the frequency of the wave. We turn our attention to the mean value because it is a significant one in our measurements. This is defined as the irradiance, denoted by I. In the SI system of units, irradiance is measured in watts per meter squared. The mean (or irradiance) of the Poynting vector is

$$\vec{I} = \frac{1}{2} Re\left(\vec{E} \times \vec{H}^*\right) \tag{28}$$

Where * denotes the complex conjugate. Furthermore, this equation is valid when the irradiance has the same direction as the flow of energy. The more usual scalar irradiance I is simply the magnitude of $\vec{I}$. Because $\vec{E}$ and $\vec{H}$ are perpendicular, Equation 28 can be written

$$I = \frac{1}{2} Re(EH^*) \tag{29}$$

Where E and H are scalar magnitudes.

For a single, homogeneous, harmonic wave of the form of Equation 15:

$$\vec{H} = y\left(\hat{s} \times \vec{E}\right) \tag{30}$$

So,

$$\vec{I} = Re\left(\frac{1}{2} y\vec{E}\vec{E}^*\hat{s}\right) = \frac{1}{2} n y_0 \vec{E}\vec{E}^*\hat{s} = \frac{1}{2} n y_0 \left|\vec{E}\right|^2 \tag{31}$$

And in terms of scalar magnitudes,

$$I = \frac{1}{2} n y_0 |E_0|^2 e^{-\frac{4\pi k}{\lambda} z} \tag{32}$$

The distance represented by $\lambda/4\pi k$ represents where does the irradiance drop to $1/e$ of its initial value. The inverse of this distance is defined as the absorption coefficient α; that is

$$\alpha = \frac{4\pi k}{\lambda} \tag{33}$$

If there is no absorption in the media, $k = \alpha = 0$.

2.5 Waves at an interface

2.5.1 Single boundary: reflection coefficient and Snell's Law

Thin-film filters usually consist of several boundaries between various homogenous media, and it is the effect of these boundaries on an incident wave that we will wish to calculate. A single boundary is the simplest case. First, we consider absorption-free media, i.e., $k = 0$.

The arrangement is sketched in Figure 4(a). A plane harmonic wave is an incident on a plane surface separating the incident medium from the second or emergent medium, each one with different refractive index. The plane containing the normal to the surface and the direction of propagation of the incident wave is known as the plane of incidence, Figure 4(b). We take the z-axis as the normal into the surface in the sense of the incident wave, and the x-axis as the normal to it and also in the plane of incidence. At a boundary, the tangential components of $\vec{E}$ and $\vec{H}$ –that is, the components along with the interface– are continuous across it because no mechanism will change them. This condition at the interface is fundamental in the thin-film theory.

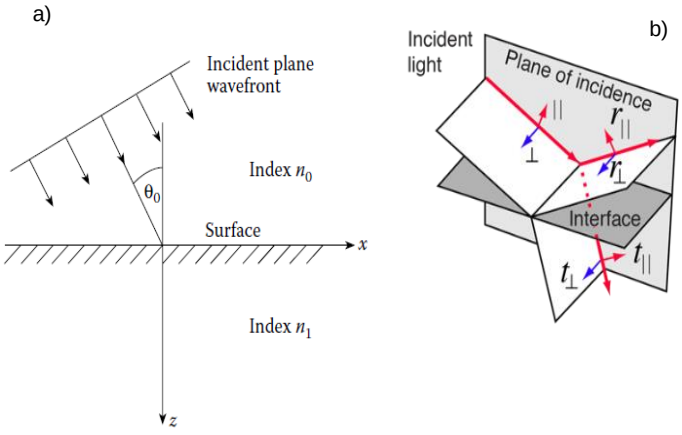

Figure 4 (a) Plane-wave incident on a single surface. (b) Sketch of the plane of incidence, surface, and incident light.

Our objective then becomes calculating the relative parameters of three waves: incident, reflected, and transmitted. We can help ourselves by defining the boundary by $z = 0$. Then, the tangential components must be continuous for all values of x, y, and t.

Let the direction cosines of the $\hat{s}$ vector of the transmitted and reflected waves be given by $(\alpha_t, \beta_t, \gamma_t)$ and $(\alpha_r, \beta_r, \gamma_r)$, respectively. For waves to satisfy the boundary conditions for all x, y, t at $z = 0$, implies that

the coefficients of these variables must be separately identically equal. Had we not already known that there would be no change in frequency, this would have confirmed it. Because the frequencies are constants, so, too, will be the free space wavelengths. Next

$$0 \equiv n_0\beta_r \equiv n_1\beta_t \tag{34}$$

This is, the directions of the reflected and transmitted or refracted beams are confined to the plane of incidence. This, in turn, means that the direction cosines of the reflected and transmitted (Figure 5) waves are

Reflected wave $\alpha_r = \sin\theta_r \qquad \gamma_r = \cos\theta_r$ (35.1)

Transmitted wave $\alpha_t = \sin\theta_t \qquad \gamma_t = \cos\theta_t$ (35.2)

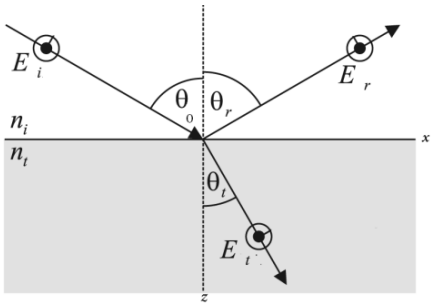

Figure 5 Angles of the incident, reflected and transmitted waves.

Also,

$$n_0 \sin\theta_0 \equiv n_0\alpha_r \equiv n_1\alpha_t \quad \Rightarrow \quad n_0 \sin\theta_0 \equiv n_0 \sin\theta_r \equiv n_1 \sin\theta_t \tag{36}$$

So that if the angles of reflection and refraction are θ_r and θ_t, respectively, then

$$\theta_0 = \theta_r \tag{37}$$

That is, the angle of reflection equals the angle of incidence. This is known as *Reflection Law*. Besides,

$$n_0 \sin\theta_0 = n_1 \sin\theta_t \tag{38}$$

This is the familiar relationship known as *Snell's Law*.

2.5.2 Normal incidence

Let the incident wave be a linearly polarized plane harmonic wave. The xy plane is the plane of the boundary (surface). We can take the incident wave as propagating along the z-axis with the positive direction of the $\vec{E}$ vector along the x-axis. Then, the positive direction of the $\vec{H}$ vector will be the y-axis. It is clear that the only waves that satisfy the boundary conditions are linearly polarized in the same plane as the incident wave (Figure 6a).

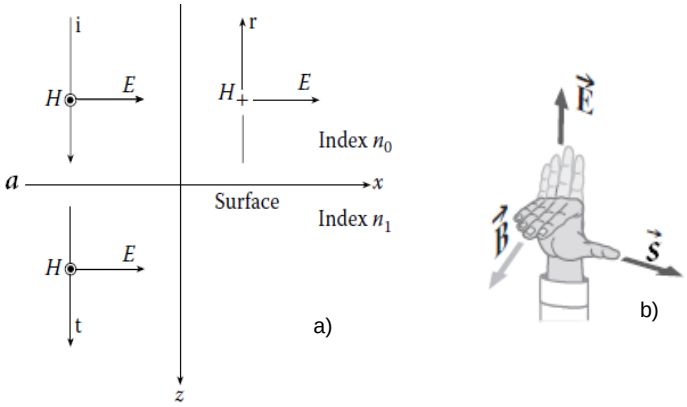

Figure 6 (a) Convention defining positive directions of the electric and magnetic vectors for reflection and transmission at an interface at normal incidence. (b) Right-hand set.

Then is a little problem: the waves have electric and magnetic fields that with the direction propagation (vector $\hat{s}$) form a right-handed set (Figure 6(b)). Because the direction of propagation is reversed in the reflected beam, the orientation of $\vec{E}$ and $\vec{H}$ cannot remain the same as that in the incident beam; otherwise, we would no longer have a right-handed set. Because the electric field is the one that is more important from the point of view of interaction with matter, we will define our directions with respect to it. This is, making a directions reference called a convention because we have complete freedom of choice, and any self-consistent arrangement is possible. We must simply ensure that once we made our choice, we adhere to it. So, we define the positive direction of $\vec{E}$ along the x-axis for all the beams that are involved. Because of this choice, the positive direction of $\vec{H}$ will be along the y-axis for the incident and transmitted wave but along the negative direction of the y-axis for the reflected wave, just as it is shown in Figure 6(a).

We now consider the boundary conditions. Because of the Law of Conservation of Energy, the amplitudes of the fields at the surface a will be:

- Electric vector continuous across the boundary a.

$$E_i + E_r = E_t \tag{39.1}$$

- Magnetic vector continuous across the boundary a

$$H_i - H_r = H_t \tag{39.2}$$

Where we must use a minus sign because of our convention for positive directions. From Equation 26, we know the relationship between magnetic and electric field through the characteristic admittance; this gives

$$y_0E_i - y_0E_r = y_1(E_i + E_r) \quad \Rightarrow \quad E_i(y_0 - y_1) = E_r(y_0 + y_1) \quad \Rightarrow \quad \frac{E_r}{E_i} = \frac{y_0 - y_1}{y_0 + y_1} \tag{40}$$

Remembering that $y = \mathcal{Y}_0 N$

$$\frac{E_r}{E_i} = \frac{y_0 - y_1}{y_0 + y_1} = \frac{\mathcal{Y}_0 N_0 - \mathcal{Y}_0 N_1}{\mathcal{Y}_0 N_0 + \mathcal{Y}_0 N_1} = \frac{N_0 - N_1}{N_0 + N_1} \tag{41}$$

Similarly, if we now solve for E_r at Equation 39.1, substituting it in Equation 40, and so on, we obtain

$$\frac{E_t}{E_i} = \frac{2y_0}{y_0 + y_1} = \frac{2\mathcal{Y}_0 N_0}{\mathcal{Y}_0 N_0 + \mathcal{Y}_0 N_1} = \frac{2N_0}{N_0 + N_1} \tag{42}$$

The quantities from Equations 41 and 42 are called *amplitude reflection* and *transmission coefficients* and are denoted by ρ and τ, respectively. Thus,

$$\rho = \frac{y_0 - y_1}{y_0 + y_1} = \frac{N_0 - N_1}{N_0 + N_1} \tag{43}$$

$$\tau = \frac{2y_0}{y_0 + y_1} = \frac{2N_0}{N_0 + N_1} \tag{44}$$

Where $N = n - ik$ is the complex refractive index.

We now examine the energy balance at the boundary. The total tangential components of the electric and magnetic fields are continuous across it, but also because the boundary is of zero thickness, it can neither supply energy nor extract energy from the waves. So that we can write from Equations 29 and 39.1,

$$net\ irradiance = I = \frac{1}{2}Re(EH^*) = Re\left[\frac{1}{2}E_t(y_1E_t)^*\right] = Re\left[\frac{1}{2}(E_i + E_r)(y_0E_i - y_0E_r)^*\right] \tag{45}$$

Given the physical definitions of ρ and τ, $E_r = \rho E_i$ and $E_t = \tau E_i$

$$net\ irradiance = \frac{1}{2} y_0 E_i E_i^* (1 - \rho^2) = \frac{1}{2} y_0 E_i E_i^* \frac{y_1}{y_0} \tau^2 \tag{46}$$

From the above equation, we recognize:

Irradiance of incident beam $$I_i = \frac{1}{2} y_0 E_i E_i^* \tag{47.1}$$

Irradiance of reflected beam $$I_r = \rho^2 \frac{1}{2} y_0 E_i E_i^* = \rho^2 I_i \tag{47.2}$$

Irradiance of transmitted beam $$I_t = \frac{1}{2} y_0 E_i E_i^* \frac{y_1}{y_0} \tau^2 = \frac{y_1}{y_0} \tau^2 I_i \tag{47.3}$$

We define the *reflectance* R as the ratio of the reflected and incident irradiances, and the *transmittance* T as the ratio of the transmitted and incident irradiances. Then,

$$T = \frac{I_t}{I_i} = \frac{y_1}{y_0} \tau^2 = \frac{4 y_0 y_1}{(y_0 + y_1)^2} = \frac{4 n_0 n_1}{(n_0 + n_1)^2} \tag{48.1}$$

$$R = \frac{I_r}{I_i} = \rho^2 = \left(\frac{y_0 - y_1}{y_0 + y_1} \right)^2 = \left(\frac{n_0 - n_1}{n_0 + n_1} \right)^2 \tag{48.2}$$

From the previous equations, we have to ensure that

$$(1 - R) = T \tag{49}$$

Remember that all of this assumes that there is no absorption. When absorption is present, the situation changes slightly.

2.5.3 Oblique incidence: s and p polarized light

There are two orientations of the incident wave that lead to reasonably straightforward calculations: the vector electrical amplitudes aligned parallel to the plane of incidence (i. e., the xz plane in Figure 4), this wave is known as p-polarized or TM (transversal magnetic). And the wave with the electrical vector normal to the plane of incidence (i. e., y-axis in Figure 4) as s-polarized or TE (transverse electric). p and s are derived from the German parallel and senkrecht (perpendicular).

Before we can proceed to the calculation of reflected and transmitted amplitudes, we have, once again, establish the convention of reference direction of the vectors, just as in the normal incidence case. The

conventions used here are shown in Figures 7 and 8. We can now apply the boundary conditions considering the vector amplitudes.

2.5.3.1 s-polarized light

Because of the Law of Conservation of Energy:

a) Electric component parallel to the boundary, continuous across it.

$$E_i + E_r = E_t \tag{50}$$

b) Magnetic component parallel to the boundary, continuous across it.

$$-H_i \cos\theta_i + H_r \cos\theta_r = -H_t \cos\theta_t \tag{51}$$

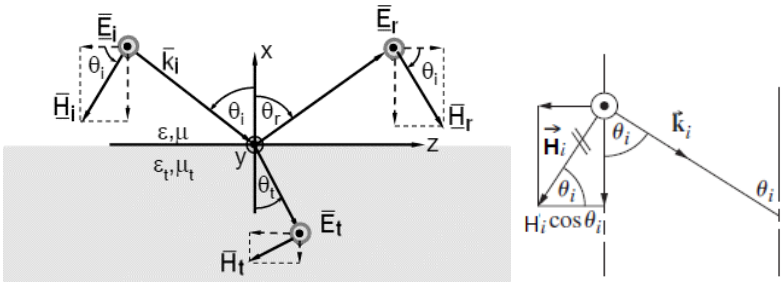

Figure 7 Convention defining positive directions of the electric and magnetic vectors for s-polarized light (TE waves).

Recalling to Equation $H = yE$ to operate on Equation 51, and given that $\theta_i = \theta_r$

$$-y_0 E_i \cos\theta_i + y_0 E_r \cos\theta_r = -y_1 E_t \cos\theta_t \quad \Rightarrow \quad y_0 \cos\theta_i (E_i - E_r) = y_1 E_t \cos\theta_t \tag{52}$$

Operating Equation 50 on Equation 52

$$\frac{E_r}{E_i} = \frac{y_0 \cos\theta_i - y_1 \cos\theta_t}{y_1 \cos\theta_t + y_0 \cos\theta_i} \tag{53}$$

Similarly, if we now solve for E_r at Equation 50, we obtain

$$\frac{E_t}{E_i} = \frac{2y_0 \cos\theta_i}{y_1 \cos\theta_t + y_0 \cos\theta_i} \tag{54}$$

Given the definitions of ρ and τ,

$$\rho_s = \frac{E_r}{E_i} = \frac{y_0 \cos\theta_i - y_1 \cos\theta_t}{y_1 \cos\theta_t + y_0 \cos\theta_i} = \frac{N_0 \cos\theta_i - N_1 \cos\theta_t}{N_0 \cos\theta_i + N_1 \cos\theta_t} \tag{55.1}$$

$$\tau_s = \frac{E_t}{E_i} = \frac{2y_0 \cos\theta_i}{y_1 \cos\theta_t + y_0 \cos\theta_i} = \frac{2N_0 \cos\theta_i}{N_0 \cos\theta_i + N_1 \cos\theta_t} \tag{55.2}$$

For *reflectance* R and *transmittance* T, the expressions remain equal than normal incidence, except that, for transmittance T, has to be considered the transversal area of incident and transmitted waves ($\cos\theta_t / \cos\theta_i$). Thus,

$$R_s = {\rho_s}^2 = \left(\frac{N_0 \cos\theta_i - N_1 \cos\theta_t}{N_0 \cos\theta_i + N_1 \cos\theta_t}\right)^2 \tag{56.1}$$

$$T_s = \frac{\cos\theta_t}{\cos\theta_i}\frac{N_1}{N_0}{\tau_s}^2 = \frac{4N_0N_1 \cos\theta_i \cos\theta_t}{(N_0 \cos\theta_i + N_1 \cos\theta_t)^2} \tag{56.2}$$

Where $y = NY_0$, $N = n - ik$, and the rule $R + T = 1$ is retained. The suffix s has been used in the above expressions to denote s-polarization.

2.5.3.2 p-polarized light

A similar pair of equations can be derived when the incoming $\vec{E}$-field lies in the plane of incidence. Continuity of the tangential components of $\vec{E}$ on either side of the boundary leads to:

a) Electric component parallel to the boundary, continuous across it.

$$E_i \cos\theta_i - E_r \cos\theta_r = E_t \cos\theta_t \tag{57}$$

b) Magnetic component parallel to the boundary, continuous across it.

$$H_i + H_r = H_t \tag{58}$$

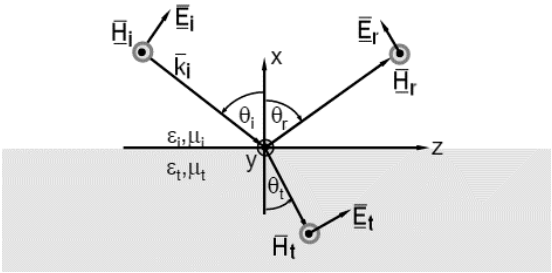

Figure 8 Convention defining positive directions of the electric and magnetic vectors for p-polarized light (TM waves).

By a process similar to that we already used before, we obtain

$$\rho_p = \frac{E_r}{E_i} = \frac{y_1 \cos\theta_i - y_0 \cos\theta_t}{y_0 \cos\theta_t + y_1 \cos\theta_i} = \frac{N_1 \cos\theta_i - N_0 \cos\theta_t}{N_0 \cos\theta_t + N_1 \cos\theta_i} \tag{59.1}$$

$$\tau_p = \frac{E_t}{E_i} = \frac{2y_0 \cos\theta_i}{y_0 \cos\theta_t + y_1 \cos\theta_i} = \frac{2N_0 \cos\theta_i}{N_0 \cos\theta_t + N_1 \cos\theta_i} \tag{59.2}$$

$$R_p = {\rho_p}^2 = \left(\frac{N_1 \cos\theta_i - N_0 \cos\theta_t}{N_0 \cos\theta_t + N_1 \cos\theta_i}\right)^2 \tag{59.3}$$

$$T_p = \frac{\cos\theta_t}{\cos\theta_i}\frac{N_1}{N_0}{\tau_p}^2 = \frac{4N_0N_1 \cos\theta_i \cos\theta_t}{(N_0 \cos\theta_t + N_1 \cos\theta_i)^2} \tag{59.4}$$

Where again, $y = N\mathcal{Y}_0$, $N = n - ik$, and the rule $R + T = 1$ is retained. The suffix p has been used in the above expressions to denote p-polarization.

2.6 Admittance of a thin film

An extension of the above analysis occurs in the case of a thin, plane parallel film of material covering a substrate's surface. The presence of two or more interfaces means that successive reflections will produce several beams, and the summation of these beams will determine the properties of the film. We say that the film is thin when full interference effects can be detected in the reflected or transmitted light.

The arrangement is illustrated in Figure 9. It is convenient to introduce a new notation. We denote waves in the direction of incidence by the symbol + (i.e., positive-going) and the waves in the opposite direction by – (i.e., negative-going). The interfaces between the film and the incident medium, and the substrate,

denoted by a and b, can be treated in the same way as the simple boundary already discussed; we consider the tangential components of the fields.

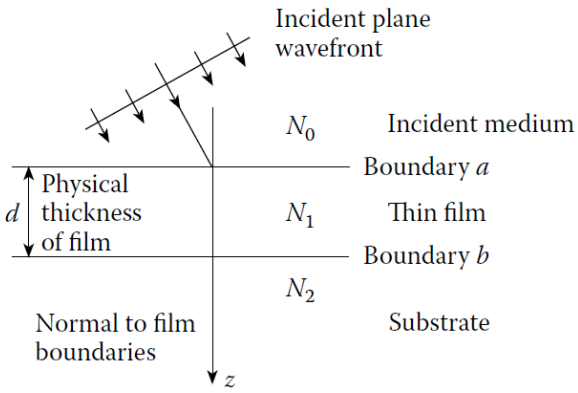

Figure 9 Plane-wave incident on a thin film.

We begin analyzing the boundary b. At this interface, there is no negative-going wave coming from the other (and unseen) face of the substrate. The waves at this place can be summed into one resultant positive-going wave (coming from boundary a), and one resulting negative-going wave (reflection at interface b). Then, the tangential component of $\vec{E}$ and $\vec{H}$ are:

$$E_b = E_{1b}^{+} + E_{1b}^{-} \tag{60.1}$$

$$H_b = H_{1b}^{+} - H_{1b}^{-} = y_1 E_{1b}^{+} - y_1 E_{1b}^{-} \tag{60.2}$$

Solving for E_{1b}^{-} from Equation 60.1 and operating it on Equation 60.2

$$H_b = y_1 E_{1b}^{+} - y_1 (E_b - E_{1b}^{-}) \quad \Rightarrow \quad E_{1b}^{+} = \frac{1}{2}\left(\frac{H_b}{y_1} + E_b\right) \tag{61.1}$$

Then, solving for E_{1b}^{+} and doing a similar process,

$$E_{1b}^{-} = \frac{1}{2}\left(-\frac{H_b}{y_1} + E_b\right) \tag{61.2}$$

And the magnetic field

$$H_{1b}^{+} = y_1 E_{1b}^{+} = \frac{1}{2}(H_b + y_1 E_b) \tag{62.1}$$

$$H_{1b}^{-} = -y_1 E_{1b}^{-} = \frac{1}{2}(H_b - y_1 E_b) \tag{62.2}$$

The fields at the interface a at the same instant, and at a point with identical x and y coordinates can be determined by altering the phase factors of the waves to allow for a shift in the z coordinate from 0 to -d. The positive-going wave will be multiplied by the phase factor $e^{i\delta}$, where

$$\delta = \frac{2\pi N_1 d \cos\theta_t}{\lambda} \tag{63}$$

Where $N_1 = n_1 - k_1$; while the negative-going wave will be multiplied by the phase factor $e^{-i\delta}$. Then, the values of E and H at the interface a are

$$E_{1a}^{+} = E_{1b}^{+} e^{i\delta} = \frac{1}{2}\left(\frac{H_b}{y_1} + E_b\right) e^{i\delta} \tag{64.1}$$

$$E_{1a}^{-} = E_{1b}^{-} e^{-i\delta} = \frac{1}{2}\left(-\frac{H_b}{y_1} + E_b\right) e^{-i\delta} \tag{64.2}$$

$$H_{1a}^{+} = H_{1b}^{+} e^{i\delta} = \frac{1}{2}(H_b + y_1 E_b) e^{i\delta} \tag{64.3}$$

$$H_{1a}^{-} = H_{1b}^{-} e^{-i\delta} = \frac{1}{2}(H_b - y_1 E_b) e^{-i\delta} \tag{64.4}$$

So,

$$E_a = E_{1a}^{+} + E_{1a}^{-} = E_b\left(\frac{e^{i\delta} + e^{-i\delta}}{2}\right) + H_b\left(\frac{e^{i\delta} - e^{-i\delta}}{2y_1}\right)$$

$$= E_b \cos\delta + iH_b \frac{\sin\delta}{y_1} \tag{65.1}$$

Similarly,

$$H_a = H_{1a}^{+} + H_{1a}^{-} = y_1 E_b\left(\frac{e^{i\delta} - e^{-i\delta}}{2}\right) + H_b\left(\frac{e^{i\delta} + e^{-i\delta}}{2}\right)$$

$$= iy_1 E_b \sin\delta + H_b \cos\delta \tag{65.2}$$

These two simultaneous equations can be written in matrix notation as

$$\begin{bmatrix} E_a \\ H_a \end{bmatrix} = \begin{bmatrix} \cos\delta & i\frac{\sin\delta}{y_1} \\ i\,y_1\sin\delta & \cos\delta \end{bmatrix} \begin{bmatrix} E_b \\ H_b \end{bmatrix} \tag{66}$$

We define the optical admittance of the assembly by analogy with Equation 26

$$Y = \frac{H_a}{E_a} \tag{67}$$

So that

$$\begin{bmatrix} B \\ C \end{bmatrix} = \begin{bmatrix} \cos\delta & i\frac{\sin\delta}{y_1} \\ i\,y_1\sin\delta & \cos\delta \end{bmatrix} \begin{bmatrix} 1 \\ y_2 \end{bmatrix} \tag{68}$$

Where B and C, the normalized electric and magnetic fields at the front interface are the quantities from which we will be extracting the thin-film system's properties, and this 2x1 matrix is called the characteristic matrix of the assembly. In contrast, the 2x2 matrix on the right-hand side is known as the thin film's characteristic matrix. So, we can write

$$Y = \frac{C}{B} = \frac{H_a}{E_a} \tag{69}$$

2.7 Admittance of an assembly of thin films

Let another film be added to the single film of the previous section. So, the final interface is now denoted by c, as shown in Figure 10. The characteristic matrix of the film nearest the substrate is

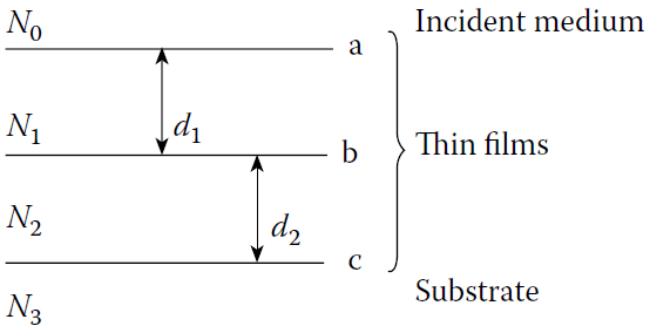

Figure 10 Notation for two thin films on a surface.

$$\begin{bmatrix} \cos\delta_2 & i\dfrac{\sin\delta_2}{y_2} \\ i\,y_2\sin\delta_2 & \cos\delta_2 \end{bmatrix}$$

And the characteristic matrix of the assembly, by analogy with Equation 68

$$\begin{bmatrix} B \\ C \end{bmatrix} = \begin{bmatrix} \cos\delta_1 & i\frac{\sin\delta_1}{y_1} \\ i\,y_1\sin\delta_1 & \cos\delta_1 \end{bmatrix} \begin{bmatrix} \cos\delta_2 & i\frac{\sin\delta_2}{y_2} \\ i\,y_2\sin\delta_2 & \cos\delta_2 \end{bmatrix} \begin{bmatrix} 1 \\ y_3 \end{bmatrix} \tag{70}$$

Y is, as before, $\frac{C}{B}$.

This result can be immediately extended to the general case of an assembly of q layers, when the characteristic matrix is simply the product of the individual matrices taken in the correct order, i.e.,

$$\begin{bmatrix} B \\ C \end{bmatrix} = \left\{ \prod_{r=1}^{q} \begin{bmatrix} \cos\delta_r & i\frac{\sin\delta_r}{y_r} \\ i\,y_r\sin\delta_r & \cos\delta_r \end{bmatrix} \right\} \begin{bmatrix} 1 \\ y_m \end{bmatrix} \tag{71}$$

Where $\delta_r = 2\pi N_r d_r \cos\frac{\theta_r}{\lambda}$, the admittance of the medium r is $y_r = N_r \mathcal{Y}_0$, and the suffix m denotes the substrate. If the angle of incidence θ_0 is given, the values of θ_r can be found from Snell's Law.

Chapter 3. Materials and Methods

This chapter resumes the reported optical properties of the materials SiO_x, Nb_2O_5, and SiO_2 that led us to manufacture antireflective coatings for near-infrared. Besides, an overview of the deposition techniques and characterization equipment used in this thesis will be made.

Figure 11 shows a diagram with the methodology and the materials used for this thesis. The first stage was the simulation of several AR designs, from 1 to 5 layers using various materials and centered at different wavelengths. From the whole set, the most suitable designs and materials were selected for manufacturing. Only double-, triple- and four-layer designs were fabricated using Nb_2O_5, SiO, SiO_2, and Al_2O_3.

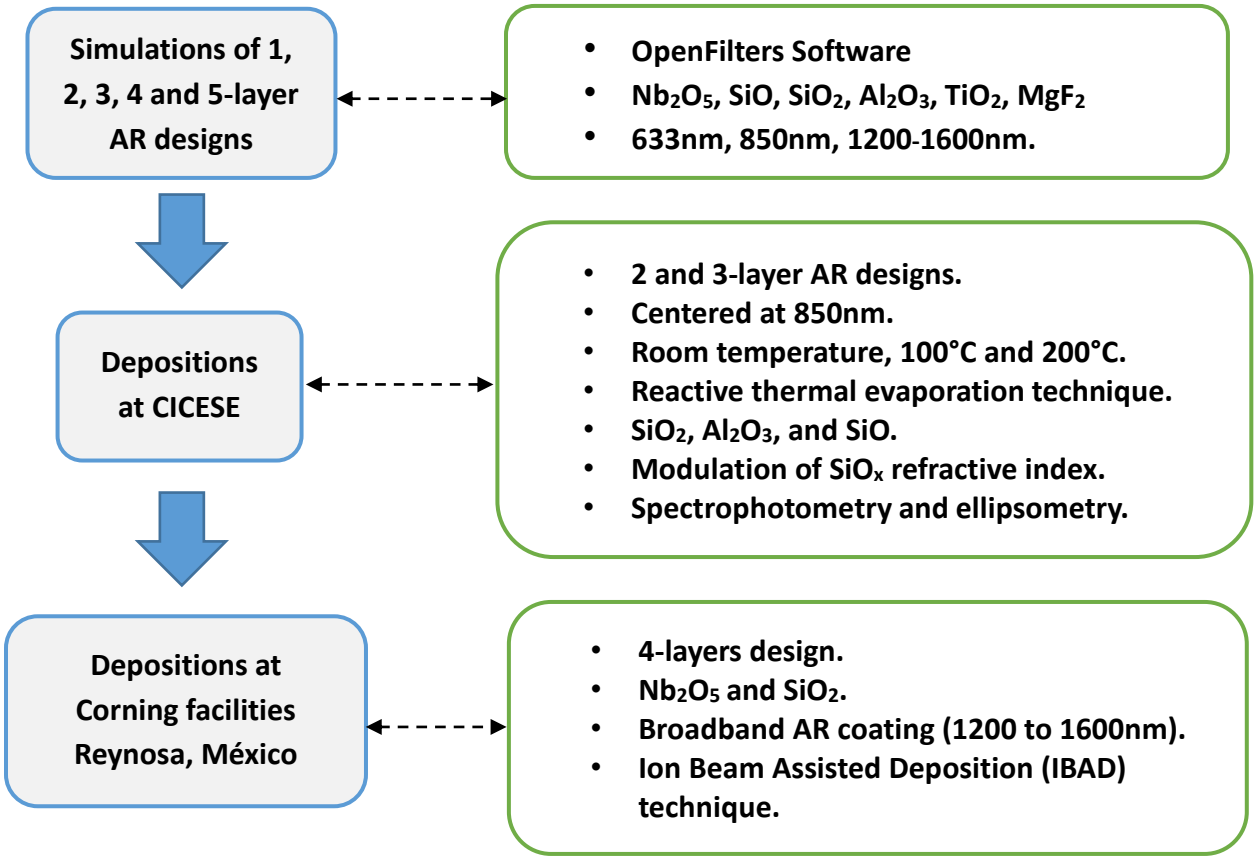

Figure 11 Flowchart showing the methodology of the thesis: simulations, experiments, synthesis techniques, characterization equipment, and materials used for the project.

The experiments were divided into two locations, CICESE and Corning Reynosa facilities, each of them used a different deposition technique (which will be reviewed later) and had different scopes. Corning Reynosa had the objective of fabricating a four-layer broadband antireflective (BBAR) coating design using niobia (Nb_2O_5) and silica (SiO_2) for the range from 1200 to 1600nm to cover both current primary fiber optical communication lines: 1310 and 1550nm. On the other hand, at CICESE were deposited double- and triple-layer AR designs using silicon monoxide (SiO), alumina (Al_2O_3), and silica (SiO_2) refractive indices; these centered at the third communication line, 850nm. The main highlight of this deposition is that it was evaporated only one material, SiO, to obtain the refractive indices similar to silica and alumina; this is possible using the modulation of the SiO_x refractive index, which will be explained in detail later.

The SiO_x ($1 < x < 2$), niobium pentoxide or niobia (Nb_2O_5), and silica (SiO_2) thin-films have been widely studied during the last decades due to their importance for silicon-based optoelectronic devices and their numerous technological applications. Such as protective coatings, thin-film solar cells, passivation layers in sensors, dielectric films in capacitors, interlayers in microelectronics, etc.

3.1 Niobium pentoxide (Nb_2O_5)

Niobium oxide is one of the important strategic high technology group V-B oxide materials. Of all the different niobium oxides such as NbO, NbO_2, and Nb_2O_5, the niobium pentoxide (also called niobia) is the thermodynamically stable form with the lowest free energy formation. It is a transparent dielectric material and has the highest most-stable oxidation number. Niobium pentoxide films have unique physical and chemical properties such as very low optical absorption and high refractive index (~ 2.23) in the visible and near-infrared range (Figure 12a), excellent chemical stability, corrosion resistance, and high transparent ratio in the UV-vis-NIR (ultraviolet-visible near-infrared) region (Figure 12b). It has superior thermal stability and mechanical resistance compared to traditional high index material (e. g., TiO_2). Also, niobium pentoxide thin films have potential applications in high-index and low-loss materials for high-quality optical devices. Some examples are interference filters, antireflection coatings, gas-sensitive materials, waveguide type second harmonic devices, and protection of UV sensitive materials (Usha et al., 2015).

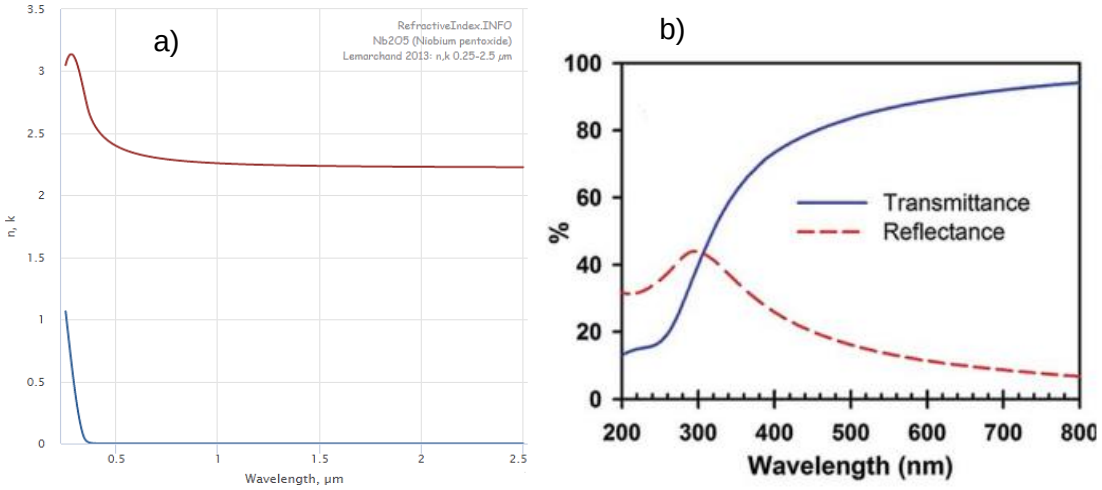

Figure 12 (a) Refractive index and absorption coefficient of Niobium pentoxide. Taken from Lemarchand (2013); (b) Reflectance (dashed curve) and transmittance (solid curve) vs. wavelength spectra Nb_2O_5. Taken from Dash et al. (2015).

3.2 Silica (SiO_2)

Silicon dioxide is the low-index (~1.45), low absorption material used in combination with high-index oxide layer coatings that operate in the UV (~200 nm) to IR (~3 µm) regions. Typical applications include antireflection coatings for near-UV laser optics, all-dielectric mirrors, beam-splitter, bandpass filters, and polarizers. Silica can be used in combination with specific high-index layers, for example, hafnia (HfO_2), zirconia (ZrO_2), niobia (Nb_2O_5), and tantala (Ta_2O_5), to form multilayer structures with high damage thresholds for specialized UV laser applications. Silica films sometimes are useful in promoting adherence between two dissimilar materials, especially oxide-compositions. In contrast to the parent quartz form, silica films are amorphous and never obtain the equivalent density, hardness, or water impermeability of the crystal form.

Completely oxidized silica films are absorption-free over the range below ~250 nm to at least 5µm. Film layers are amorphous and smooth. High mechanical compressive stress limits the thickness of the single-layer thickness. When starting from silica pieces, little dissociation and oxygen loss occur during evaporation, and it is not always necessary to provide a background pressure of oxygen to obtain low-absorbing films. Adhesion is good to glass, most other oxides, and some polymers. The films generally grow with an amorphous structure and relatively high packing density, so they exhibit minimum index changes when vented to moist air. The refractive index is maximized, and the water band absorption is minimized with high energy deposition techniques such as IBAD or sputtering, and high substrate

temperature. Low absorption SiO_2 films can be produced by oxidizing silicon monoxide in a reactive oxygen background. (Materion, 2000).

The refractive indices are dependent on the degree of oxidation, the substrate temperature, and the deposition energy. Figure 13 shows the typical values.

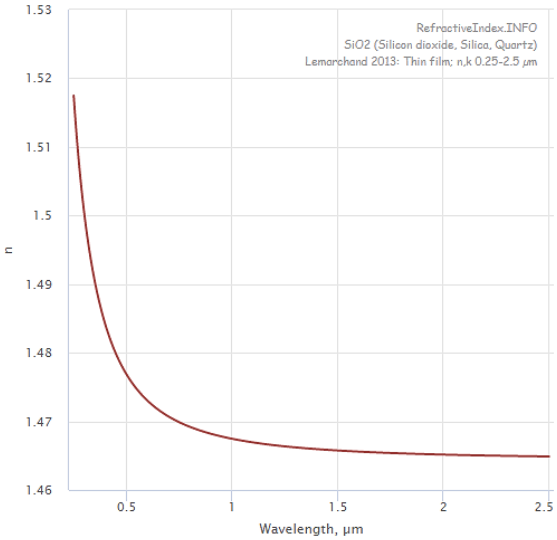

Figure 13 Refractive index vs. wavelength of silica (SiO_2). Taken from Lemarchand (2013).

3.3 Non-stoichiometric silicon oxide (SiO_x)

The features of an evaporated SiO_x film are highly dependent on the fabrication process. For example, for films prepared by physical vapor deposition (PVD) of SiO as source material -as in this thesis work-, their optical and physical properties are sensitive to the fabrication conditions (E. G. Lizarraga-Medina et al., 2015). So, different pressures in a vacuum chamber and different deposition rates can lead to films of different compositions. That means the relation $x = O/Si$ changes as the pressure or the deposition rate is manipulated (Figure 14). The easiest way to manage the vacuum in a chamber is to introduce oxygen gas into the vacuum chamber, that is, creating reactive evaporation of SiO in oxygen, and the deposition rate can be changed by tuning the current that heats the boat containing the SiO.

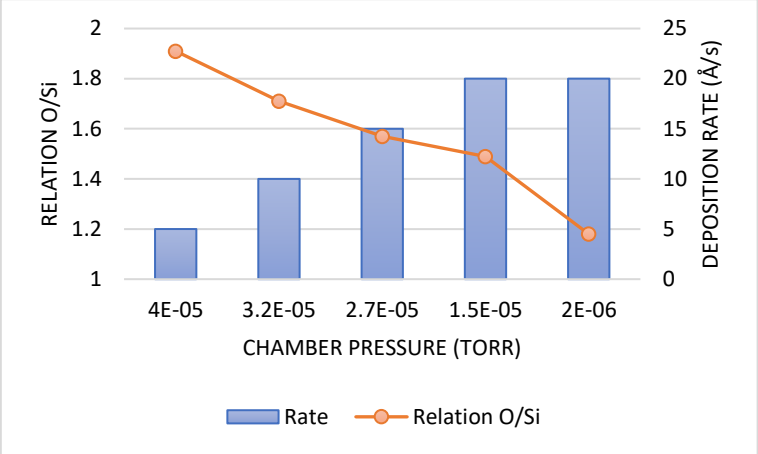

Figure 14 Relation between $x = O/Si$, chamber pressure, and deposition rate in reactive evaporation of SiO. The graph is based on the work reported by O'Leary and Thomas (1987).

As we said before, as the composition of a SiO_x film is different, it will present other optical and physical properties. For example, Durrani et al. (2003) reported that the refractive index of a deposited SiO_x thin films increases as the stoichiometric relation x decreases (Figure 15a). This x value approaches to 1 when the film composition has more silicon or equivalently, the oxygen content decreases. Consequently, the refractive index and other optical properties tend to get similar to SiO. On the other hand, when the x value tends to 2, the evaporated material will present a behavior SiO_2-like. This refractive-index-tuning will bring changes in optical properties like transmittance (Figure 15b).

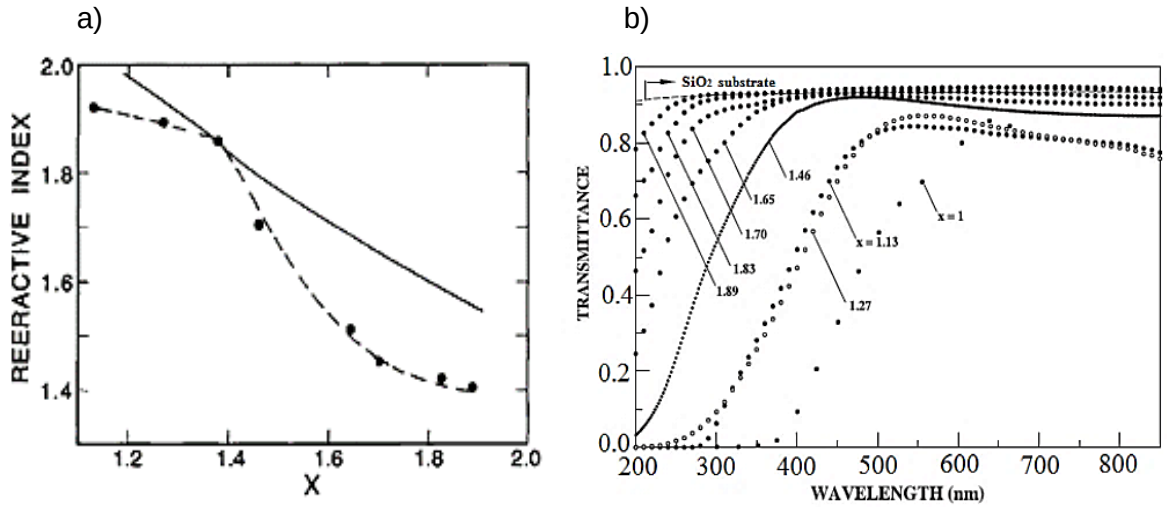

Figure 15 (a) Refractive index (at a wavelength of 630 nm) of SiO_x as a function of stoichiometry x from O'Leary and Thomas (1987) (solid line) and Durrani et al., (2003) (dashed line). (b) Transmittance spectra of an uncoated SiO_2 substrate and SiO_x films with different values of x.

In thin-films design, one of the essential properties of the material to be used is the complex refractive index $N = n - ik$ at a specific reference wavelength. For SiO_x, again, those values depend mainly on the stoichiometry of the evaporated films, which means the value of x. Durrani et al. (2003) have reported the relations called dispersion curves for refractive index n and absorption coefficient k for different values of x (Figure 16), where we can observe how the value of the refractive index is inversely proportional to x. Some values of x have been omitted given the similarity to its neighbors.

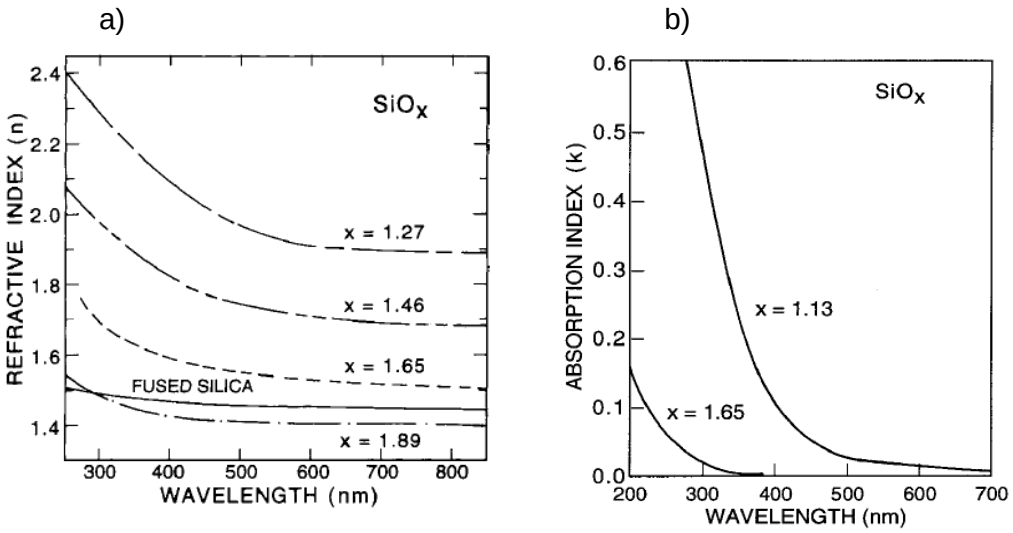

Figure 16 Plots for (a) refractive index and (b) absorption coefficient versus wavelength for SiO_x films with different stoichiometric values of x.

More recent studies about the modulation of the stoichiometric value of x in SiO_x thin-films have been done. Salazar et al. (2016) from CICESE Optics Department deposited SiO_x films by varying the deposition rates at two different vacuum pressures: low vacuum (10^{-4} Torr) and high vacuum (10^{-6} Torr), using SiO as source material. Figure 17 shows the spectral transmittance of SiO_x coatings fabricated at different deposition rates. Films obtained at low vacuum pressure have similar curves with a slight decrease in transmittance value for higher evaporation rates; see Figure 17a. On the other hand, Figure 17b shows how, at a high vacuum, the spectrum presents the typical interference oscillations related to the thin-film thickness; the thicker the film, the more fluctuations. The spectral transmission curves of SiO_x films shown in Figure 17 exhibit a transmission shift towards longer wavelengths; this shift can be associated with the amount of silicon (Si) in the film (Shabalov and Feldman, 1983).

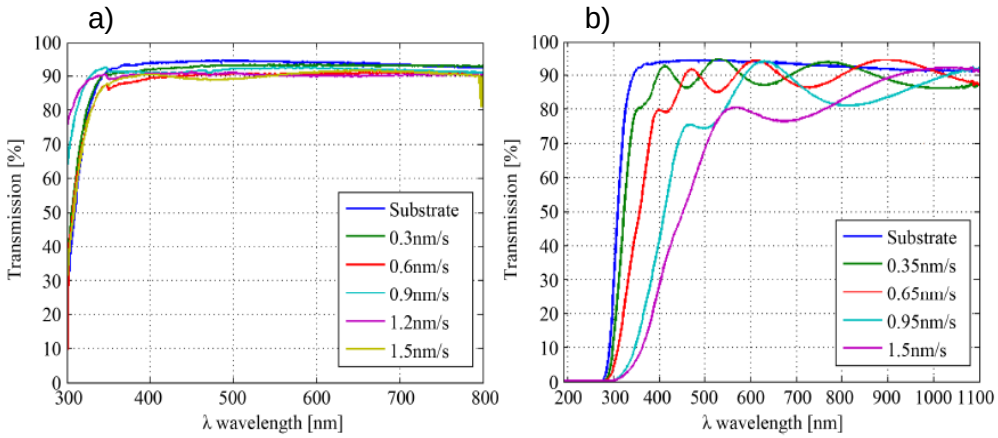

Figure 17 Spectral transmittance of SiO_x films under (a) low vacuum and (b) high vacuum pressure.

The dispersion curves shown in Figure 18 represent the relationship between refractive index n and the evaporation rates: the refractive index value increase as the evaporation rate increases. Given that the films were characterized by ellipsometry, a dielectric modeling procedure is needed. Some dielectric models used by Salazar et al. (2016) were Cauchy and Tauc-Lorentz.

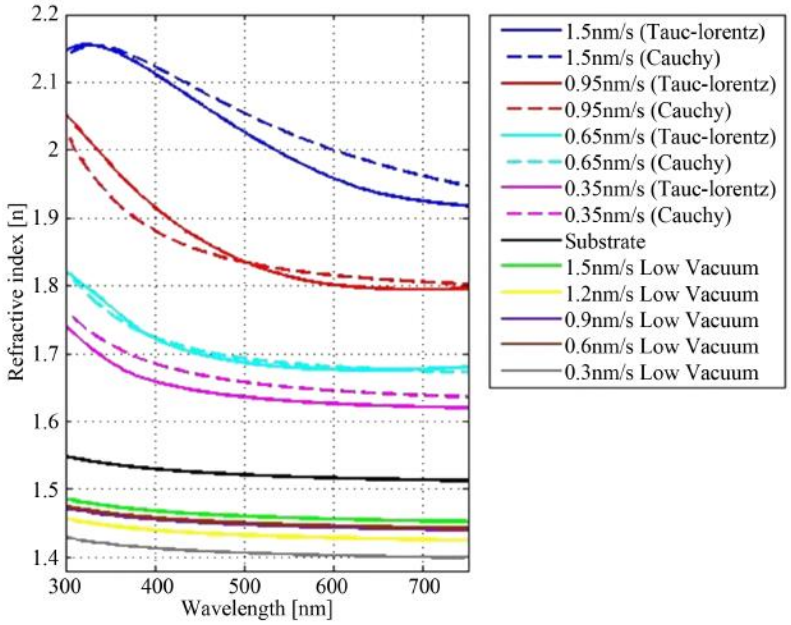

Figure 18 Plot of refractive index versus wavelength for SiO_x at different evaporation rates and vacuum pressures chamber.

Modulation of the refractive index of SiO_x films can still be possible if only one variable during the process was manipulated. Salazar et al. (2016) also reported what happens when the high vacuum pressure chamber (10^{-6} Torr) was fixed, and only the evaporation rate is tuned (Figure 19). The refractive index values are within a range from 1.6 to 1.95; higher n values were obtained at a higher evaporation rate, as expected. At higher deposition rates, the oxidation in the films is avoided, and the stoichiometry and refractive index approached to a SiO-like coating, that is, with x=1.

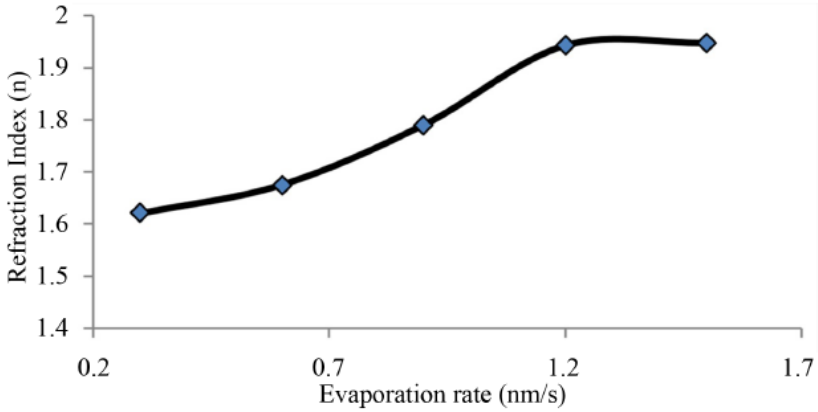

Figure 19 Refraction index for different evaporation rates; the vacuum pressure chamber was set to 10^{-6} Torr, and the reference wavelength is 633nm.

3.4 Simulation of antireflective (AR) coatings

Once the potential materials to be used in the coatings are selected, and prior to the synthesis step, it is convenient to make simulations of the designs using specialized software to try to anticipate the experimental result. Besides, a simulation works as a point of reference to compare the experiment versus the theory.

For this thesis, an open-source software called *OpenFilters* created by Stéphane Larouche and Ludvik Martinu from the Montreal Polytechnique School was used to analyze the optical performance of the coatings. This software allows the creation of multilayer filters and calculation of absorption, phase, admittance diagram, electric field distribution, and generation of reflection, transmission, and ellipsometric monitoring curves (Larouche and Martinu, 2008).

As shown in Figure 20, a classical optical filter consists of a stack of layers of thicknesses d_q and indices of refraction N_q between an incidence and an exit media of indices of refraction N_{inc} and N_{ex}, respectively.

OpenFilters calculates the filter's optical properties using the characteristic matrix approach, just as seen in the Theoretical Basis section. In this approach, the qth layer is represented by

$$M_q = \begin{bmatrix} \cos\delta_q & i\frac{\sin\delta_q}{y_q} \\ i\,y_q \sin\delta_q & \cos\delta_q \end{bmatrix} \tag{72}$$

Where

$$\delta_q = \frac{2\pi N_q d_q \cos\theta_i}{\lambda} \tag{73}$$

is the phase shift of the wave inside the filter, θ_i is the angle of propagation in the layer, and λ is the wavelength in the vacuum.

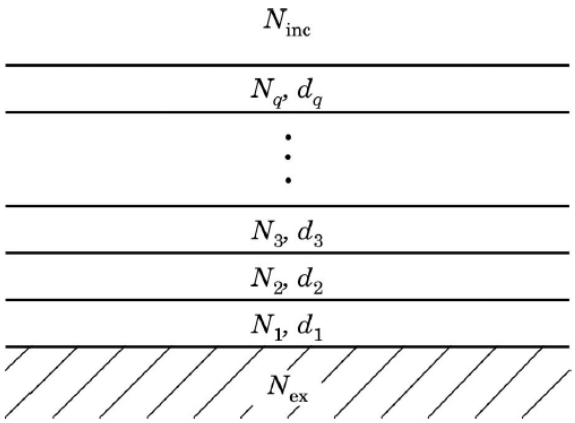

Figure 20 Multilayer optical filter. The image was taken from Larouche and Martinu (2008).

3.5 Manufacturing techniques

Both academic research and industry have fabricated thin films made of SiO_x, Nb_2O_5, or SiO_2 during the years using different techniques, classified into physical (PVD) or chemical (CVD). PVD involves vacuum deposition processes in which one or more of the depositing species are evaporated from a solid source in the coating chamber. On the other hand, in CVD, there are chemical reactions that transform gaseous molecules – called precursor – into a solid material, in the form of thin-film or powder, on a substrate's surface. In the present thesis, the coatings were deposited using two different variations of PVD techniques; those will be discussed below.

3.5.1 Physical Vapor Deposition (PVD)

In PVD, a solid source material is vaporized atom by atom, or molecule by molecule, and deposited on the substrate at a controlled rate in a vacuum environment. Typically, PVD processes are used to deposit films with thicknesses in the range of a few nanometers to thousands of nanometers; however, they can also be used to form multilayer coatings. Typical PVD deposition rates are 1–10 nanometers per second. The main categories of PVD processing are vacuum deposition (or thermal evaporation), sputter deposition, arc vapor deposition, ion plating, and Ion Beam Assisted Deposition (IBAD), as depicted in Figure 21 (Mattox, 2009).

The major difference between PVD techniques is the way that the vapor flux is generated from a target made of a specific material. Simultaneously, one or more gases may also be introduced to modify either the vapor species or the growing film chemically. In reactive deposition processes, compounds are formed by the depositing material's reaction with the ambient gas environment, such as oxygen or nitrogen. The used methods for this thesis objectives have been *reactive thermal evaporation* and *ion-beam assisted deposition*. So, the focus will be on them. The latter is also part of a subgroup called energetic processes.

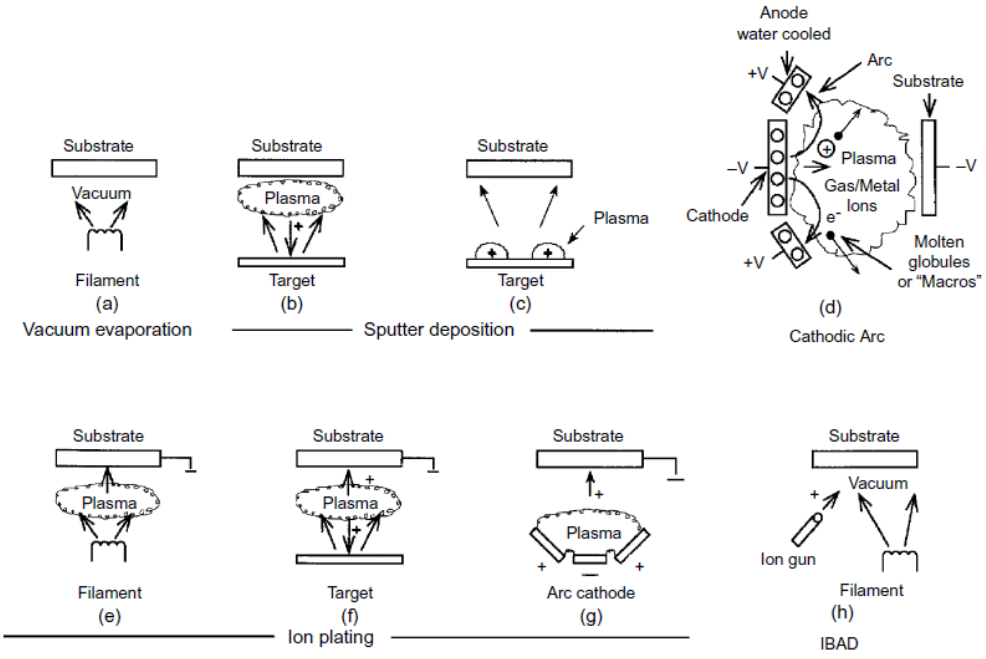

Figure 21 PVD processing techniques: (a) thermal evaporation, (b) and (c) sputter deposition, (d) cathodic arc, ion plating with: (e) plasma environment in thermal evaporation source, (f) and sputtering source, (g) arc vaporization source, and (h) ion beam assisted deposition.

3.5.1.1 Thermal Evaporation

Thermal evaporation is a PVD process where atoms and clusters of atoms or molecules are removed in the form of a vapor flux from a metal crucible, containing some bulk material (source) by heating the crucible, either by passing a current through it or by a heater filament (Figure 22). In a typical thermal evaporation process, the source material is heated by the Joule effect to an appropriate temperature at which there is considerable vapor pressure. Standard resistive heating elements are carbon, molybdenum, tantalum, and tungsten/wolfram (Martín-Palma and Lakhtakia, 2013).

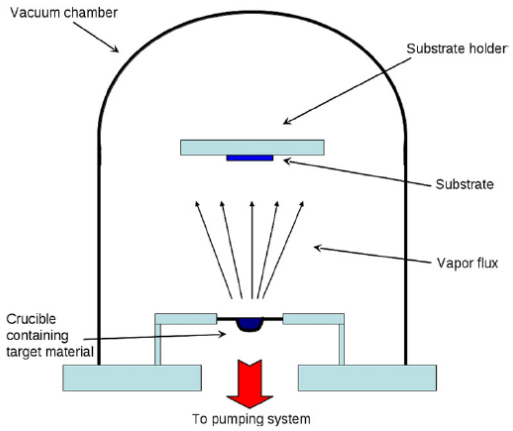

Figure 22 Schematic of a typical thermal evaporation system. The source material is heated by electrical current.

Thermal evaporation usually requires a vacuum better than 10^{-4} Torr to have a long mean free path between collisions. At this pressure, there is still a large amount of concurrent impingement on the substrate by potentially undesirable residual gases that can contaminate the film. Because of the reduced pressure in the chamber, the vapor is given off in an even stream, the molecules appearing to travel in straight lines so that any variation in the thickness of the film that is formed is smooth and depends principally on the position and orientation of the substrate with respect to the vapor source.

Thermally evaporated films usually exhibit tensile stress resulting from the disorder frozen into the film, as freshly arriving material covers what already exists. An increase in the deposition rate gives less time for the material on the surface to reorganize itself and, therefore, should lead to an increase in tensile stress (MacLeod, 2001).

Thermal evaporation deposition has advantages and disadvantages compared to other PVD techniques. Benefits, in some cases:

- A line-of-sight deposition allows the use of masks to define areas of the deposit.
- High deposition rates can be obtained.
- Deposition rate monitoring is relatively easy.
- Vaporization source material can be in many forms, such as chunks, powder, wire, chips, etc.
- The vaporization source material of high purity is relatively inexpensive.
- High purity films are readily deposited from high purity source material since the deposition ambient can be made as non-contaminating as is desired.

Disadvantages, in some cases:

- Line-of-sight deposition gives poor surface coverage over a large area and poor uniformity.
- Low ability to deposit many alloys and compounds.
- High radiant heat loads during processing.
- Poor utilization of source material.
- Non-optimal film properties – e.g., pinholes, less than bulk density, columnar morphology, high residual film stress. –

The thermal evaporation of non-absorbing film layers of oxide compounds requires oxidation of the source material to obtain the desired composition; this is done by introducing activated oxygen to the reactive process. The chemical state of the starting material might be fully oxidized or be reduced to a sub-oxide. The low-index oxide common to all oxide coating combinations is SiO_2. Silicon dioxide can be deposited by evaporation of silica or by reactive oxidation of SiO (Pellicori, 1984). Today SiO is used mostly for multilayer coatings in the infrared range (Kaiser and Pulker, 2003).

3.5.1.2 Features of manufacturing by thermal evaporation

The deposition of films by this technique was done in a thermal evaporation machine BOC Edwards Auto-500 (Figures 23 and 24) located at CICESE facilities in the Thin-Films Laboratory.

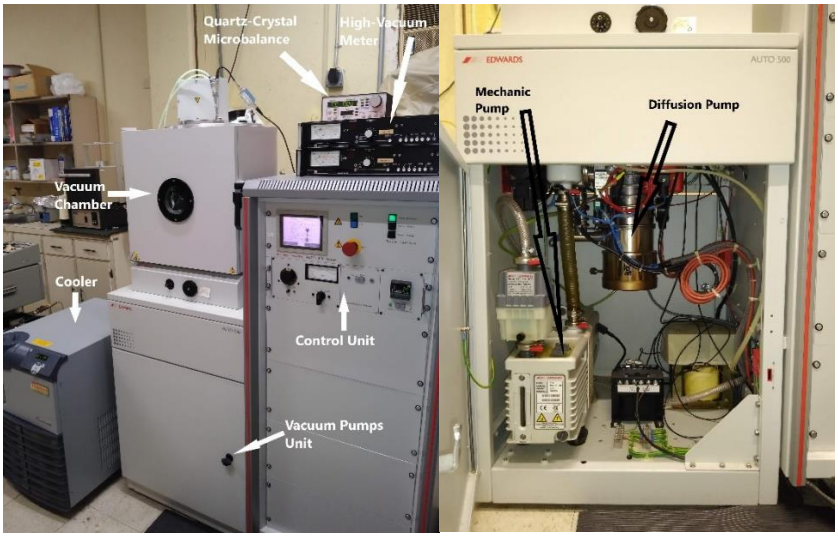

Figure 23 Thermal evaporation machine BOC Edwards Auto-500 (left), and view of vacuum pumps (right).

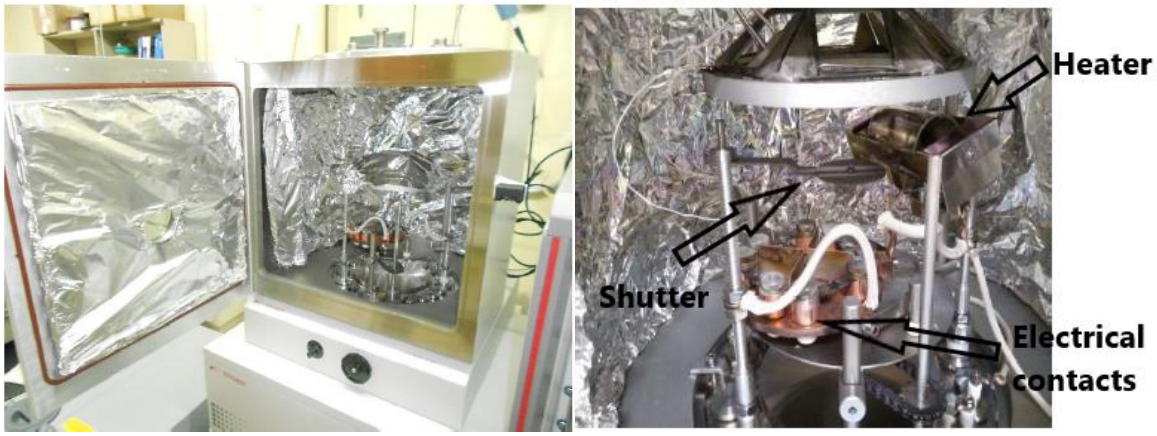

Figure 24 The inside of the vacuum chamber.

The main objective of the depositions performed in CICESE was to develop a pair of double-layer and one triple-layer AR designs at 850 nm as the reference wavelength. The highlight of these was that all the different values of refractive indices used in the designs were obtained using the SiO_x index modulation – from 1.47 (~SiO_2) to 1.92 (~SiO) – by evaporating only one material and changing the process parameters (vacuum, deposition rate, and temperature). Thus, an analysis of their effect on the samples' optical properties was done to set the conditions to have a better control of the synthesis results. Furthermore, determine their viability for AR coating usage.

The material evaporated in this index-modulation process was silicon monoxide (SiO) brand Balzers, with 99.5% purity and grain size of 5 – 8 mm (Figure 25), and deposited on silica substrates brand FOCTEK of 10 mm x 7.5 mm x 1 mm.

Figure 25 Grains of silicon monoxide (SiO) with a refractive index of 1.95 used for thermal evaporation; its refractive index was modulated by manipulating the synthesis parameters during evaporation.

The SiO was evaporated by heating molybdenum boats (Figure 26), and the deposition rate and thickness were monitored by a quartz-crystal microbalance of the company INFICON model SQM-160.

Figure 26 Molybdenum boat used to evaporate the SiO grains

The base pressure for the whole set of depositions was $\sim 1\ x10^{-6}$ Torr. As we have already discussed, this same value was used to obtain SiO-like refractive index and Al_2O_3-like refractive index, given that it could be considered a high-vacuum for this application. On the other hand, to get a SiO_2-like index value, we need a low-vacuum. So, the pressure was increased from the base value to $\sim 1.5\ x10^{-4}$ Torr by adding ultrapure oxygen into the chamber.

3.5.2 Energetic processes

The energetic processes are the ones that involve considerably greater energies than thermal. Thin films deposited by thermal evaporation have a pronounced columnar structure that is a significant cause of coating instability and drifts. The idea behind the energetic processes is to disrupt the columnar structure with its accompanying voids by supplying extra energy, and this does work well. Although we describe the processes as energetic, it has been shown that momentum is the critical quantity. The improvements are achieved at comparatively low substrate temperatures, which helps with plastic substrates' difficult coating.

It has been theoretically demonstrated by advanced computer modeling that the significant effects are due to the additional momentum of the molecules, either supplied by collisions with the incoming energetic ions or derived from the additional kinetic energy of the evaporant. Experimental evidence shows a correlation of the effects with momentum rather than the energy of the bombarding ions. These processes' significant benefits are the increased packing density of the films, making them more bulk-like and hence increasing their ruggedness, the improved adhesion resulting from a mixing of materials at the interfaces between layers, and a reduction of the sometimes relatively high tensile stress in the layers. The increase in packing density also reduces moisture sensitivity and can actually eliminate it (MacLeod, 2001).

3.5.2.1 Ion Beam Assisted Deposition (IBAD)

The simplest of the energetic processes is termed ion beam assisted deposition, or IBAD (Figure 27). The IBAD process is not a deposition technique, per se. Instead, it is a technique wherein ion bombardment is combined with another PVD technique. For this thesis, the PDV technique used is electron beam evaporation.

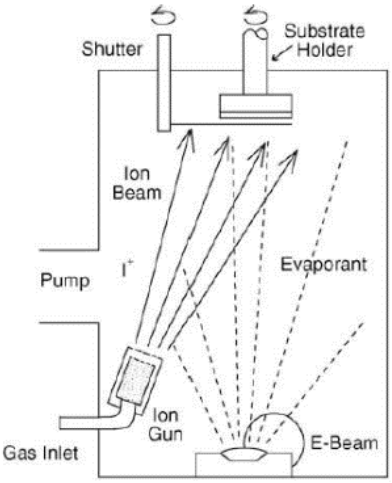

Figure 27 Ion Beam Assisted Deposition (IBAD).

The evaporated species produced by the chosen PVD technique are simultaneously impinged by an independently generated flux of ions. Thus, while the individual atoms or molecules condense on the substrate to form a thin film, highly energetic ions (typically from 100 to 2,000 eV) are produced and directed at the growing thin film (Martín-Palma and Lakhtakia, 2013). The energetic particles used for bombardment are usually ions of inert gas.

The ions extracted from the source are positive and would rapidly charge any dielectric material preventing further bombardment. Thus, sufficient electrons to neutralize this charge are therefore added to the extracted beams yielding what is usually termed a neutral ion beam. In the early work, mostly argon was used as the bombarding species, but a much more extensive range is used today (Piegari and Flory, 2013).

The effect of IBAD on the coating depends on many parameters such as ion energy, ion to atom arrival ratio, angle of ion incidence, pressure, and temperature. The main advantage of IBAD is that it allows adherent coatings to be applied at low temperatures (Santecchia et al., 2015). The concurrent ion bombardment significantly improves adhesion and permits control over the morphology, density, internal stresses, crystallinity, and chemical composition of the thin film. Ion bombardment can also blend together coating and substrate atoms. The energy and flux of bombarding ions can be exploited to modify the size and crystallographic orientation of grains. For best results, it is essential that the bombardment be continuous between the cleaning and the deposition portions of the process to maintain an atomically clean interface.

Energy from the bombarding particle will be deposited in a very small area/volume but will represent a very high local temperature. The amount of energy available locally can determine how an adatom nucleates and condenses. If the amount of energy is small – as in the case of thermally evaporated atoms (condensation energy)–, the adatom will be quenched in position before it reaches its lowest energy configuration. Hence, the deposit will be less than fully dense, have tensile stress, and develop a columnar structure. If bombardment adds a small amount of energy (a few eV), the adatom will have higher surface mobility and, in some cases, may develop an epitaxial structure. At higher bombarding energies, the adatoms and surface atoms are knocked about, thus densifying the deposited material (Figure 28). However, if the atoms are stuffed into the atomic structure by too much bombardment, they will develop high compressive stress and, in some cases, an unusual atomic arrangement (Martin, 2010).

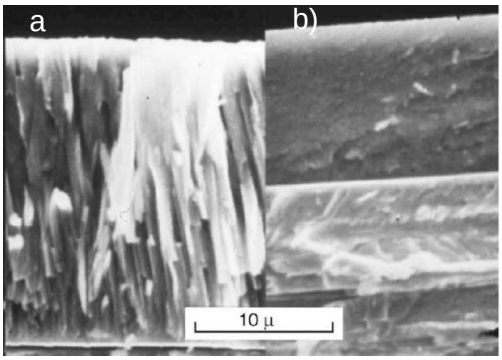

Figure 28 Example of cross-section morphology of a deposit: (a) without and (b) with bombardment.

It was demonstrated that the bombardment in an ion-assisted deposition could improve films' solidity to eradicate their moisture sensitivity. The absence of moisture-induced shifts and, also, because of the high packing density, were significant reasons for the rapid adoption of ion-assisted deposition by industry.

There is a general tendency for the oxides to lose some oxygen in the evaporation process, and the resulting vacancies cause absorption. The oxygen can be restored by adding oxygen to the background atmosphere of the machine in a process termed reactive evaporation. Not enough oxygen and the absorption remains, although reduced; too much oxygen and the packing of the thin film suffers from all the accompanying consequences (Piegari and Flory, 2013).

3.5.2.2 Features of manufacturing by IBAD

The deposition of films by this technique was done in a conventional box coater for ion-assisted e-beam evaporation located in Corning Reynosa México facilities, in the Thin-Films Laboratory. The objective of the depositions in Corning Reynosa was to fabricate a four-layer broadband AR design from 1200 to 1600 nm, with 1430 nm as the reference wavelength. The materials evaporated in this process were silica (SiO_2) and Nb_2O_5 pellets of material (Figure 29) with a purity >99% and deposited on silica substrates. The evaporation was made using an e-beam gun gaussed for 9 kV and current <200 mA.

Figure 29 Pellets of SiO_2 (left) and Nb_2O_5 (right) used to make the four-layer design in the Corning Reynosa facilities.

The chamber's base pressure is 10^{-6} Torr, and the background pressure during evaporation is approximately 10^{-4} Torr**.** The budget of the substrate temperature is supposed to not going over 110°C. Besides, the fluxes of the reactive and inert gasses were 15 and 20 sccm for the O_2 and Ar, respectively. In addition, the machine has an ion-gun aimed at the substrate to improve the packing density of the evaporated films.

3.6 Optical characterization

3.6.1 Spectrophotometry

The basic function of a spectrometer is to take light, break it into spectral components, digitize the signal as a function of wavelength, and read it out and display it through a computer. The first step in this process is to direct light through a fiber-optic cable into the spectrometer through the entrance slit. The light is then collimated by a concave mirror and directed onto a grating. The grating disperses the light's spectral components at slightly varying angles, which are then focused by a second concave mirror and imaged onto the detector array (see Figure 30).

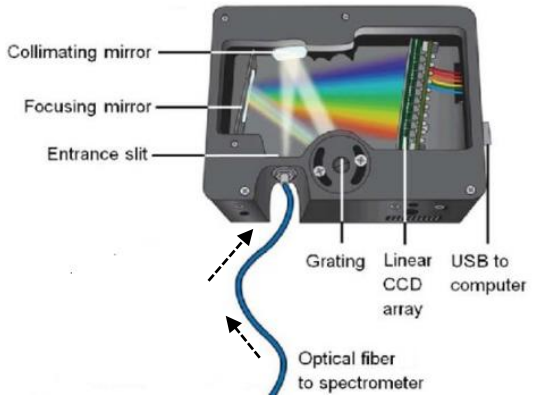

Figure 30 Typical optical components in a spectrometer. The arrows show the direction of propagation of light. Image taken from Regnima et al. (2017).

Once imaged, the photons are converted into electrons that are digitized and read out through a USB or serial port to an external computer. A software interprets the signal based on the number of pixels in the detector and the linear dispersion of the diffraction grating to create a calibration that enables the data to be plotted as a function of wavelength over the given spectral range. These data can then be used and manipulated for many different spectroscopic applications.

The spectrometer used to measure the AR samples' spectral transmittance deposited at CICESE was the *OceanOptics Red Tide USB650* (Figure 31). On the other hand, the one used to measure the spectral reflectance at the Reynosa facilities was the *Filmetrics F10-AR* (Figure 31).

Figure 31 Spectrometers used for the characterization of the fabricated AR samples. At CICESE, was used the OceanOptics Red Tide USB650 (left) to measure the transmittance from 350 to 1000nm. On the other hand, a Filmetrics F10-AR (right) measured the spectral reflectance of the four-layer design fabricated in Corning Reynosa from 380 to 1700nm.

3.6.2 Spectroscopic Ellipsometry (SE)

Ellipsometry is a non-perturbing optical technique that uses the change in the state of light's polarization upon reflection to characterize surfaces, interfaces, and thin films.

In ellipsometry, a collimated beam of monochromatic or quasi-monochromatic light, which is polarized in a known state, is incident on a sample surface under examination, and the state of polarization of the reflected light is analyzed. From the incident and reflected states of polarization, ratios of complex reflection coefficients of the surface for the incident orthogonal linear polarizations parallel and perpendicular to the incidence-plane are determined. These ratios are subsequently related to the structural and optical properties of the ambient-sample interface region by invoking an appropriate model and the electromagnetic theory of reflection. Finally, model parameters of interest are determined by solving the resulting inverse problem (Azzam, 1995).

3.6.2.1 Values measured in ellipsometry

In a typical scheme (Figure 32), the incident light is linearly polarized at a known -but arbitrary- angle, and the reflected light is elliptically polarized. Measurement of the ellipse of polarization of the reflected light accounts for the name ellipsometry.

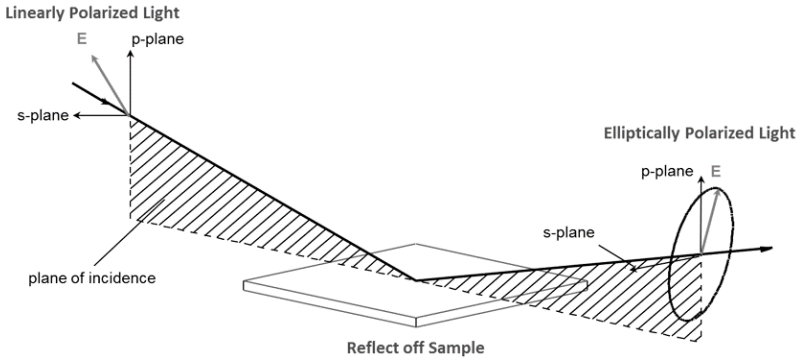

Figure 32 Diagram of ellipsometry

For optically isotropic structures, ellipsometry is carried out only at oblique incidence. In this case, if the incident light is linearly polarized with the electric vector vibrating parallel p or perpendicular s to the plane of incidence, the reflected light is likewise p- and s-polarized, respectively. The associated complex amplitude reflection coefficients are R_p and R_s; given by the Airy formula:

$$R_{p,s} = \frac{R_{1_{p,s}} + R_{2_{p,s}} e^{-2ib}}{1 + R_{1_{p,s}} R_{2_{p,s}} e^{-2ib}} \tag{74}$$

$$b = \frac{2\pi d_f}{\lambda} N_f \cos \phi_f \tag{75}$$

Where d_f is the film thickness, λ is the wavelength of the light, N_f is the complex refractive index of the film, and ϕ_f is the angle of light propagation within the film as determined by Snell's Law. The quantities R_1 and R_2 are the Fresnel reflection coefficients for interfaces 1 and 2, respectively.

Besides,

$$\rho = \frac{R_p}{R_s} \tag{76}$$

Therefore, ellipsometry involves pure polarization measurements (without account for absolute light intensity or absolute phase) to determine ρ. It has become customary to express ρ in polar form in terms of two *ellipsometric angles* ψ and Δ ($0 \leq \psi \leq 90°, 0 \leq \Delta \leq 360°$) as follows:

$$\rho = \tan\psi e^{i\Delta} \tag{77}$$

Where

$$\tan\psi = \frac{|R_p|}{|R_s|} \tag{78}$$

represents the relative amplitude attenuation, and

$$\Delta = \arg(R_p) - \arg(R_s) \tag{79}$$

is the differential phase shift of the p and s linearly polarized components upon reflection. The measured response depends on the optical properties and thickness of individual materials. Thus, ellipsometry is primarily used to determine film thickness and optical constants. However, it is also applied to characterize composition, crystallinity, roughness, doping concentration, and other material properties associated with a change in optical response.

3.6.2.2 Instrumentation

Figure 33 is a schematic diagram of a generic ellipsometer. It consists of a source of collimated and monochromatic light L, polarizing optics PO on one side of the sample S, polarization analyzing optics AO, and a photodetector D on the other side. An apt terminology refers to the PO as a polarization state generator (PSG) and the AO plus D as a polarization state detector (PSD).

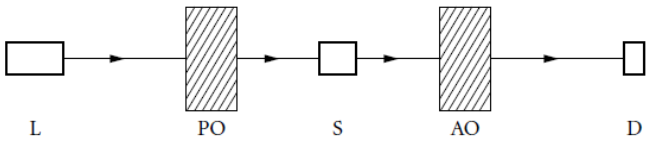

Figure 33 Generic ellipsometer with polarizing optics PO and analyzing optics AO. L and D are the light source and photodetector, respectively.

Figure 34 shows the commonly used polarizer-compensator-sample-analyzer (PCSA) ellipsometer arrangement. The PSG consists of a linear polarizer with transmission-axis azimuth P and a linear retarder, or compensator, with fast-axis azimuth C. The PSD consists of a single linear polarizer that functions as an analyzer, with transmission-axis azimuth A followed by a photodetector D.

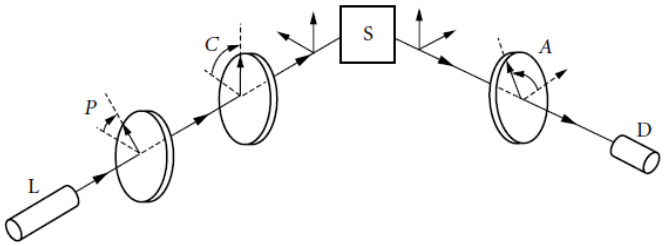

Figure 34 Polarizer-compensator-sample-analyzer (PCSA) ellipsometer. The azimuth angles P of the polarizer, C of the compensator (or quarter-wave retarder), and A of the analyzer are measured from the plane of incidence, positive in a counterclockwise sense when looking toward the source.

There are several possible variations of the optical configuration in the ellipsometer depends on which element is rotating. For this thesis, an ellipsometer J. A. Woollam M2000D (Figure 35) was used for characterization. This equipment uses a rotating compensator ellipsometer (RCE) configuration (Figure 35). This ellipsometer has a spectral range from 193 to 1000nm, and it is located at the UABC campus Mexicali in Dr. Nicola Radnev's laboratory.

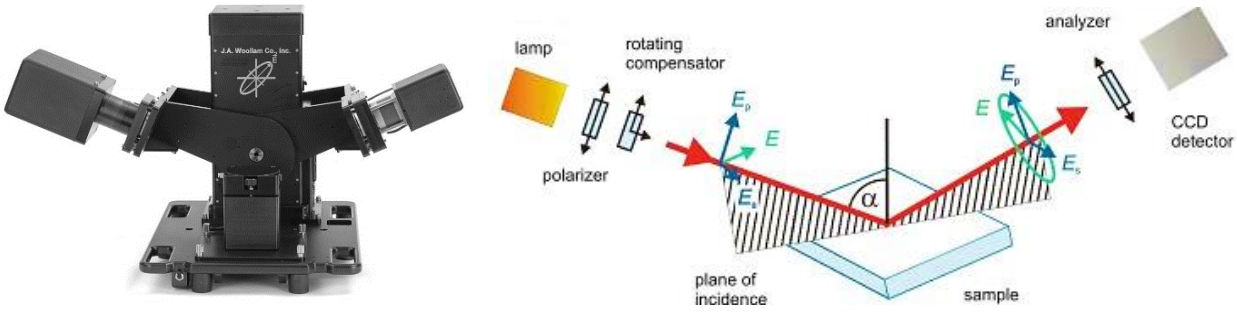

Figure 35 Ellipsometer J. A. Woollam M2000D (left) and its configuration of rotating compensator (right).

Chapter 4. Results and Discussion

This section presents several types of relevant results for the development of each stage of this thesis work (Figure 36): the theoretical antireflective designs, simulations, and synthesis and characterization of the optical properties of the deposited films. Each of them was important to pass to the next step in the project. Based on these results, a discussion of the relevance of this work is presented.

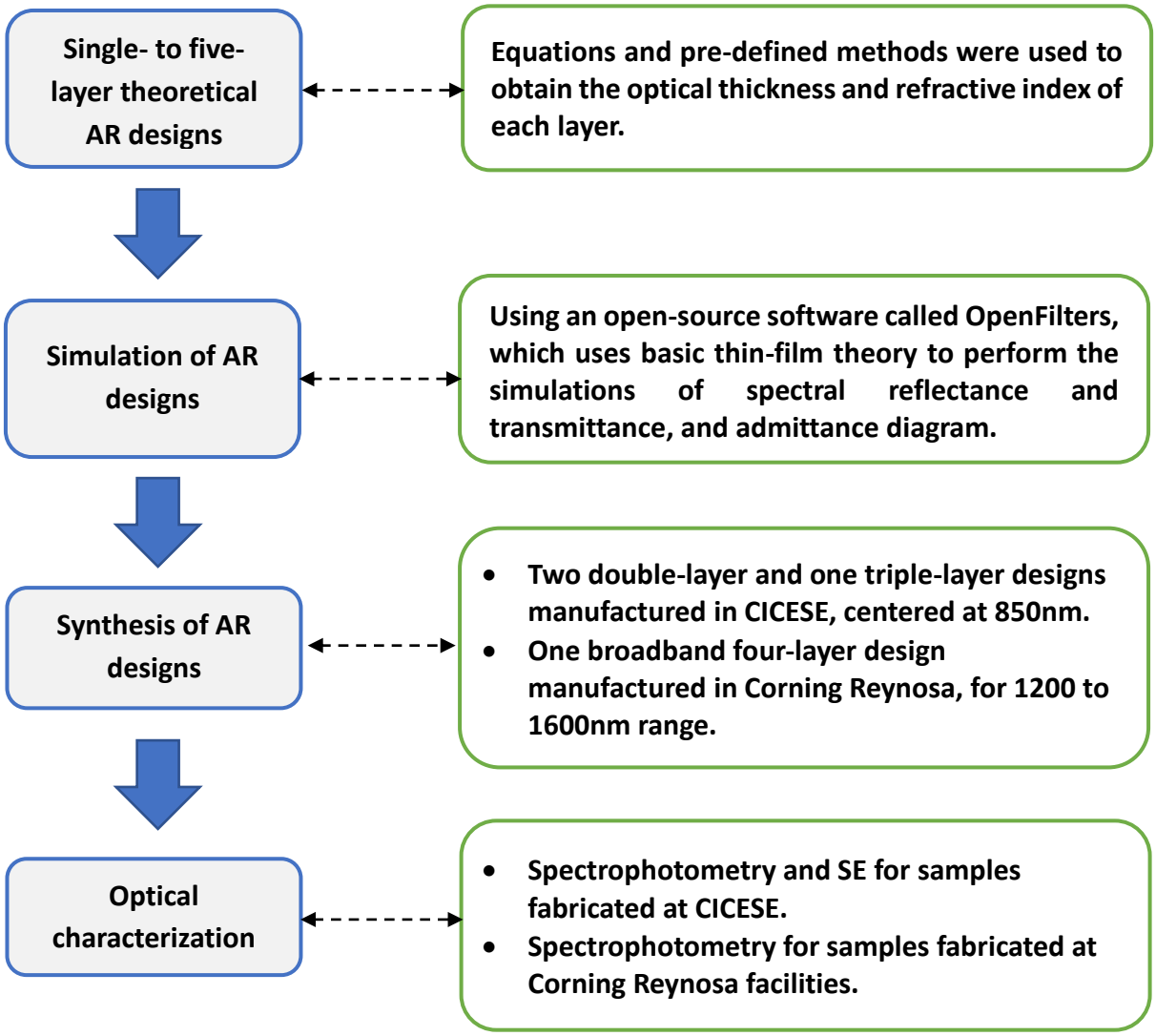

Figure 36 Flowchart of results obtained throughout the thesis project and a brief description of each one. All of them will be explained in detail below.

4.1 Theoretical designs

There are several paths or methods to define either the refractive index or the optical thickness of the layers in the designs to have the lowest reflection possible. They are similar in essence but may be slight variations depends on the number of layers.

4.1.1 Single layer

Single-layer AR coatings are designed so that the relative phase shift between the beam reflected at the upper and lower boundaries of a thin film is 180°. Destructive interference between the two reflected beams occurs, which cancels both beams before they exit the surface (Figure 37).

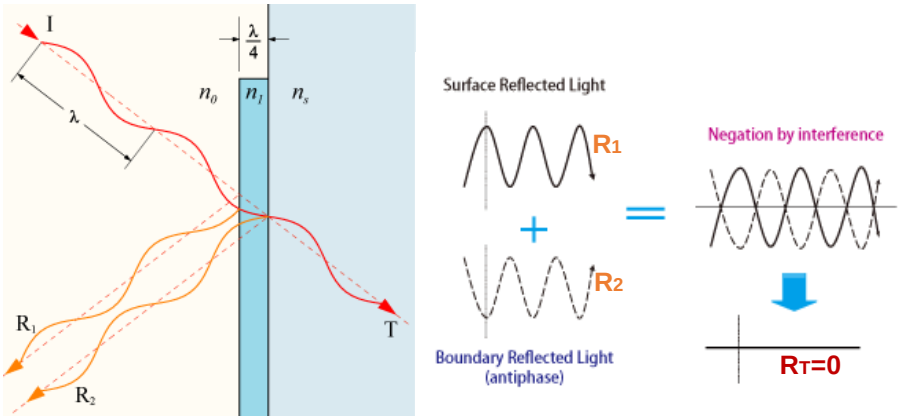

Figure 37 The refractive index and thickness of every coating layer are carefully controlled to cause destructive interference between every reflected beam.

The optical thickness of the coating must be an odd integer multiple of $\lambda/4$, where λ is the reference wavelength. When achieved, this will lead to the cancellation of the beams. The index of refraction of a thin film (n_1) needed for complete cancelation of the reflected beams can be found by using the refractive indices of the incident medium (n_0) and the substrate (n_s).

$$n_1 = \sqrt{n_0 n_s} \tag{80}$$

In this thesis, the incident medium is air ($n_0 = 1$), and the substrate is silica ($n_s = 1.45$). So, the ideal refractive index for the deposited film to have zero reflection will be

$$n_1 = \sqrt{(1.0)(1.45)} = 1.2 \tag{81}$$

However, it does not exist such material with this exact index value. The closest one is the silica-like refractive index I obtained with the modulation of the SiO_x explained earlier, which is ~ 1.47 (Figure 38). Given this difference between the real and the ideal value of the refractive index, the total reflection will not be zero; it is needed to add more layers to decrease the remaining reflection.

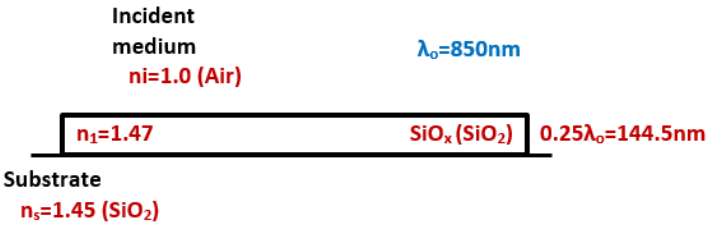

Figure 38 My best approximation of single-layer AR designs because my lowest refractive index material available for the process is $n_1 = 1.47$.

4.1.2 Double-layer

When one more layer of different material is added, you have two paths to follow depend on the availability of materials or even on the type and quality of the deposit monitoring.

1. If you have several materials available in your stock to fabricate, and your monitoring equipment has better results with optical thicknesses of multiples of $\lambda/4$, or the designer just wants to have both layers with an optical thickness of $\lambda/4$, the resulting design will look similar to Figure 39. The index of refraction of the outermost film (n_1) needed for complete cancelation of the reflected beams can be found by using the refractive indices of the incident medium (n_0), the substrate (n_s), and selecting a high-index material available in our stock (n_2) by using

$$n_1 = n_2\sqrt{\frac{n_0}{n_s}} \tag{82}$$

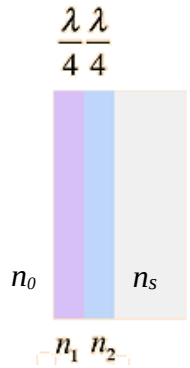

Figure 39 Double-layer AR design with both layers having an optical thickness of $\lambda/4$.

2. However, maybe something similar to the single-layer case could happen if the n_1-n_2 refractive indices combination is not the ideal. So, if your stock of materials is short, you can select the two materials you want to use and, after, calculate an unequal optical thickness for each layer (Figure 40).

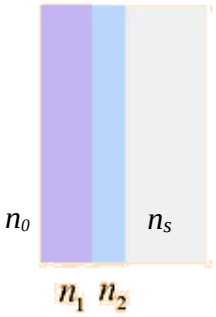

Figure 40 Double-layer AR design with unequal optical thicknesses.

With this configuration, the phase shift in each layer will be different. We can calculate the value of the shifts by using the indices of refraction of the outermost film (n_1), the incident medium (n_0), the substrate (n_s), and the film next to the substrate (n_2). Having the characteristic matrix of two layers and solving for the phase shifts δ_1 and δ_2, we obtain (MacLeod, 2001)

$$\tan^2 \delta_1 = \frac{(n_s - n_0)(n_2{}^2 - n_0 n_s) n_1{}^2}{(n_1{}^2 n_s - n_0 n_2{}^2)(n_0 n_s - n_1{}^2)} \tag{83.1}$$

$$\tan^2 \delta_2 = \frac{(n_s - n_0)(n_0 n_s - n_1{}^2) n_2{}^2}{(n_1{}^2 n_s - n_0 n_2{}^2)(n_1{}^2 - n_0 n_s)} \tag{83.2}$$

For this thesis, the latter option was chosen to have different thicknesses for each film. Figure 41 shows the two different AR designs fabricated in CICESE.

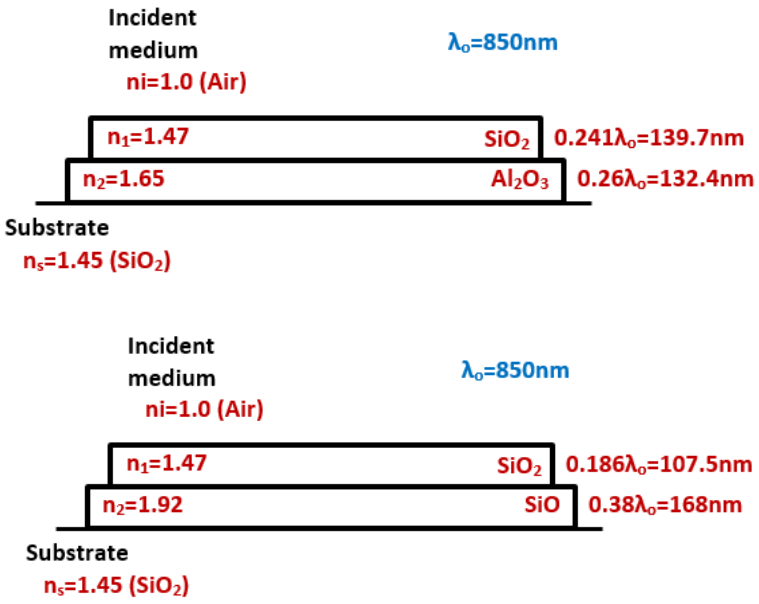

Figure 41 Double-layer designs fabricated for this thesis, both of them having unequal thicknesses. The main difference between them is the refractive index of the material next to the substrate

There is little further improvement in performance that can be achieved with two-layer coatings, given the limitations existing in usable film indices. For higher performance and broader bandwidth, further layers are required.

4.1.3 Triple-layer

As well as for the previous cases, a triple-layer AR coating design has several ways to be designed: all layers having an optical thickness of $\lambda/4$, all of them having different thicknesses using a method developed by Thetford (1969), or a configuration called quarter-half-quarter (QHQ). Designs with all-unequal thicknesses probably have lower reflectivities at the reference wavelength. However, the QHQ design has been a very common and significant configuration for several decades. So, in order to honor its importance, the QHQ was selected for this thesis.

The quarter-half-quarter AR design (Figure 42), as its name suggests, is formed by two layers with an optical thickness of $\lambda/4$, and between them, one layer with an optical thickness of $\lambda/2$ (also called broadening layer).

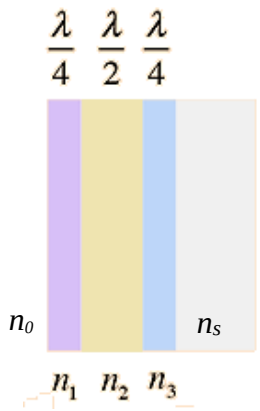

Figure 42 Quarter-half-quarter AR design

The arrangement consists of a layer of intermediate index next to the substrate, followed by a high-index layer and finally by a low-index layer on the outside. To achieve the broadening effect, the half-wave layer must be of a high index (2.0 or more). Good results are obtained with values of the refractive index of the half-wave layer in the range 2.0–2.4. Cox et al. (1962) investigated the effect of varying the index of the quarter-wave layers. They found that for the best results on crown glass, the outermost layer index should be between 1.35 and 1.45, and the innermost layer index between 1.65 and 1.70. The outermost layer is the most critical in the design.

A half-wave layer acts as an absent layer; that means its admittance plot ends where it began (it forms a complete circle) in the admittance diagram. The closest the outermost layer admittance ends from the admittance of the incident media (in this case, air, n=1.0), the lower the reflectivity at the reference wavelength. For this reason, even when the half-layer is an absent layer, if there are small variations in the layers' thicknesses, the admittance of the outermost layer will not be dragged so much from its original location if it is located next to the half-wave layer. For this reason, the broadening layer is situated in the middle.

The quarter-half-quarter coating is certainly the most significant of the early multilayer coatings for low-index substrates. It has had considerable influence on the development of the field (MacLeod, 2001). For this thesis, the triple-layer AR design fabricated in CICESE is shown in Figure 43.

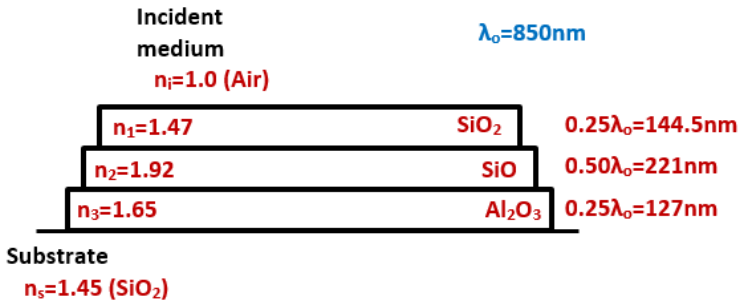

Figure 43 Quarter-half-quarter (QHQ) design fabricated for this thesis. To achieve the broadening effect, the half-wave layer must be high index and situated in the middle.

4.1.4 Four- and five-layer

The greater the number of layers on a substrate, the wider the bandwidth of the spectral reflectance. For this reason, a multilayer coating can also be called a broadband coating.

A multilayer coating also has several methods to be designed. For example, all layer thicknesses being multiples of $\lambda/4$, all of them with unequal and non-multiple of $\lambda/4$, or a combination of them. Besides, all of them use at least two different refractive indices. For this work, we used the technique devised by Thetford (1968), where alternation of high- and low-index, unequal and non-multiple thicknesses, and only two values of refractive index are used instead of three. This method is cheaper in some way because you only need to buy two materials instead of three. In addition, this procedure is easier to understand; it consists of splitting a two-layer coating (which has a high-index layer next to the substrate) into four or five parts, according to the case. Because the expressions would be much more complicated in this case, Thetford did not attempt an analytical solution but rather arrived at a design by trial and error. Given the nature of the procedure, when departing from an existing design (two-layer, in this case), it is easier to use a trial and error solution based on the changes in the shape of the simulated admittance diagram than try an analytical solution. The design fabricated in Corning Reynosa for this thesis is presented in Figure 44. It is a broadband coating designed for the range from 1200 to 1600 nm, encompassing the two primary fiber optical communications lines: 1.31 and 1.55 µm. Also, a five-layer AR design simulated, but no fabricated is shown in figure 45.

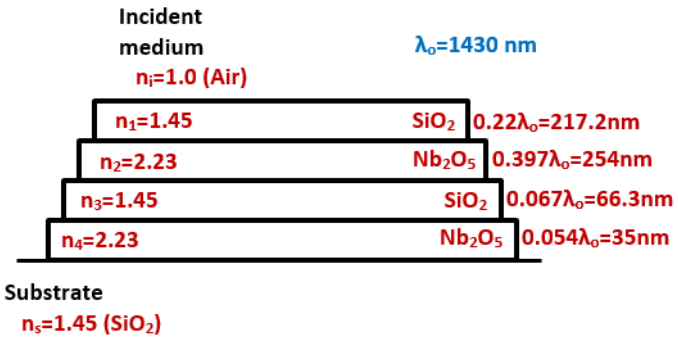

Figure 44 Four-layer broadband AR design fabricated for this thesis, based on the design proposed by Thetford (1968) and presented in (MacLeod, 2001).

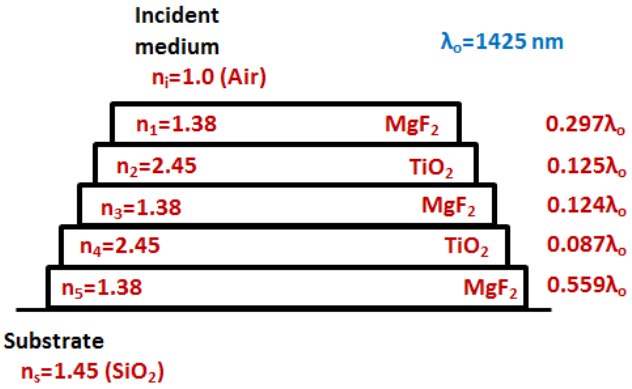

Figure 45 Five-layer broadband AR design simulated for this thesis, based on suggestions presented in (MacLeod, 2001). It was also aimed to covers the range from 1200 to 1600nm.

4.2 Simulations

As it has been mentioned before, antireflective designs from 1 to 5 layers were calculated and simulated. In this section, the simulation results for the AR coatings designs from single- to five-layer will be presented.

For all the simulations, an open-source software called *OpenFilters* (Figure 46) created by Larouche and Martinu (2008) from the Montreal Polytechnique School was used.

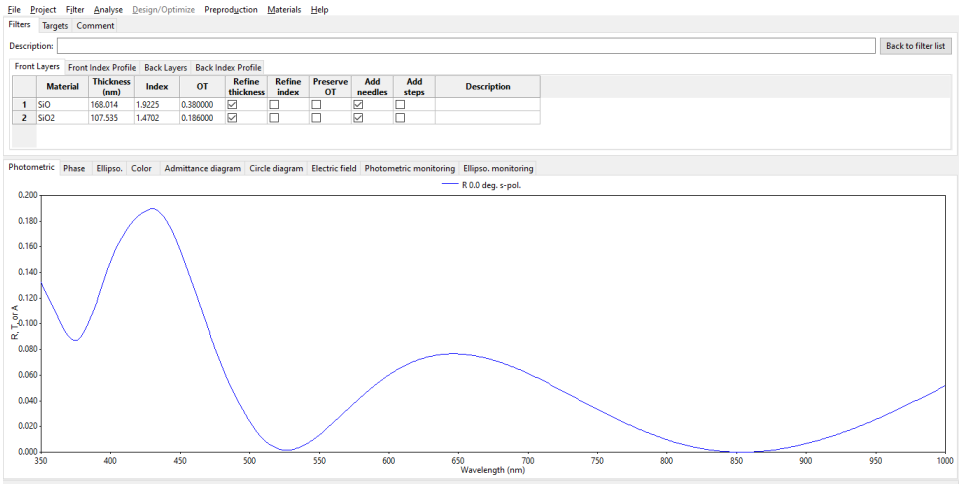

Figure 46 Screenshot of the OpenFilters interface (left), OpenFilters logo (right).

The simulation results of the AR designs are presented below. For each design, the following features will be shown.

- Design: materials, refractive indices, optical and physical thicknesses, centering wavelength.
- Spectral reflectance: only one face of the substrate is considered for the results presented in this section.
- Reflectivity percentage values for the interest wavelengths or ranges.
- Admittance diagram simulated by OpenFilters. The real and imaginary axles shown resulted from the characteristic matrix of the corresponding assembly.

The admittance diagram plot of a layer is a circle or a section of it. It depends on the thickness of the layer. If the thickness of the coating is $\lambda/4$, the chart will be a semicircle; if the thickness is $\lambda/2$, the chart will be a full circle. Thus, any value non-multiple of $\lambda/4$ will be a fraction of a circle on the diagram. As said before, the closest the admittance plot ends from the admittance of the incident media, the better the design performance.

4.2.1 Single-layer

The best approach's simulation result using the SiO_x modulation for a single-layer AR coating is presented in Figure 47. Recalling Equation 80, $n_1 = \sqrt{n_0 n_s}$, the refractive index of the layer has to be lower than the substrate's to achieve an AR effect. Given that the lowest refractive index obtained by the SiO_x modulation is higher than the substrate's, performance is poor. We can see that on the spectral reflectance graph.

As explained before, given that the layer is a $\lambda/4$, the shape of the admittance diagram is a semicircle. Also, it can be seen that the end of the semicircle is approximately at the point (1.482, 0). It is quite far from the admittance of the incident media (1, 0), which is the air. This also is translated as poor performance of the coating.

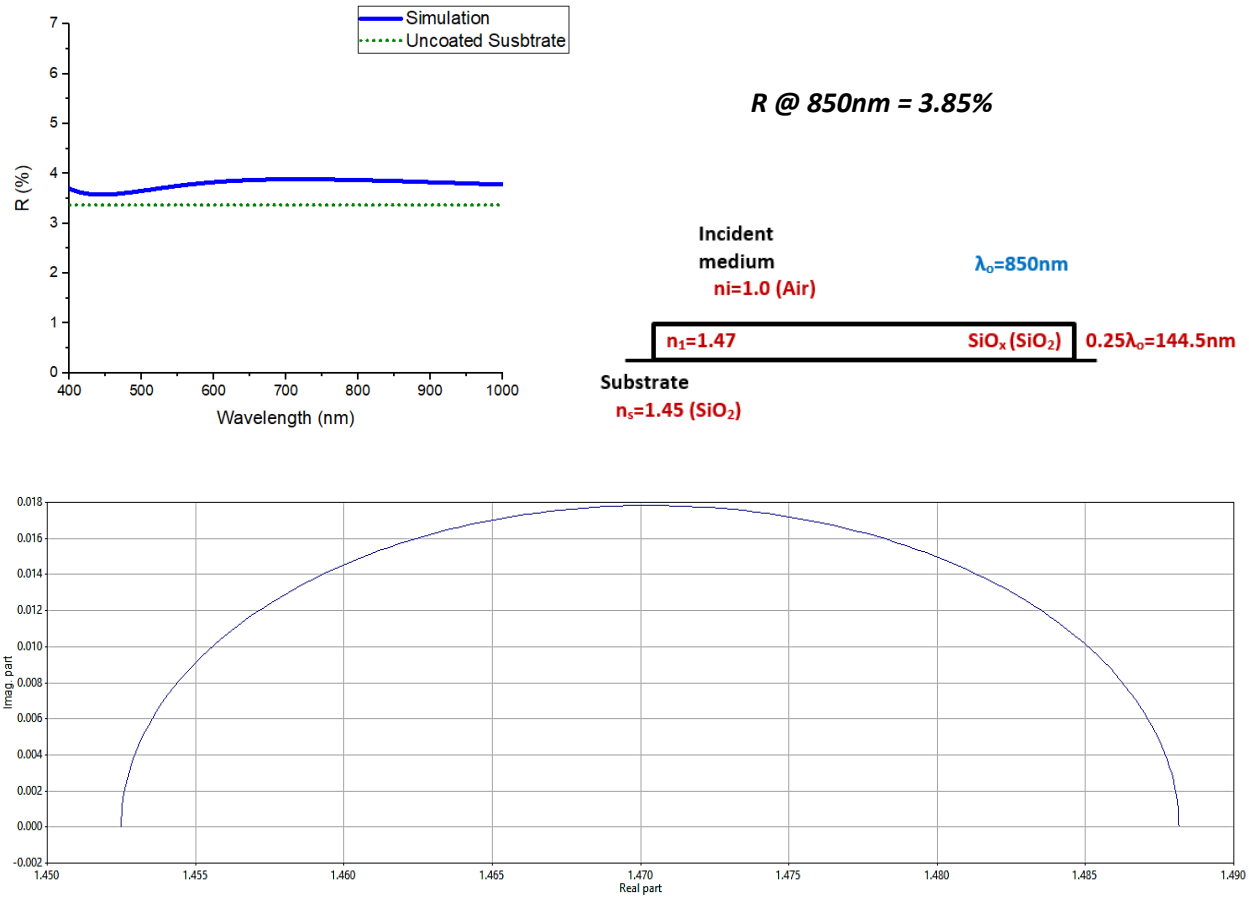

Figure 47 Simulation results of single-layer AR design with silica (SiO_2) centered at 850nm. It is presented spectral reflectance (top-left), design and reflectivity value at the reference wavelength (top-right), and admittance diagram (bottom).

4.2.2 Double-layer

As we have seen before, two different double-layer AR designs were simulated and fabricated in CICESE. Figures 48 and 49 present the simulation results.

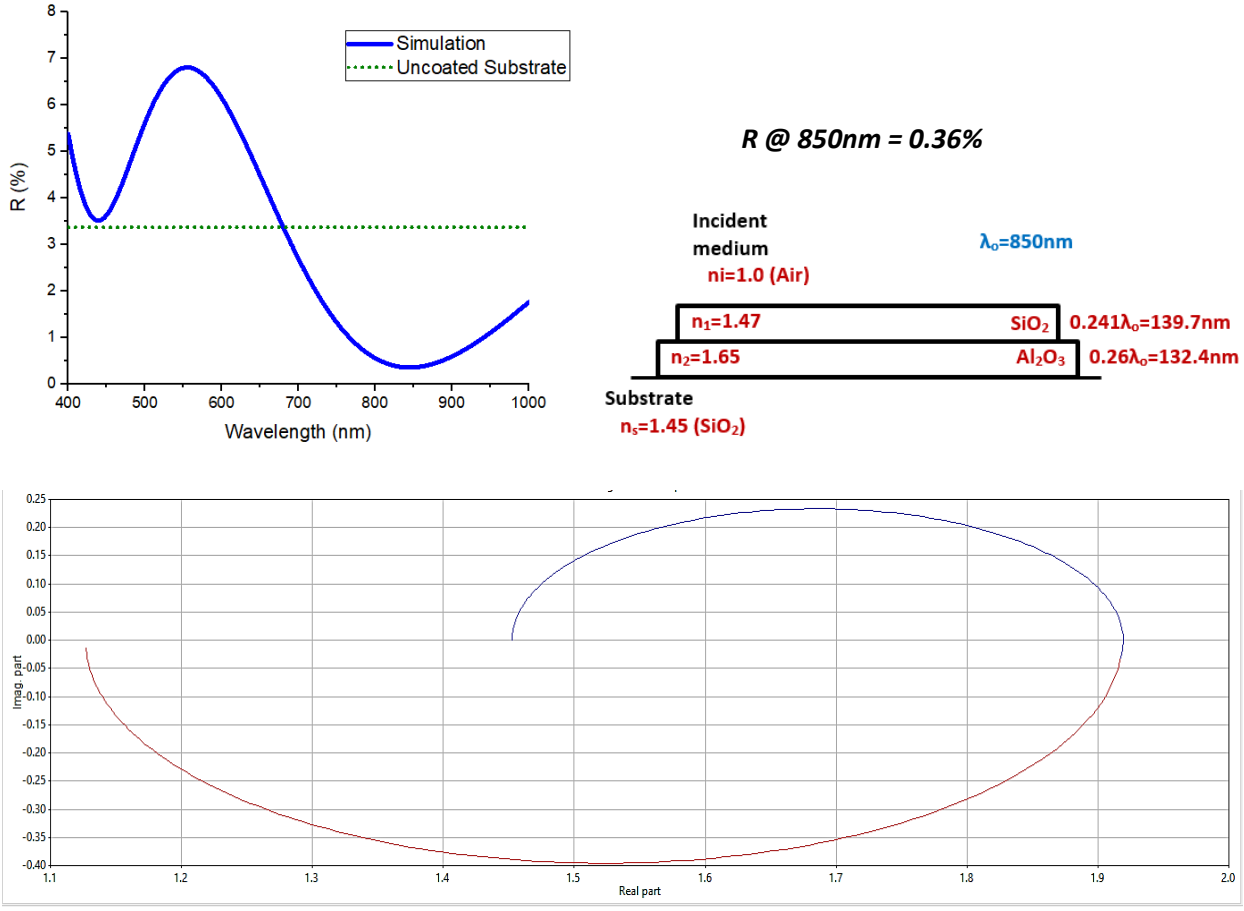

Figure 48 Simulation results of double-layer AR design with alumina (Al_2O_3) and silica (SiO_2) centered at 850nm.

Figure 48 shows an AR effect, especially on the reference wavelength (850nm). Given that the layers are non-multiple of $\lambda/4$, their admittance plots are fractions of circles. However, the outermost layer's admittance ends at the point (1.13, 0), which is close to the incident media admittance (1, 0). For this reason, this design has a good theoretical AR performance.

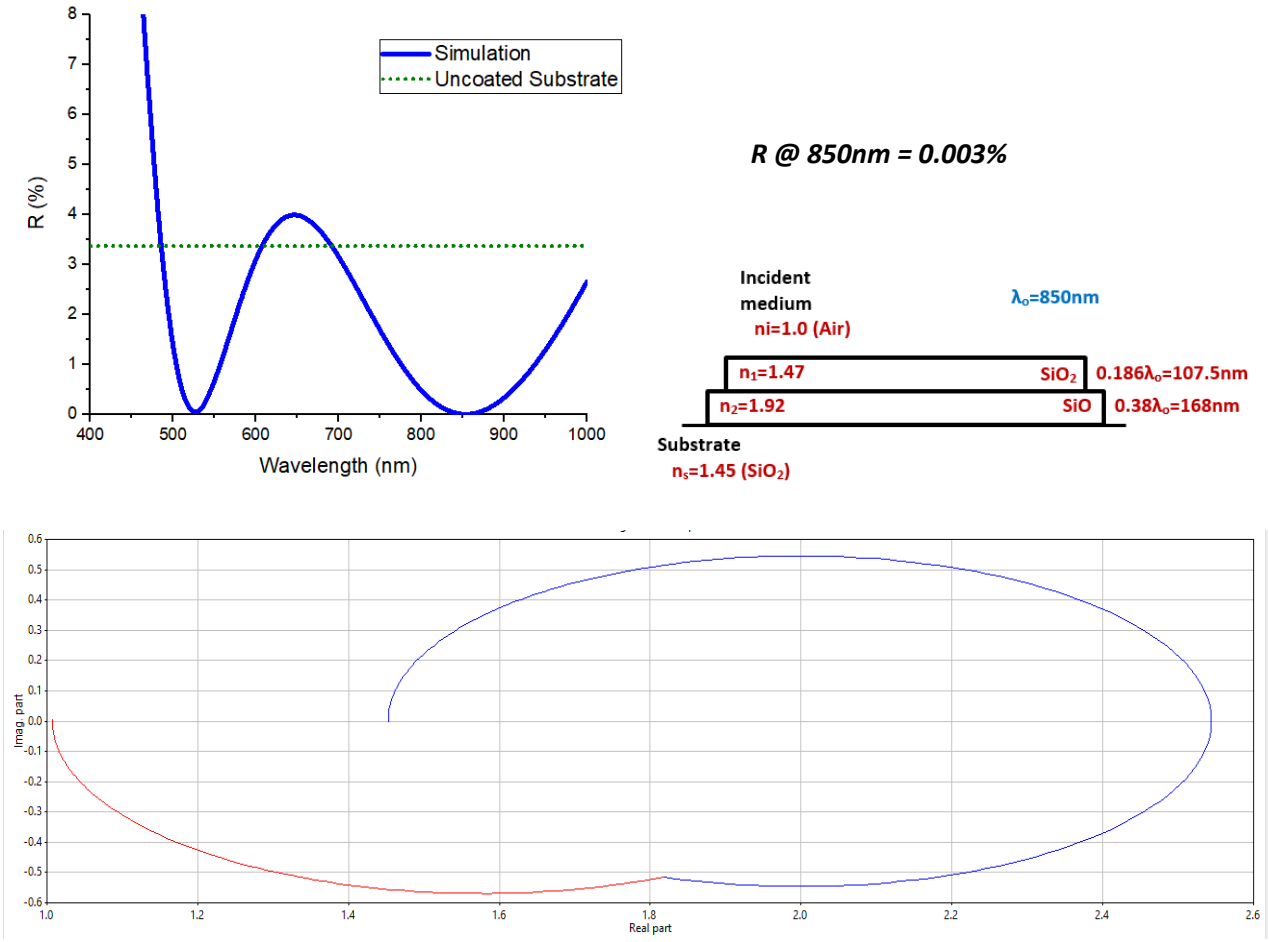

Figure 49 Simulation results of double-layer AR design with silicon monoxide (SiO) and silica (SiO_2) centered at 850nm.

Figure 49 also shows a good AR effect on the reference wavelength (850nm). As well as the previous design, given that the layers are non-multiple of $\lambda/4$, their admittance plots are fractions of circles. The admittance of the outermost layer ends extremely close to the air's admittance value, approximately at (1.01, 0). For this reason, this design has an excellent theoretical AR performance.

We can also see from Figures 48 and 49 at the central wavelength, 850nm, the characteristic V-like shape of the spectral reflectance. For this reason, the double-layer AR coatings are also called “V-Type.”

4.2.3 Triple-layer

Also, one triple-layer AR design with the QHQ configuration was simulated and fabricated in CICESE. It is shown in Figure 50.

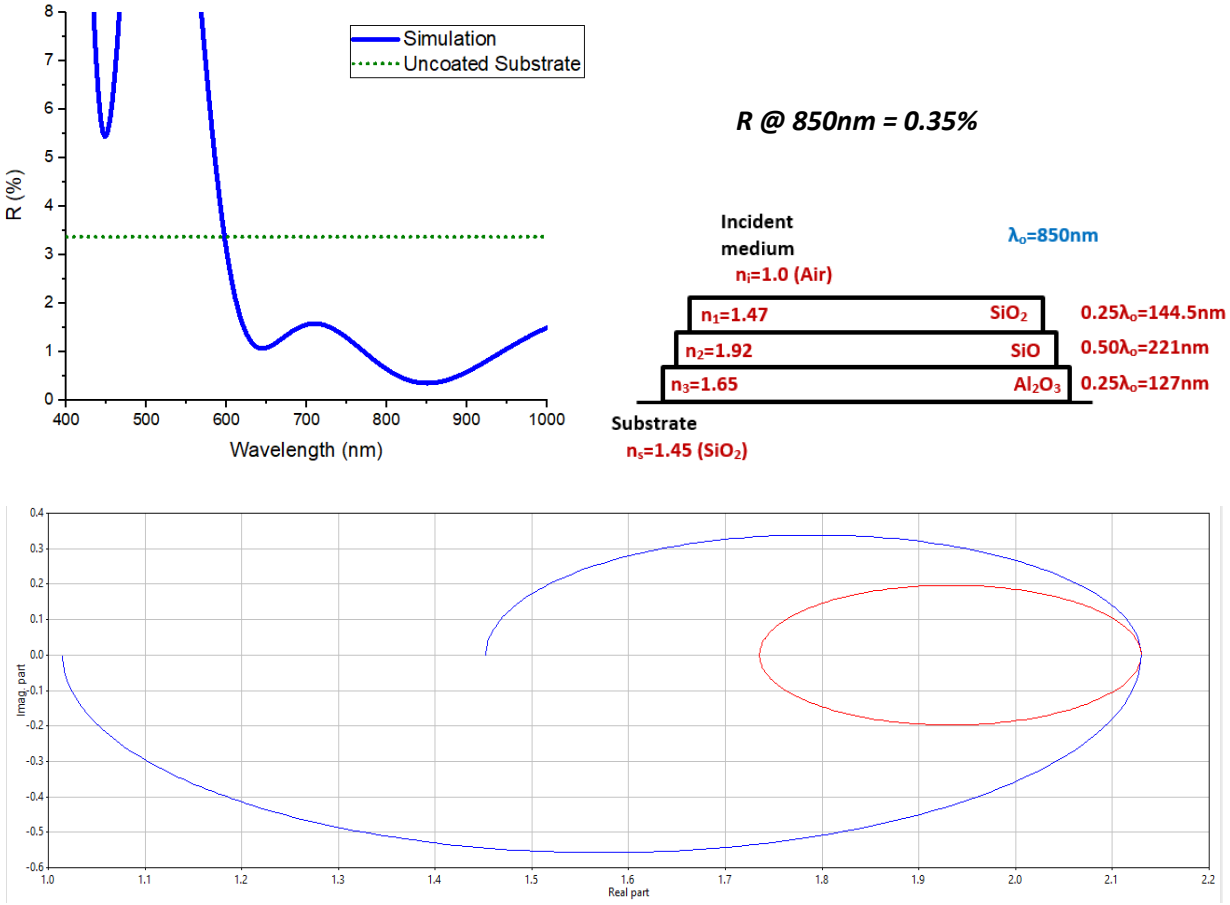

Figure 50 Simulation results of quarter-half-quarter AR design with alumina (Al_2O_3), silicon monoxide (SiO), and silica (SiO_2) centered at 850nm. It is presented spectral reflectance (top-left), design and reflectivity value at the reference wavelength (top-right), and admittance diagram (bottom).

The spectral reflectances shown until now are on the same vertical scale. If we compare Figures 48 or 49 with Figure 50, it is possible to see that the bandwidth is more prominent on the last graph. That corroborates the fact that the more layers on a substrate, the wider the bandwidth. Besides, the contrast between the highest and the lowest refractive index is important for the bandwidth; the greater the difference, the flatter the chart's shape. For this design, the limit is established by the maximum and minimum modulation of SiO_x refractive index, 1.92 and 1.47.

Given that the layers are multiple of $\lambda/4$, their admittance plots are fractions of circles. The last admittance plot ends very close to the air's admittance value, approximately at (1.03, 0). For this reason, this design has a good theoretical AR performance. However, as said earlier, designs with unequal thicknesses can achieve better results than a QHQ.

4.2.4 Four-layer

As discussed before, one four-layer AR design was simulated and fabricated in Corning Reynosa facilities. This is considered a broadband AR coating because of the number of layers. It was designed to cover the two main fiber optical communication lines (1310 and 1550nm) within the range from 1200 to 1600nm. The results of its simulation are shown in Figure 51.

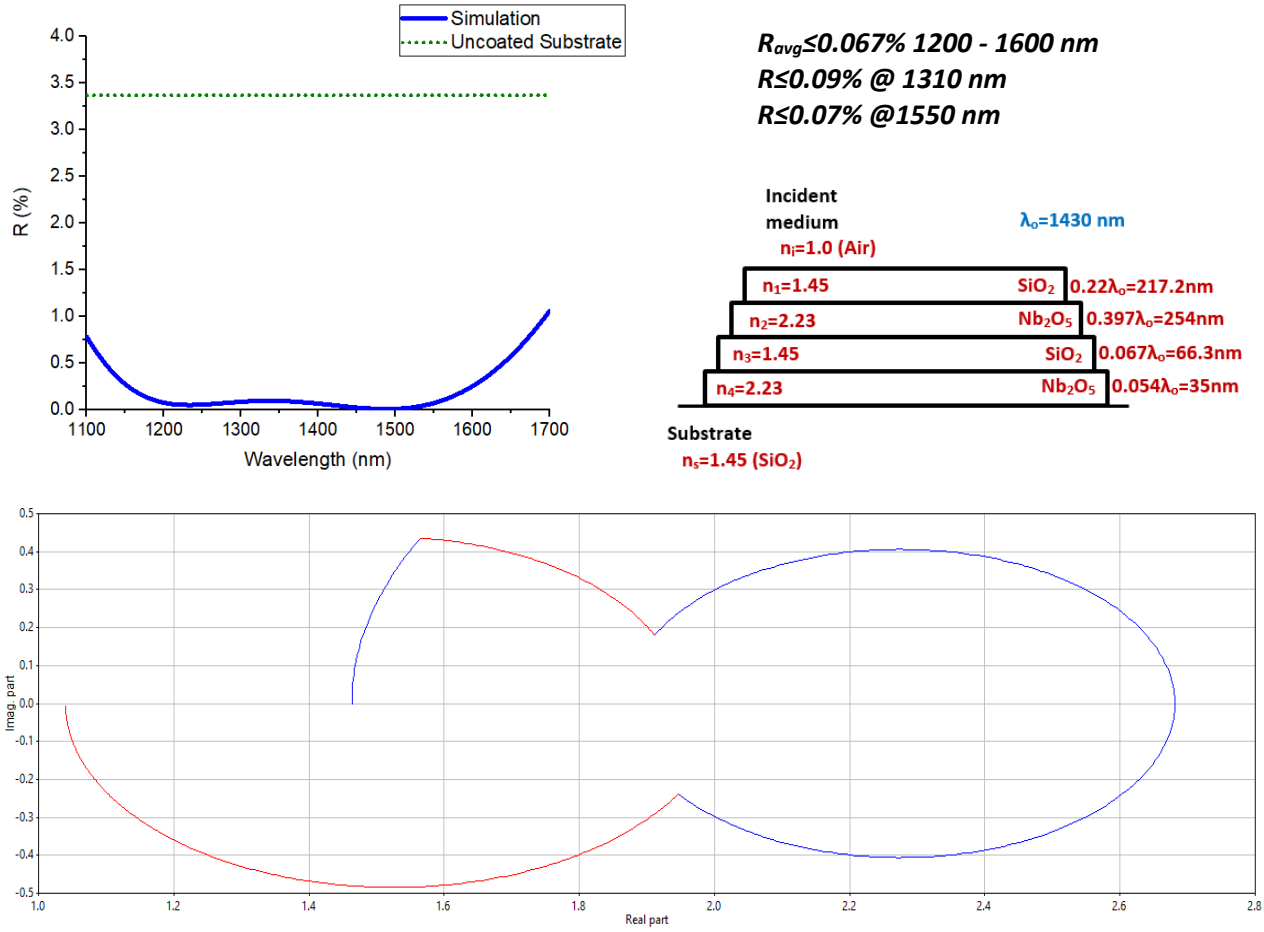

Figure 51 Simulation results of four-layer AR design with niobia (Nb_2O_5) and silica (SiO_2) centered at 1430nm, which is just the middle between 1310 and 1550nm. It is presented spectral reflectance (top-left), design and reflectivity values (top-right), and admittance diagram (bottom).

It is evident from Figure 51 that the bandwidth of the four-layer AR coating has become wider than the previous figures (Figures 48, 49, and 50), which are made of two or three layers, respectively. Also, the reflectivity values are quite low at the lines of interest, 1310 and 1550nm, which was an outstanding result for this thesis's intentions. It is also demonstrated again that designs with unequal thicknesses and higher contrast between the refractive indices tend to have better results. Those are the reasons this design has better performance than the QHQ design.

4.2.5 Five-layer

As previously said, also a five-layer AR design was simulated but no fabricated. Its simulation results are shown in Figure 52.

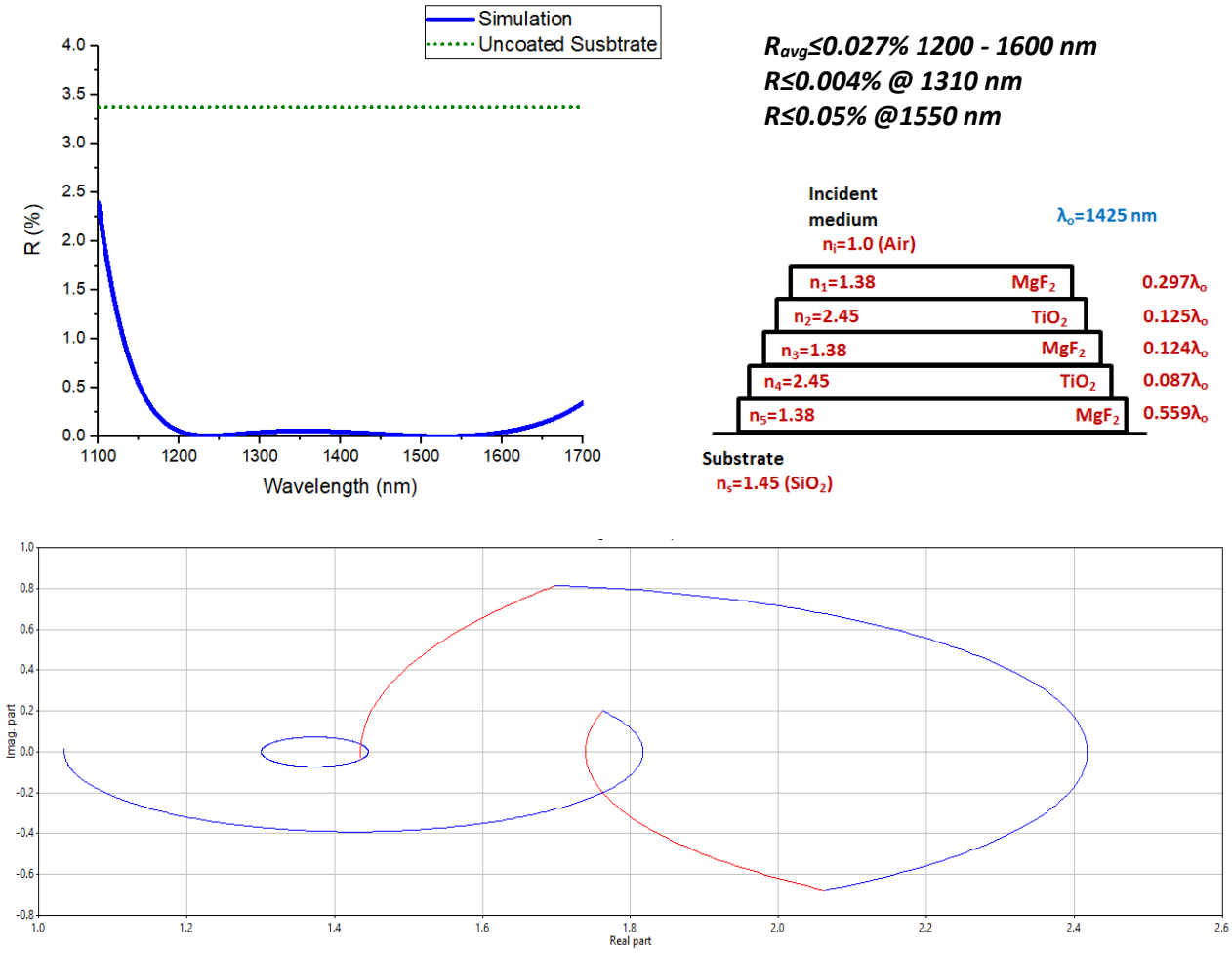

Figure 52 Simulation results of five-layer AR design with magnesium fluoride (MgF_2) and titania (TiO_2) centered at 1425nm, which is around the middle between 1310 and 1550nm. It is presented spectral reflectance (top-left), design and reflectivity values (top-right), and admittance diagram (bottom).

The five-layer result improved from the four-layer mainly because the contrast between the refractive index of the TiO_2 (n=2.45) and the MgF_2 (n=1.38) is higher than the Nb_2O_5 (n=2.23) and SiO_2 (n=1.45). We can also see that the admittance diagram are sections of circles because none of the layers are multiple of $\lambda/4$. Besides, the plot ends very close to the admittance of the air, approximately at (1.03, 0.02). Also, the reflectivity values are quite low at the lines of interest, 1310 and 1550nm, which was an excellent theoretical AR performance.

4.3 Synthesis

As we discussed in the previous section, this thesis's experimental work was divided into two parts, given the collaboration between CICESE's Optics Department and Corning, Inc. That means AR designs were produced at two different locations: CICESE and Corning Reynosa facilities. The details of the experiments at the two facilities are described below.

4.3.1 CICESE facilities

At the Thin-Films lab, were fabricated and characterized double- and triple-layer AR designs, the scope of this experimental setup was:

- Fabricate two double-layer AR designs.
- Fabricate one triple-layer (Quarter-Half-Quarter) AR design.
- Centered at 850nm, which is the third optical communications line.
- Usage of the reactive thermal evaporation technique.
- There were three different depositions for each design because the substrate received a different thermal treatment before the evaporation. When increasing the substrate's temperature, the mobility of the arriving molecules increases and can create denser films. The temperatures selected were room temperature, 100°C, and 200°C.
- Were obtained three different refractive indices similar to silica (SiO_2), alumina (Al_2O_3), and silicon monoxide (SiO) by evaporating only one material: SiO. This was possible using the SiO_x index modulation by manipulating the fabrication parameters (see Material and Methods section for more information). As a reminder,

  - To get silica is needed a low vacuum (≥**1.5x10^{-4} Torr**) and depositing at a low rate (**0.4 nm/s**).
  - The Al_2O_3-like refractive index is achieved by setting a low deposition rate (**0.4 nm/s**) and a high vacuum (≤ **1x10^{-6} Torr**).
  - The SiO-like refractive index is achieved by setting a high deposition rate (≥**2 nm/s**) and a high vacuum (≤ **1x10^{-6} Torr**).
- Deposition on both faces of the silica substrates.

The features of the fabricated AR samples on the first face of the substrate are shown in Table 4, and for the second face in Table 5. Besides, a photo of some of them is shown in Figure 53, which shows darker substrates than others. This is caused for the amount of silicon on the SiO_x resulting stoichiometry. Given that the silicon absorbs more in the visible, the more amount of silicon, the darker to the eye.

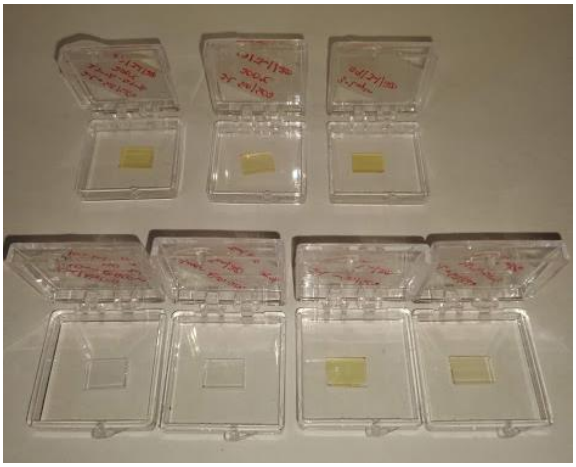

Figure 53 AR designs fabricated in CICESE using reactive thermal evaporation technique and modulation of SiO_x index to obtain three different refractive indexes similar to silica, alumina, and silicon monoxide.

Table 3 Results of synthesis of the three AR designs at their respective substrate thermal treatment before the evaporation; deposited on the first face of the silica substrates. All of the samples have a reference wavelength of 850nm.

	FIRST FACE OF THE SILICA SUBSTRATE						
	Coating Materials	Substrate treatment temperature (°C)	Deposition Pressure (Torr)	Deposition rate (nm/s)	Theoretical thickness		Thickness results (nm)
					Optical Thickness	Physical Thickness (nm)	Quartz Crystal Sensor
Double-layer	Al_2O_3 SiO_2	Room	***$1x10^{-6}$*** ***$1.5x10^{-4}$***	***0.4*** ***0.4***	0.26λo 0.241λo	132.4 139.7	132 139
		100	***$1.5x10^{-6}$*** ***$1.5x10^{-4}$***	***0.4*** ***0.4***	0.26λo 0.241λo	132.4 139.7	134 140
		200	***$1x10^{-6}$*** ***$1.5x10^{-4}$***	***0.4*** ***0.4***	0.26λo 0.241λo	132.4 139.7	134 140
Double-layer	SiO SiO_2	Room	***$1.12x10^{-6}$*** ***$1.5x10^{-4}$***	***2.5*** ***0.4***	0.38λo 0.186λo	168 107.5	171 107
		100	***$1x10^{-6}$*** ***$1.5x10^{-4}$***	***2.0*** ***0.4***	0.38λo 0.186λo	168 107.5	170 108
		200	***$1x10^{-6}$*** ***$1.5x10^{-4}$***	***2.2*** ***0.4***	0.38λo 0.186λo	168 107.5	170 108
Triple-layer	Al_2O_3 SiO SiO_2	Room	***$1.5x10^{-6}$*** ***$1.5x10^{-6}$*** ***$1.5x10^{-4}$***	***0.4*** ***2.1*** ***0.4***	0.25λo 0.50λo 0.25λo	127 221 144.5	126 222 148
		100	***$1x10^{-6}$*** ***$1x10^{-6}$*** ***$1.5x10^{-4}$***	***0.4*** ***2.5*** ***0.4***	0.25λo 0.50λo 0.25λo	127 221 144.5	129 223 145
		200	***$1.5x10^{-6}$*** ***$1x10^{-6}$*** ***$1.5x10^{-4}$***	***0.4*** ***1.9*** ***0.4***	0.25λo 0.50λo 0.25λo	127 221 144.5	128 227 146

Table 4 Results of synthesis of the three AR designs at their respective substrate thermal treatment before the evaporation; deposited on the second face of the silica substrates. All of the samples have a reference wavelength of 850nm.

	SECOND FACE OF THE SILICA SUBSTRATE						
	Coating Materials	Substrate treatment temperature (°C)	Deposition Pressure (Torr)	Deposition rate (nm/s)	Theoretical thickness		Thickness results (nm)
					Optical Thickness	Physical Thickness (nm)	Quartz Crystal Sensor
Double-layer	Al_2O_3 SiO_2	Room	***1x10^{-6}***	***0.4***	0.26λo	132.4	134
			1.5x10^{-4}	***0.4***	0.241λo	139.7	139
		100	***1x10^{-6}***	***0.5***	0.26λo	132.4	134
			1.5x10^{-4}	***0.4***	0.241λo	139.7	140
		200	***1x10^{-6}***	***0.4***	0.26λo	132.4	133
			1.5x10^{-4}	***0.4***	0.241λo	139.7	139
Double-layer	SiO SiO_2	Room	***1.1x10^{-6}***	***2.0***	0.38λo	168	168
			1.5x10^{-4}	***0.45***	0.186λo	107.5	109
		100	***1x10^{-6}***	***1.9***	0.38λo	168	169
			1.5x10^{-4}	***0.4***	0.186λo	107.5	109
		200	***1.5x10^{-6}***	***2.2***	0.38λo	168	170
			1.5x10^{-4}	***0.4***	0.186λo	107.5	109
Triple-layer	Al_2O_3 SiO SiO_2	Room	***1x10^{-6}***	***0.5***	0.25λo	127	129
			1x10^{-6}	***1.9***	0.50λo	221	225
			1.5x10^{-4}	***0.4***	0.25λo	144.5	146
		100	***1x10^{-6}***	***0.4***	0.25λo	127	130
			1x10^{-6}	***1.8***	0.50λo	221	223
			1.5x10^{-4}	***0.4***	0.25λo	144.5	147
		200	***1.5x10^{-6}***	***0.4***	0.25λo	127	129
			1.1x10^{-6}	***2.0***	0.50λo	221	222
			1.5x10^{-4}	***0.4***	0.25λo	144.5	144

Table 4 and 5 show the depositions features on the first and the second substrate face, respectively. We can see that both pressure values and measured thicknesses are similar to the ideal ones, recalling that the target values were **1x10^{-6}** and **1.5x10^{-4} Torr** for high-vacuum and low-vacuum levels, respectively. On the other hand, the high deposition rate (to get SiO-like refractive index) has some fluctuations from the ideal value of **2.0 nm/s.** The faster the deposition rate required, the more current needed to be passed through the boat to evaporate the material. The amount of current necessary to obtain SiO-like was very close to the evaporation machine's limitations, so there were instabilities in the total current provided by the machine. That was traduced as slight fluctuations in the high valued deposition rates. However, it did not considerably affect the resulting refractive index.

4.3.2 Corning Reynosa facilities

The other part of this thesis's experiments was made in the Corning facilities at Reynosa, México. At the Thin-Films lab, was fabricated and characterized a four-layer AR design; the scope of this experimental setup was:

- Fabricate one four-layer AR design.
- Ion Beam Assisted Deposition (IBAD) technique was used for deposition.
- Broadband antireflective (BBAR) design for the range from 1200 to 1600nm.
- Design centered at 1430nm.
- The characterization was made using the spectrophotometer Filmetrics F-10 AR to obtain the deposits' spectral reflectance within the range from 380 to 1700nm.

The characteristics of the fabricated AR samples in Reynosa are shown in Table 6. Besides, a picture of them is shown in Figure 54.

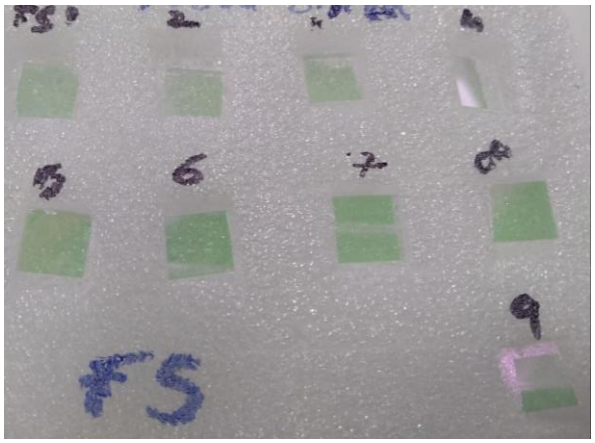

Figure 54 Broadband AR designs fabricated in Corning Reynosa using IBAD technique.

Table 5 Results of synthesis of the four-layer broadband AR design. All of the samples have a reference wavelength of 1430nm.

	Coating Materials	Deposition temperature (°C)	Deposition Pressure (Torr)	Ar flux (sccm)	O_2 flux (sccm)	Theoretical thickness		Thickness results (nm)
						Optical Thickness	Physical Thickness (nm)	
Four-layer	Nb_2O_5 SiO_2 Nb_2O_5 SiO_2	< 110	***1.5x10^{-4}***	15	20	0.054λo 0.067λo 0.397λo 0.22λo	35 66.3 254 217.2	35 66.3 254 217.2

4.4 Optical Characterization

4.4.1 Spectroscopic Ellipsometry (SE)

The ellipsometer J. A. Woollam M2000D placed in the UABC campus Mexicali was used to characterize the refractive index of the deposited films by the SiO_x modulation. Figure 55 shows a photo of the used equipment and the experimental arrangement for the measurements.

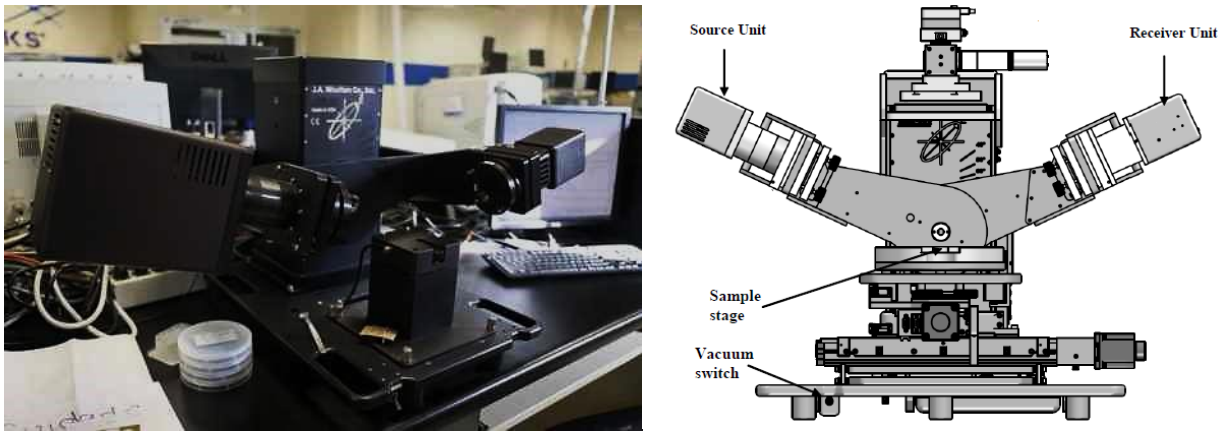

Figure 55 Ellipsometer J. A. Woollam M2000D located in the UABC campus Mexicali (left) and arrangement to perform the measurements (right).

As we have seen from the simulation results, there were three different refractive indices for the fabrication of AR designs in CICESE: silica, alumina, and silicon monoxide. All of them were obtained by the modulation of the SiO_x refractive index. Figure 56 and Figure 57 show their ellipsometric characterization curve and their comparison with the theory. Notice that the alumina-like refractive index is missing; because of the coronavirus pandemic, it was impossible to access to the ellipsometer one more time.

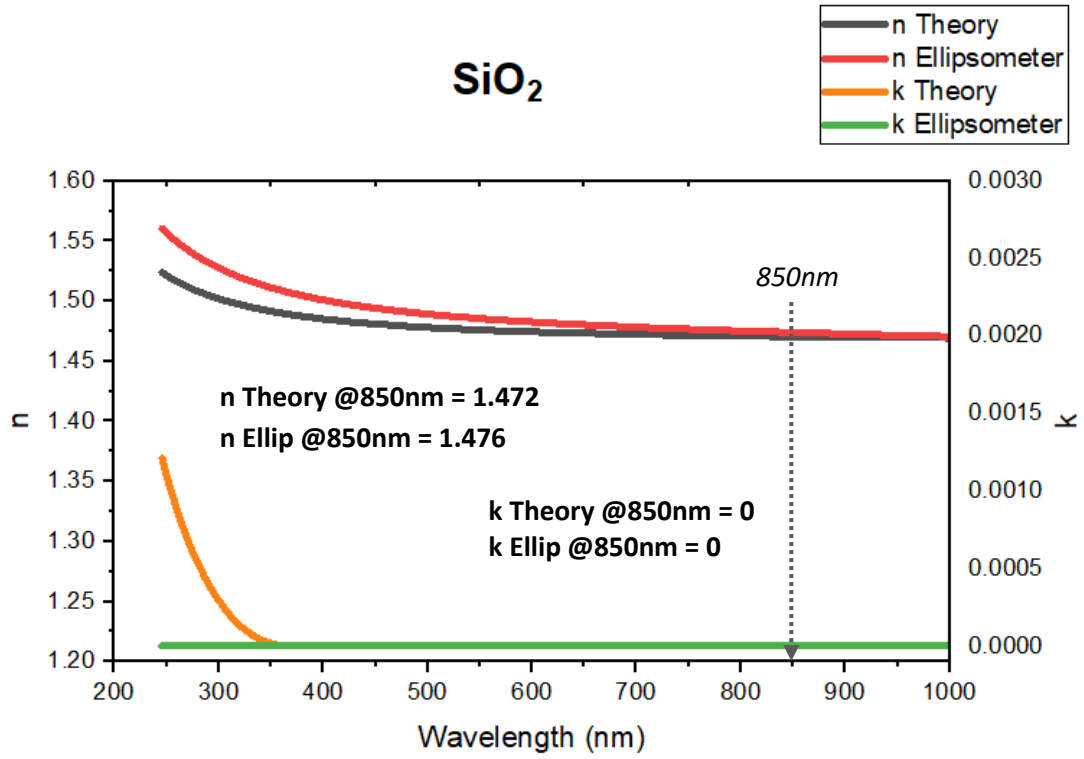

Figure 56 Comparative of ellipsometer results vs. theory for silica-like refractive index obtained by the SiOx index modulation at CICESE facilities. Theoretical data obtained from Gao et al. (2013).

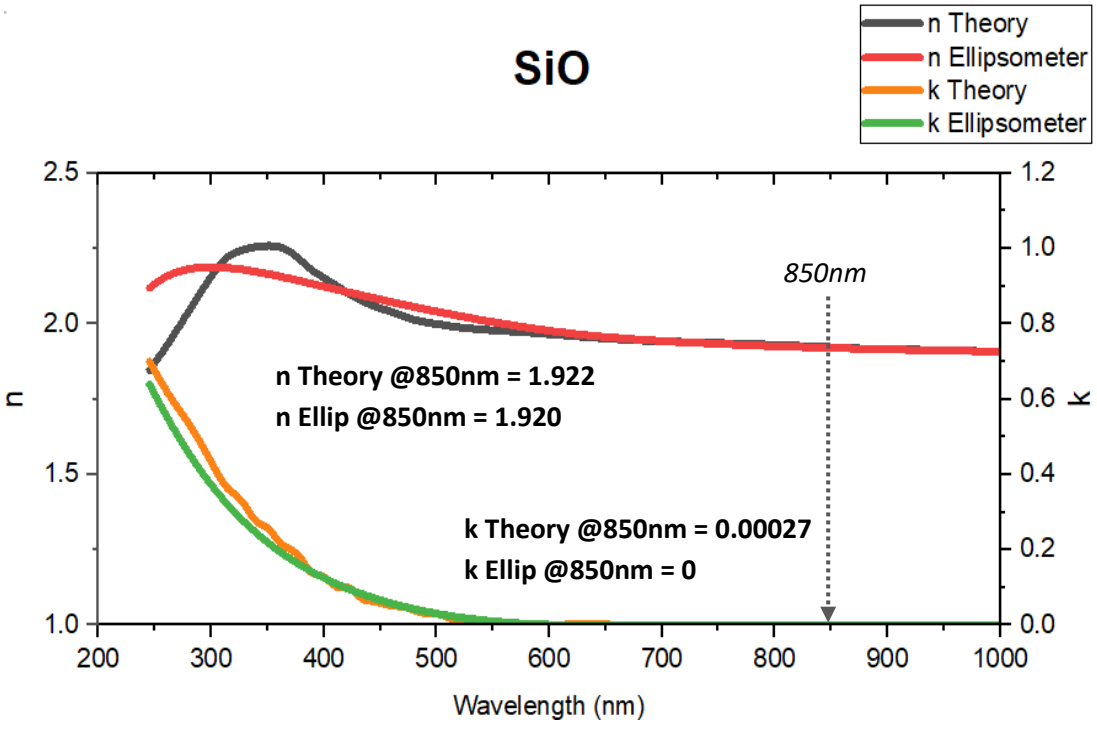

Figure 57 Comparative of ellipsometer results vs. theory for silicon monoxide-like refractive index obtained by the SiO_x index modulation at CICESE facilities. Theoretical data obtained from Hass and Salzberg (1954).

Figures 56 and 57 show the comparison theory versus experiment of refractive index (n) and the extinction coefficient (k), which is related to material absorption. We can see that, at the reference wavelength, the values of n and k are very similar theoretical and experimentally for both SiO_2 and SiO. This ellipsometric study proves that we are getting the desired refractive indices using the modulation of the SiO_x.

4.4.2 Spectrophotometry

4.4.2.1 CICESE facilities

Figure 58 shows the experimental block diagram and a photo of the arrangement used to measure the optical transmittance of double- and triple-layer AR designs deposited at CICESE. Were used a spectrometer OceanOptics Red Tide USB650 and a tungsten-halogen light source to characterize the wavelength from 350 to 1000nm.

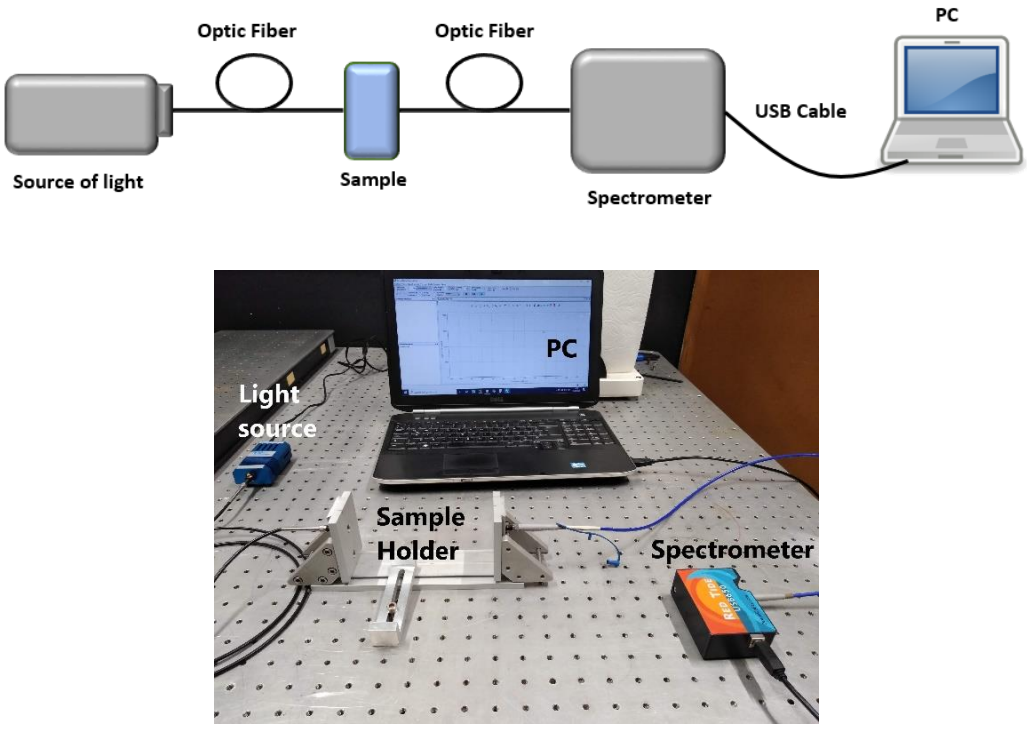

Figure 58 Transmittance characterization experimental block diagram (up) and a photo of the arrangement (bottom).

Figure 59 to 70 will present the results of transmittance and reflectance characterization for the three designs (two double-layer and one triple-layer) for each substrate temperature deposited on the first face of the substrate. For the transmittance graph, the red line is the theoretical result obtained from the simulations, the short-dot and short-dash lines mean the +/- 10% of the thickness of the layers to see how far or how close we are from the ideal theoretical value, the green line is the uncoated-substrate experimental transmittance. The blue line is the experimental data measured from the deposited design. It is also presented an inset graph that shows a zoom of the area of interest (850nm). In addition, a comparative-temperature graph for each design is given (Figures 62, 66, and 70). On the other hand, for the reflectance graph, the yellow line is the theoretical simulated value, the green line the experimental data, and the purple line is the uncoated-substrate reflectance.

4.4.2.1.1 Al_2O_3-SiO_2 double-layer AR coating (first substrate face)

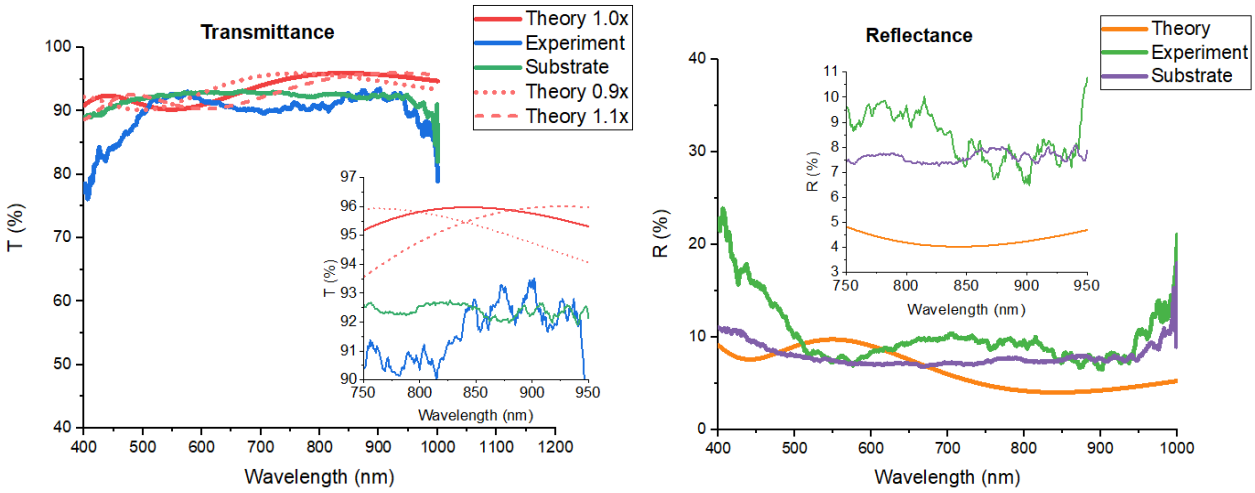

Figure 59 Transmittance and reflectance of Al_2O_3-SiO_2 double-layer AR coating at room temperature deposited on one face of the silica substrate.

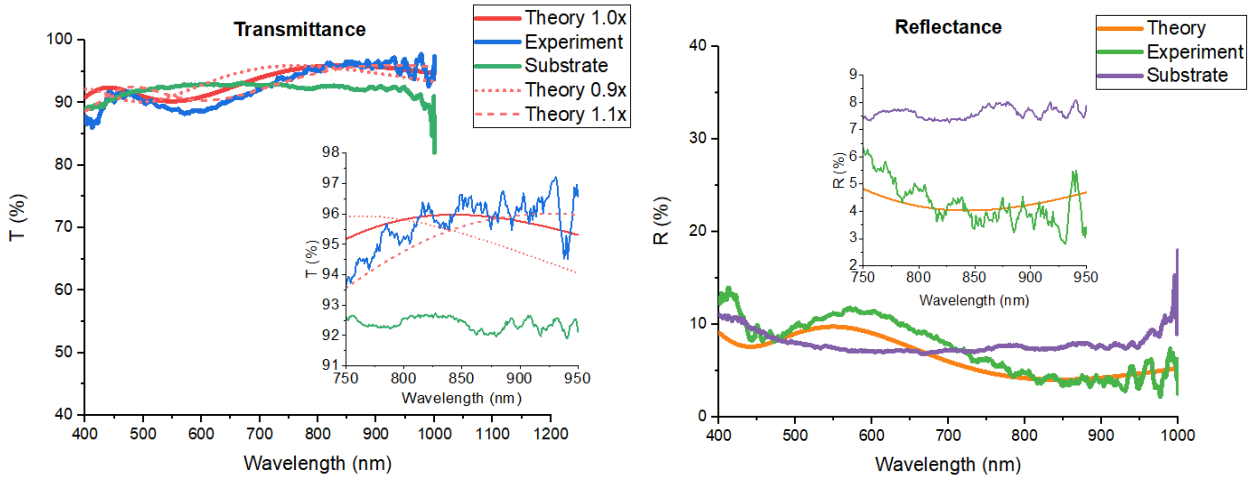

Figure 60 Transmittance and reflectance of Al_2O_3-SiO_2 double-layer AR coating at 100°C deposited on one face of the silica substrate.

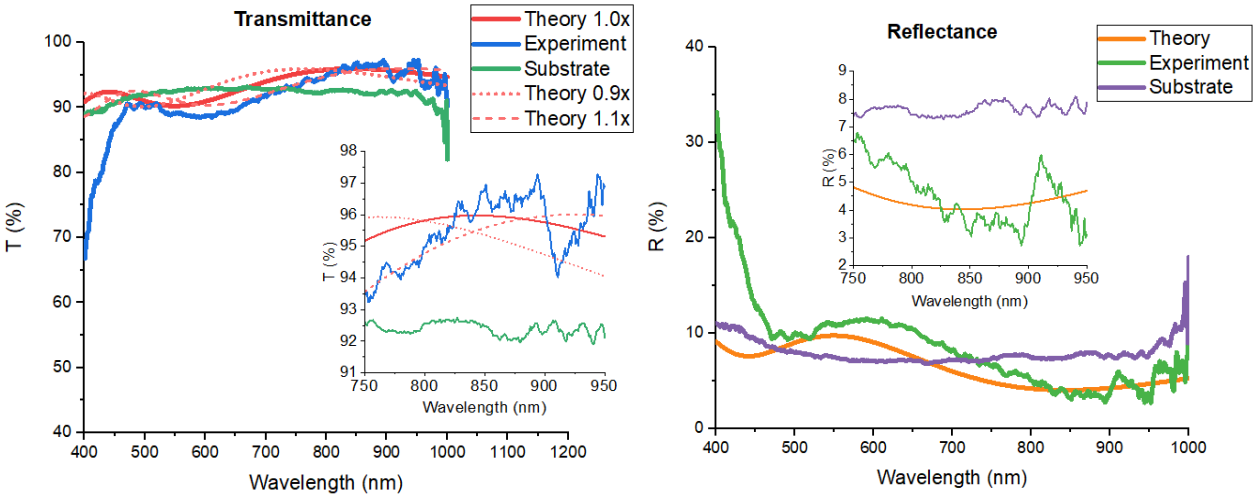

Figure 61 Transmittance and reflectance of Al_2O_3-SiO_2 double-layer AR coating at 200°C deposited on one face of the silica substrate.

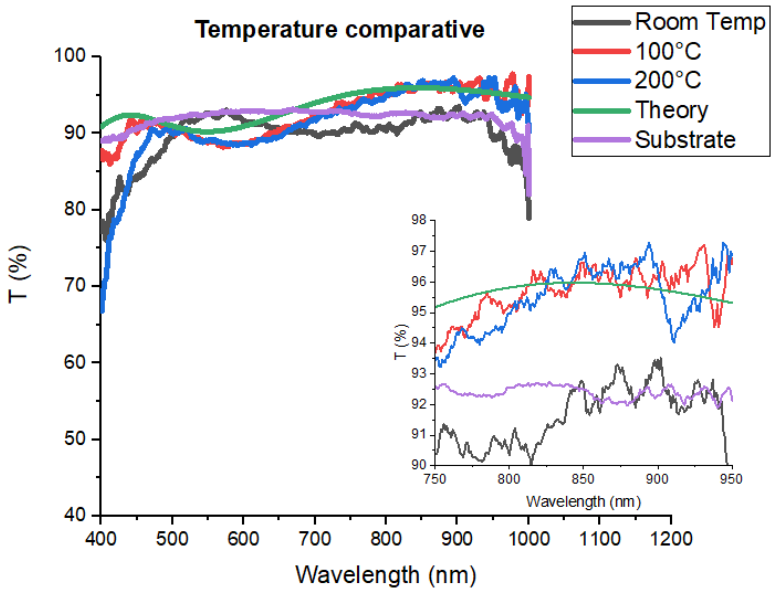

Figure 62 Temperature-comparative transmittance graph of Al_2O_3-SiO_2 double-layer AR coating.

Table 6 Comparison of values of transmittance of the Al_2O_3-SiO_2 double-layer AR coating at the reference wavelength for each substrate temperature.

SUBSTRATE FIRST FACE							
Design	**%T @ 850nm**						
	Theory	**Theory +10% Thickness**	**Theory -10% Thickness**	**Room Temperature**	**100°C**	**200°C**	**Uncoated Substrate**
2-Layer AR coating (Al_2O_3-SiO_2)	95.96	95.58	95.35	92.6	96.6	96.8	92.46

From these results, it is evident how the transmittance improved when you increase the temperature from room to 100°C. This could be caused by the increase in the evaporated atoms' mobility because of the thermal energy. This phenomenon can cause a better arrangement of the impregnated molecules on the substrate; thus, a denser film is grown. However, there is no visible enhancement from the latter to the 200°C result; there is even a peak of decrement around 910nm. It could be caused due to the noise in the measurement because it is close to the maximum limit of the equipment (1000 nm) or because of the imperfections due to the columnar growth. Maybe it is required a higher value of temperature to see a substantial improvement. Temperatures of 300°C or more may result in transmittances more matched to the ideal one.

4.4.2.1.2 SiO-SiO_2 double-layer AR coating (first substrate face)

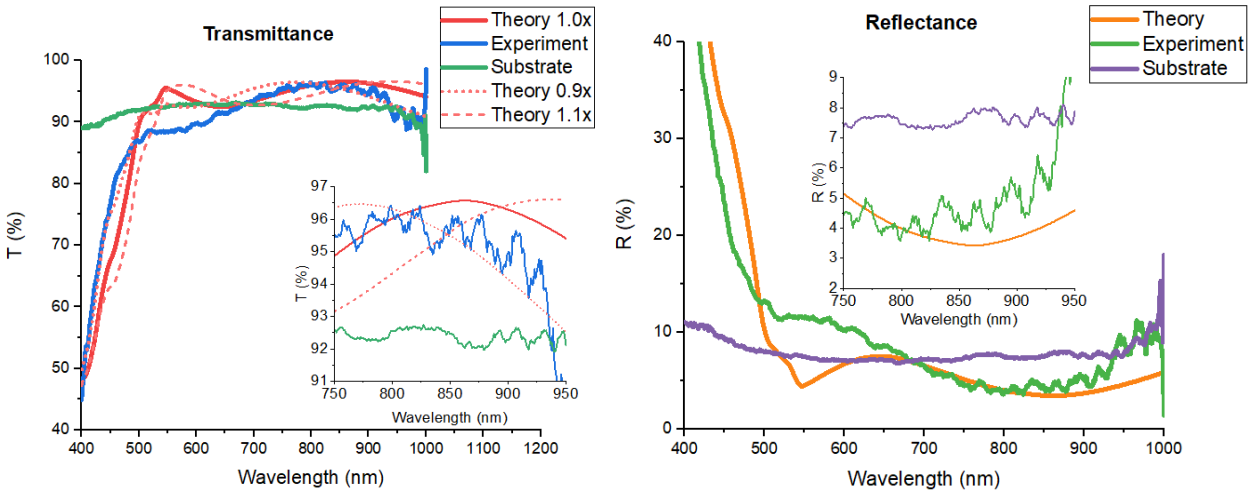

Figure 63 Transmittance and reflectance of SiO-SiO_2 double-layer AR coating at room temperature deposited on one face of the silica substrate.

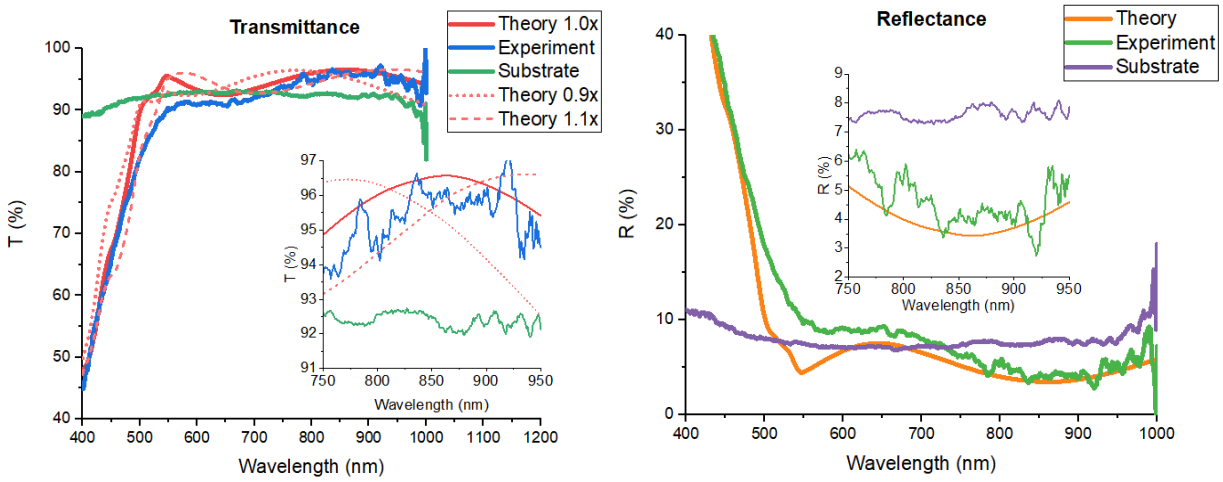

Figure 64 Transmittance and reflectance of SiO-SiO_2 double-layer AR coating at 100°C deposited on one face of the silica substrate.

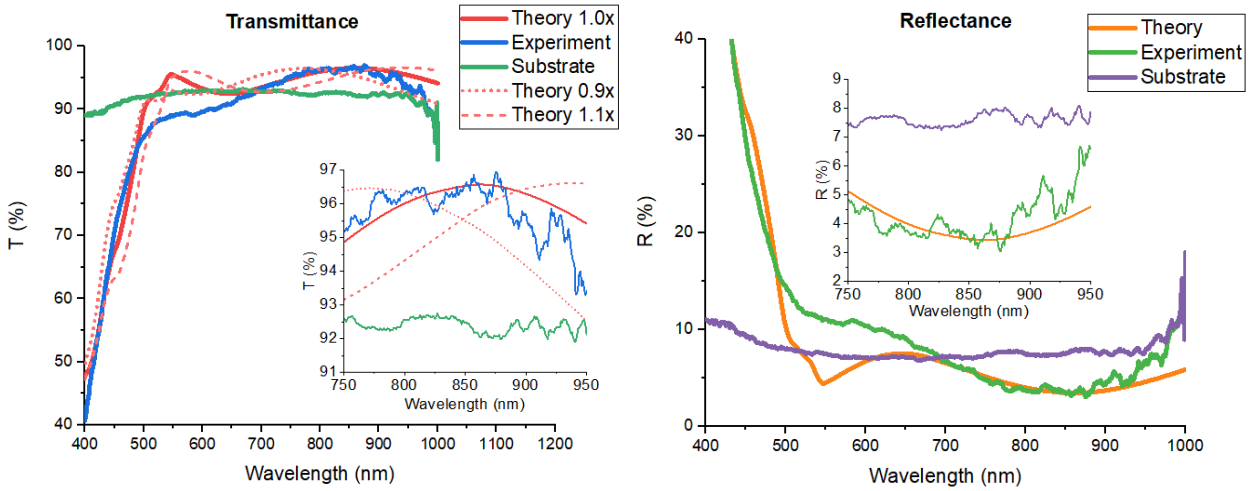

Figure 65 Transmittance and reflectance of SiO-SiO_2 double-layer AR coating at 200°C deposited on one face of the silica substrate.

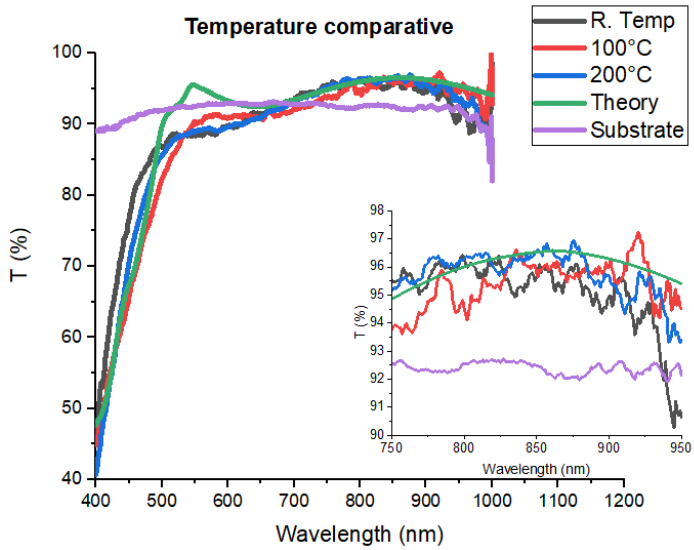

Figure 66 Temperature-comparative transmittance graph of SiO-SiO_2 double-layer AR coating.

Table 7 Comparison of values of transmittance of the SiO-SiO_2 double-layer AR coating at the reference wavelength for each substrate temperature.

SUBSTRATE FIRST FACE							
Design	**%T @ 850nm**						
	Theory	**Theory +10% Thickness**	**Theory -10% Thickness**	**Room Temperature**	**100°C**	**200°C**	**Uncoated Substrate**
2-Layer AR coating (SiO-SiO_2)	96.53	95.6	95.5	95.6	95.8	96.2	92.46

On this design, there was not a considerable transmittance improvement between temperatures. As the temperatures increase, the experimental lines would have to tend to be more fitted to the ideal one, but there was not an evident improvement in the values like on the previous design. The literature says that high deposition rates can improve the packaging density of the films deposited by thermal evaporation; this design requires high rates to obtain the SiO. That may be why the good results obtained, not being the temperature a fundamental key at this time; the previous design used both rates of *0.4 nm/s,* and this one a rate around *2.0 nm/s* for the SiO and *0.4nm/s* for SiO_2.

4.4.2.1.3 Al_2O_3-SiO-SiO_2 triple-layer AR coating (first substrate face)

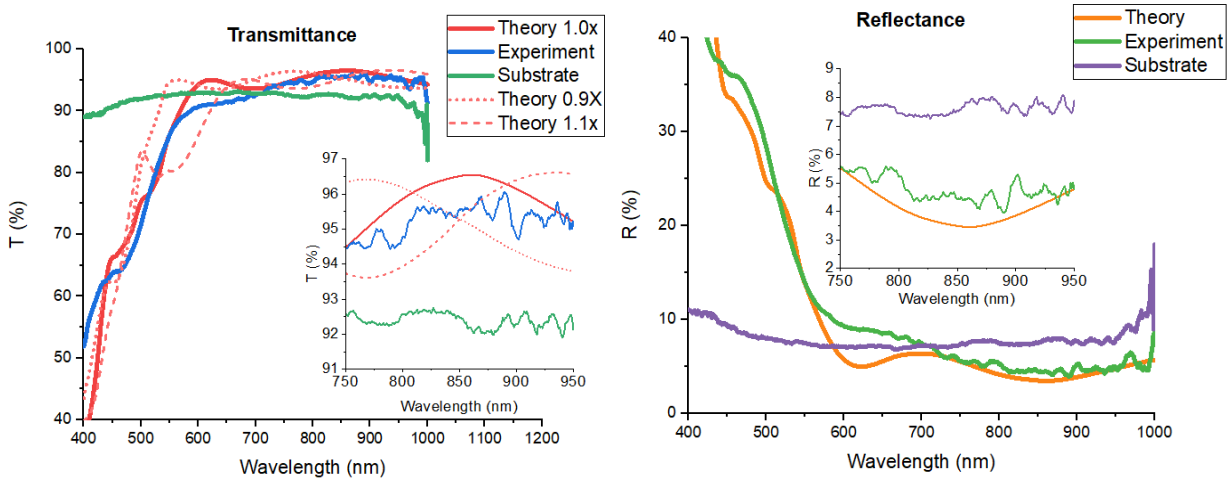

Figure 67 Transmittance and reflectance of Al_2O_3-SiO-SiO_2 triple-layer AR coating at room temperature, deposited on one face of the silica substrate.

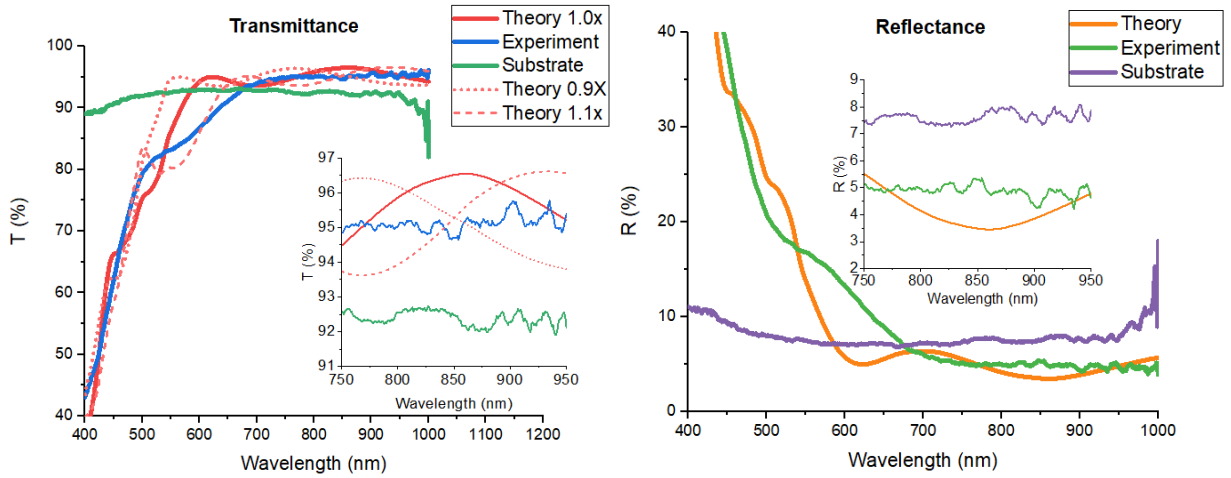

Figure 68 Transmittance and reflectance of Al_2O_3-SiO-SiO_2 triple-layer AR coating at 100°C, deposited on one face of the silica substrate.

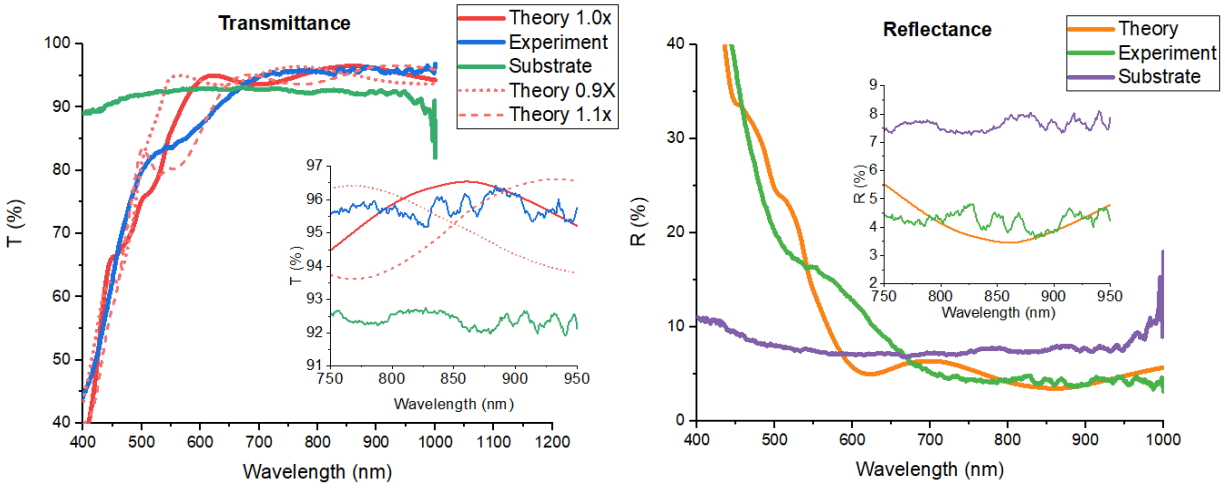

Figure 69 Transmittance and reflectance of Al_2O_3-SiO-SiO_2 triple-layer AR coating at 200°C, deposited on one face of the silica substrate.

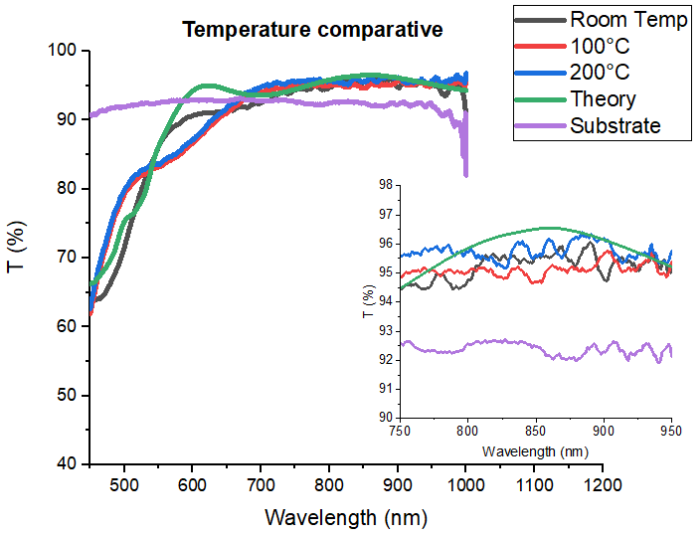

Figure 70 Temperature-comparative transmittance graph of Al_2O_3-SiO-SiO_2 triple-layer AR coating.

Table 8 Comparison of values of transmittance of the Al_2O_3-SiO-SiO_2 triple-layer AR coating at the reference wavelength for each substrate temperature.

SUBSTRATE FIRST FACE							
Design	**%T @ 850nm**						
	Theory	**Theory +10% Thickness**	**Theory -10% Thickness**	**Room Temperature**	**100°C**	**200°C**	**Uncoated Substrate**
3-Layer AR coating (Al_2O_3-SiO-SiO_2)	96.5	95.2	95.3	95.56	94.9	95.6	92.46

As well as the previous design, there was a similarity in the results for all the temperatures. The reason could be the same: high deposition rate (*2.0 nm/s*) used to get SiO overcomes the importance of temperature to get better transmittances, just as explained before.

On the other hand, from Figure 71 to 82 will be presented the results of transmittance characterization for all the same three AR designs for each substrate temperature deposited on the second face of the substrate. The color code is the same; for the transmittance graph, the red line is the theoretical results obtained from the simulations, the short-dot and short-dash mean the +/- 10% of the thickness of the layers, the green line is the uncoated substrate experimental transmittance, and the blue line is the experimental data. Again, it is presented an inset graph that shows a zoom of the area of interest (850nm). As in the previous case, a comparative-temperature graph of transmittance for each AR design is presented (Figures 74, 78, and 82). One more time, for the reflectance graph, the yellow line is the theoretical simulated value, the green line the experimental data, and the purple line is the uncoated-substrate reflectance.

4.4.2.1.4 Al_2O_3-SiO_2 double-layer AR coating (second substrate face)

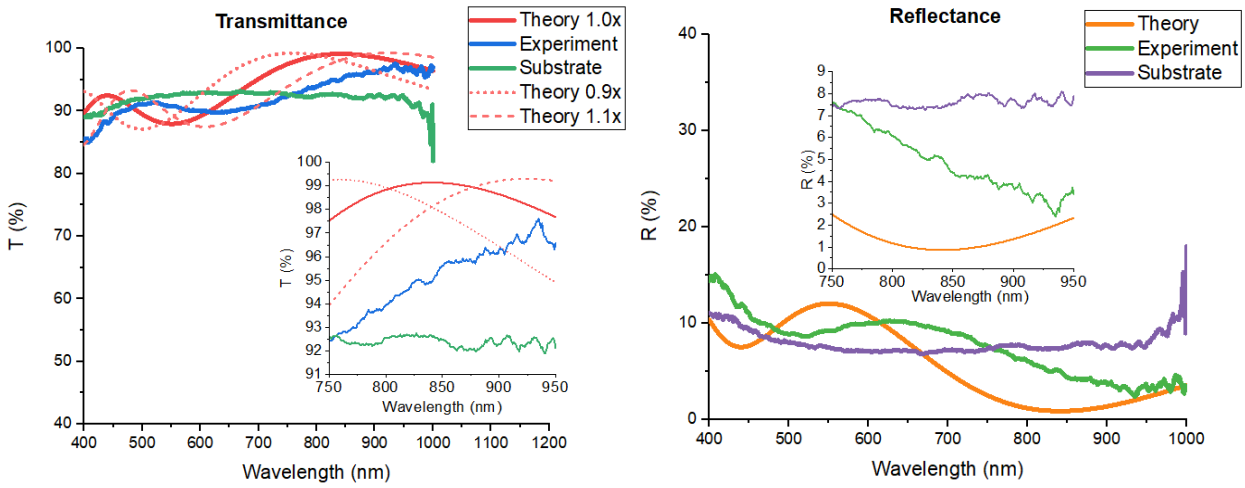

Figure 71 Transmittance and reflectance of Al_2O_3-SiO_2 double-layer AR coating at room temperature, deposited on the second face of the substrate.

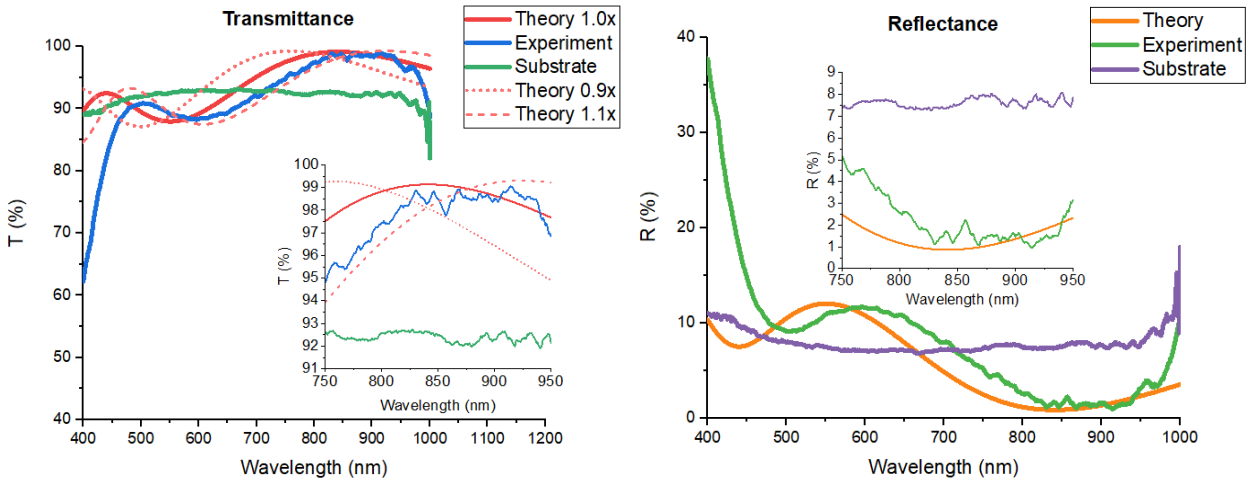

Figure 72 Transmittance and reflectance of Al_2O_3-SiO_2 double-layer AR coating at 100°C, deposited on the second face of the substrate.

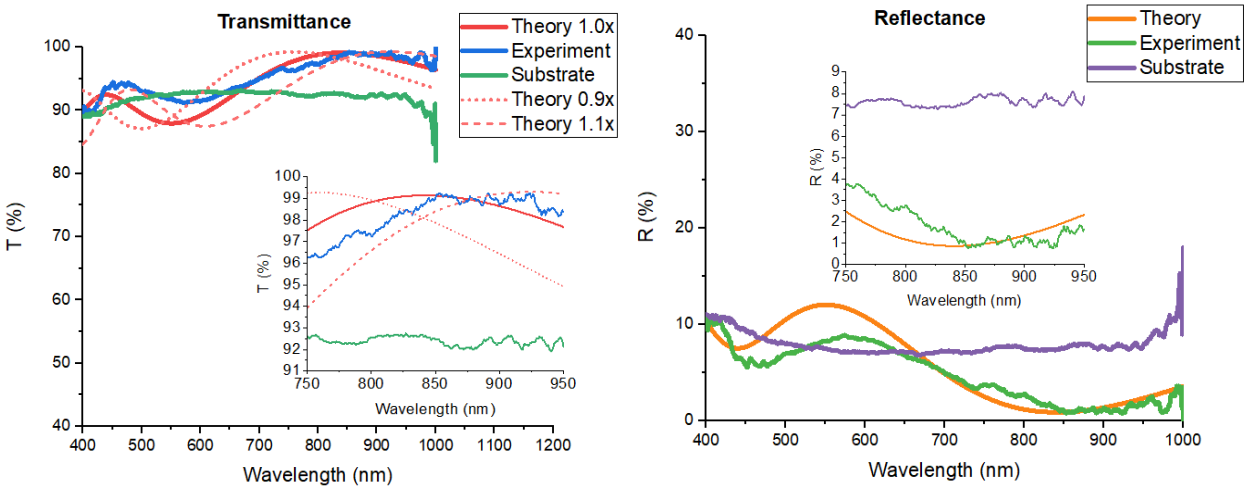

Figure 73 Transmittance and reflectance of Al_2O_3-SiO_2 double-layer AR coating at 200°C, deposited on the second face of the substrate.

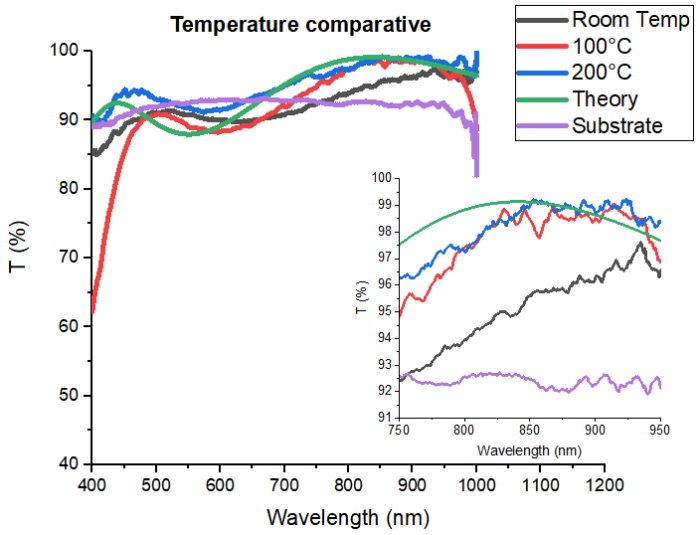

Figure 74 Temperature-comparative transmittance graph of Al_2O_3-SiO_2 double-layer AR coating.

Table 9 Comparison of values of transmittance of the Al_2O_3-SiO_2 double-layer AR coating at the reference wavelength for each substrate temperature.

SUBSTRATE SECOND FACE							
Design	**%T @ 850nm**						
	Theory	**Theory +10% Thickness**	**Theory -10% Thickness**	**Room Temperature**	**100°C**	**200°C**	**Uncoated Substrate**
2-Layer AR coating (Al_2O_3-SiO_2)	99.12	98.37	97.85	95.6	98.5	98.9	92.46

These results have the same behavior as the first-face ones, it was an improvement in the transmittance when you increase the temperature from room to 100°C, and there was no visible enhancement from the latter to the 200°C result. The reason for this was the same explained before: increasing in the mobility of the evaporated atoms because of the thermal energy can cause a better arrangement of the molecules; thus, a denser film. Besides, it probably is required a higher temperature to see substantial improvement from the 100°C result; values like 300°C or more may result in transmittances more matched to the ideal one.

In this case, there is not a peak of decrement around 910nm in the 200°C result. Just as before, the limit of measurement is close to the limit (1000 nm) and could be some instabilities. Besides, we must remember that the thermal evaporation technique is one of the less repeatable methods given the number of control variables.

4.4.2.1.5 SiO-SiO_2 double-layer AR coating (second substrate face)

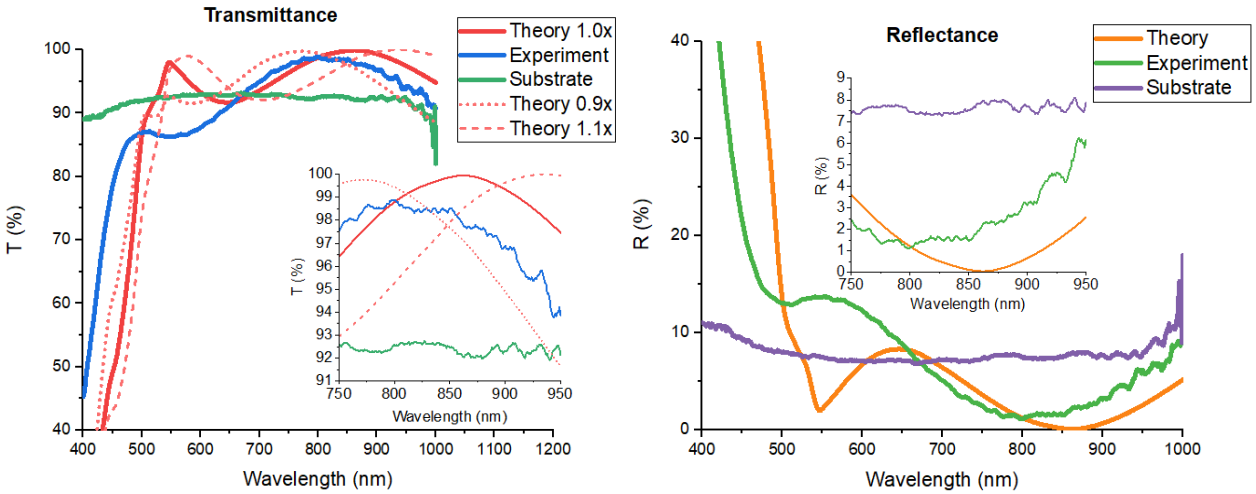

Figure 75 Transmittance and reflectance of SiO-SiO_2 double-layer AR coating <u>at room temperature</u>, now deposited on the second face of the substrate.

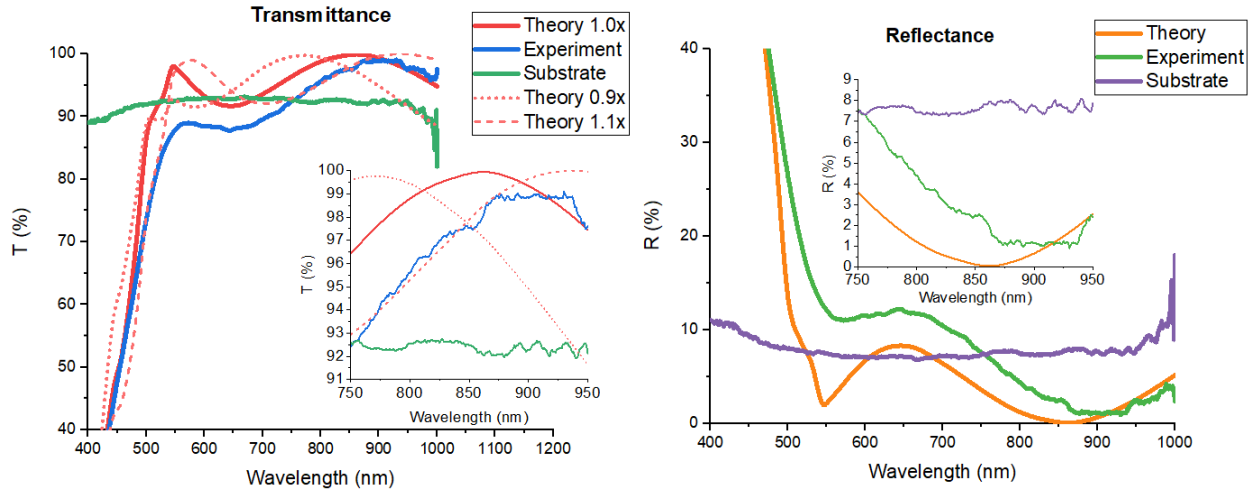

Figure 76 Transmittance and reflectance of SiO-SiO_2 double-layer AR coating <u>at 100°C</u>, now deposited on the second face of the substrate.

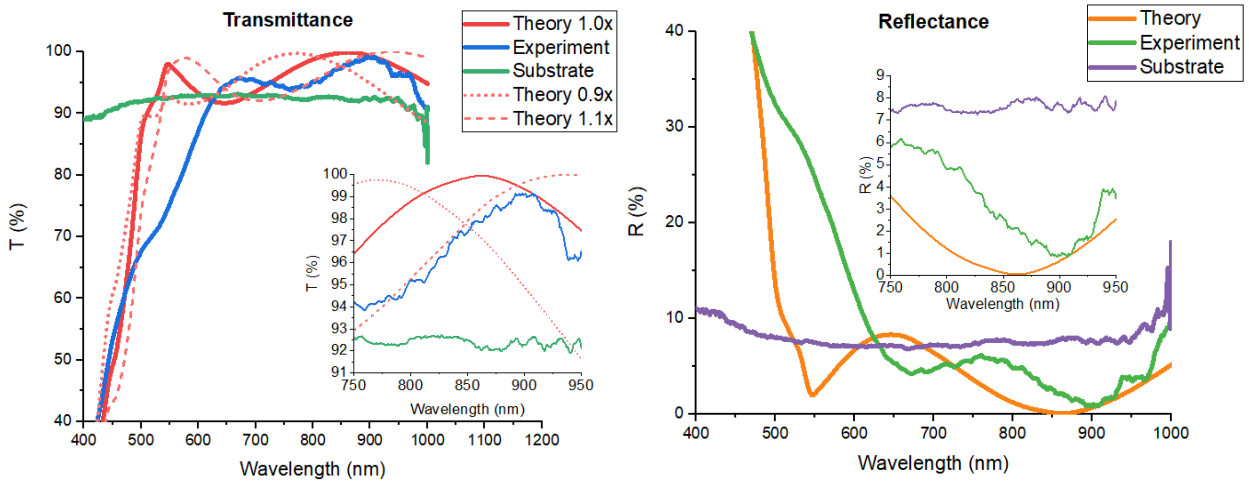

Figure 77 Transmittance and reflectance of SiO-SiO_2 double-layer AR coating at 200°C, now deposited on the second face of the substrate.

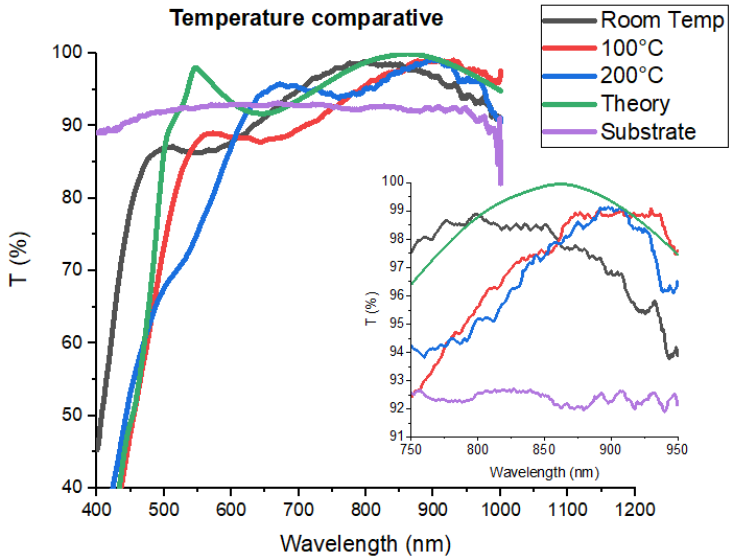

Figure 78 Temperature-comparative transmittance graph of SiO-SiO_2 double-layer AR coating.

Table 10 Comparison of values of transmittance of the SiO-SiO_2 double-layer AR coating at the reference wavelength for each substrate temperature.

SUBSTRATE SECOND FACE							
Design	**%T @ 850nm**						
	Theory	**Theory +10% Thickness**	**Theory -10% Thickness**	**Room Temperature**	**100°C**	**200°C**	**Uncoated Substrate**
2-Layer AR coating (SiO-SiO_2)	99.86	97.89	97.67	98.3	97.6	97.47	92.46

The experimental transmittance in Figures 75, 76, and 77 shows an interesting physical behavior in the transmittance's shape. On the one hand, the values of transmittance at 850nm are very similar, just like the results on the substrate's first face. However, the blue line at room temperature fits 90% of the thickness, while the 100°C and 200°C fit more with 110% of the thickness. In other words, those can be seen as a reference wavelength shift that may be caused for the moisture absorbed by the films on the first face of the substrate in the meantime of the deposition on the second face, due to small errors in thickness accumulated for both faces, or even a combination of both and this is the cause the shifts are not towards the same side.

4.4.2.1.6 Al_2O_3-SiO-SiO_2 triple-layer AR coating (second substrate face)

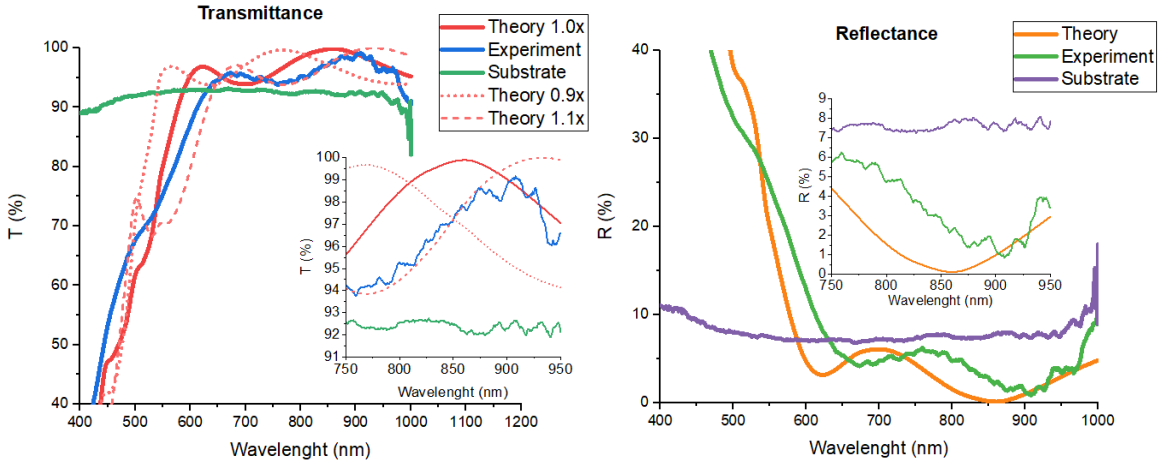

Figure 79 Transmittance and reflectance of Al_2O_3-SiO-SiO_2 triple-layer AR coating at room temperature, deposited on the second face of the substrate.

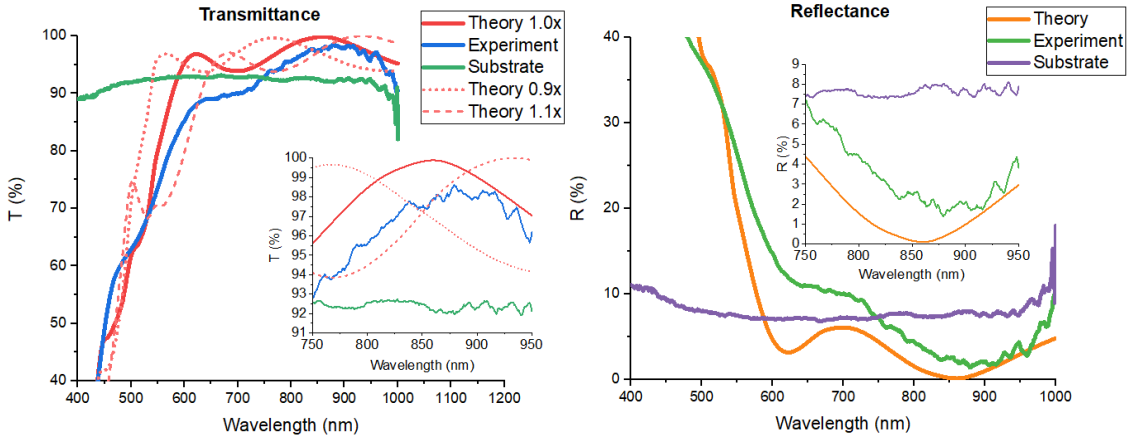

Figure 80 Transmittance and reflectance of Al_2O_3-SiO-SiO_2 triple-layer AR coating at 100°C, deposited on the second face of the substrate.

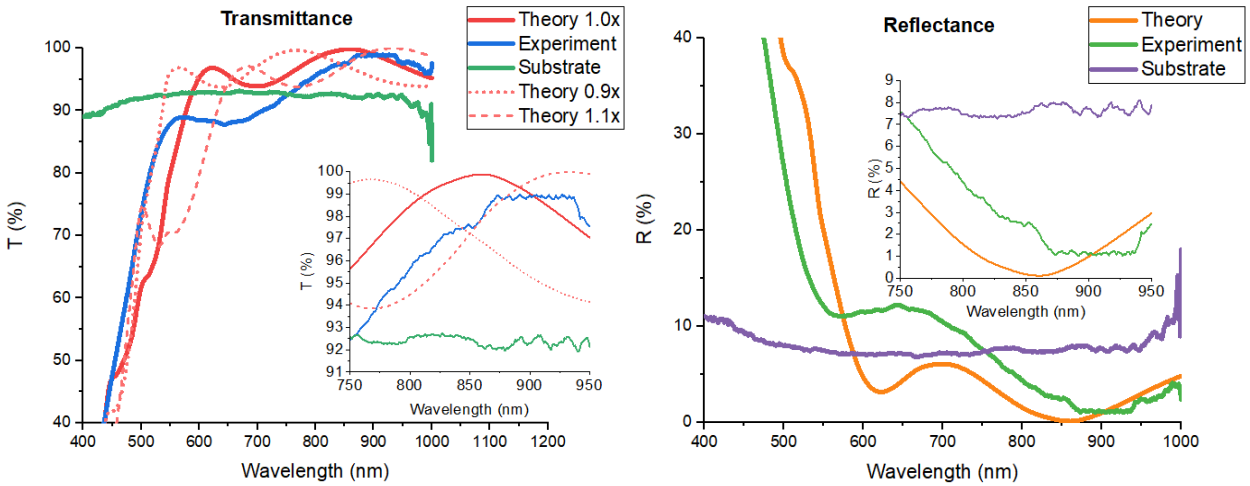

Figure 81 Transmittance and reflectance of Al_2O_3-SiO-SiO_2 triple-layer AR coating at 200°C, deposited on the second face of the substrate.

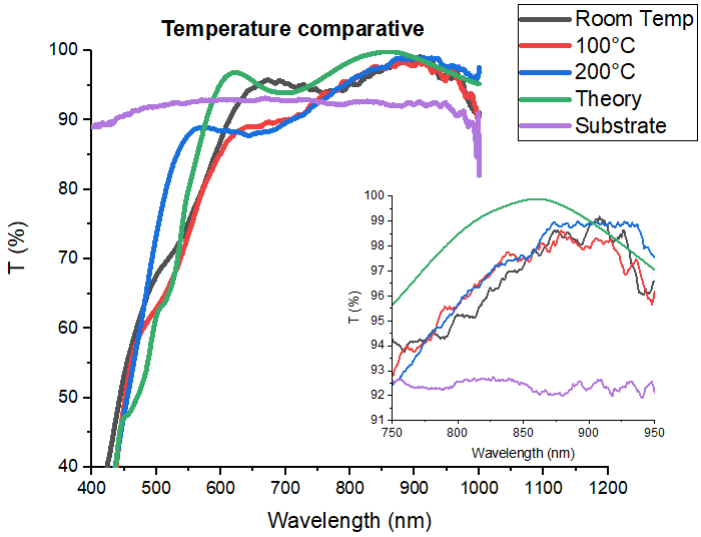

Figure 82 Temperature-comparative transmittance graph of Al_2O_3-SiO-SiO_2 triple-layer AR coating.

Table 11 Comparison of values of transmittance of the Al_2O_3-SiO-SiO_2 triple-layer AR coating at the reference wavelength for each substrate temperature.

SUBSTRATE SECOND FACE							
Design	**%T @ 850nm**						
	Theory	**Theory +10% Thickness**	**Theory -10% Thickness**	**Room Temperature**	**100°C**	**200°C**	**Uncoated Substrate**
3-Layer AR coating (Al_2O_3-SiO-SiO_2)	99.81	97.19	97.23	97.16	97.5	97.58	92.46

This design exhibits a similar phenomenon to the previous one: there was a reference wavelength shift probably caused by the moisture absorbed by the films on the first face of the substrate in the meantime of the deposition on the second face or by errors in the thickness accumulated by both faces due to the columnar growth. The difference is that all three shifts were towards the 110% of the thickness in this time. Thus, those shifts may be caused by moisture because the moisture tends to cause shifts towards longer wavelengths. In addition, this design also shows transmittance-behavior similar to the deposition on the first face of the substrate; the values of transmittance are similar despite the change in the temperature.

4.4.2.2 Corning Reynosa facilities

It has already been mentioned that the spectrometer used to characterize the reflectance of the four-layer broadband AR designs deposited in Reynosa was a Filmetrics F10. Figure 83 shows the experimental block diagram used to measure the samples' optical reflectance from 380 to 1700nm.

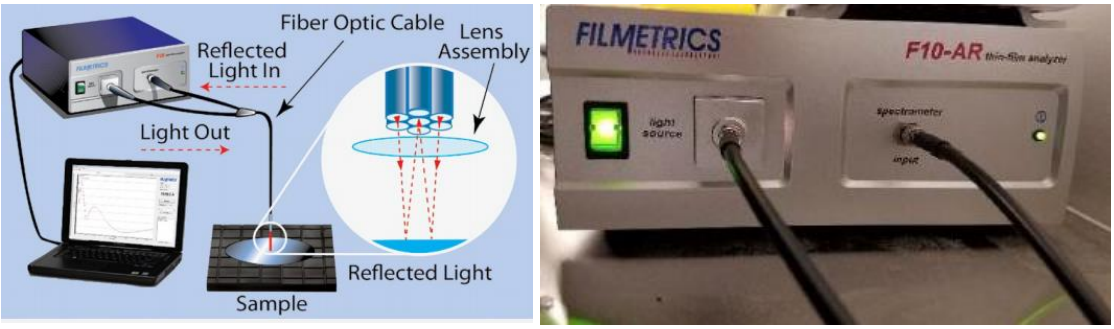

Figure 83 Reflectance characterization experimental block diagram (left) and an example of the equipment (right).

There were several depositions of the same design in order to check the repeatability of the IBAD equipment. Three deposits over a silica witness-substrate with one non-polished face and nine depositions over silica substrates with both polished faces. The results of these are shown in Figures 84 and 85. Figure 84 presents the results of reflectance characterization for the three iterations deposited on the witness-substrates. The solid lines are the measured experimental data, while the blue dashed line shows the theoretical results obtained from simulation. Also, a comparative table with values of reflectivity is shown (Table 13).

From the next results, we will appreciate that the IBAD machine has excellent repeatability in the depositions; all the solid-lines in the graphs are very similar but slightly different from the theory (dashed line), especially in the 1200 to 1400 nm zone. The process engineers in Corning Reynosa told us that a possible reason was that, given the long time between the four-layer coating was designed and it was fabricated (because of the quarantine), could have been some changes in the calibration of the machine and the refractive indexes of the pellets made of the selected materials. Unfortunately, given that both Corning Reynosa and I were behind schedule because of the quarantine, there was no time to optimize the four-layer design and fabricate new samples. That could be future work in this collaboration Corning-CICESE.

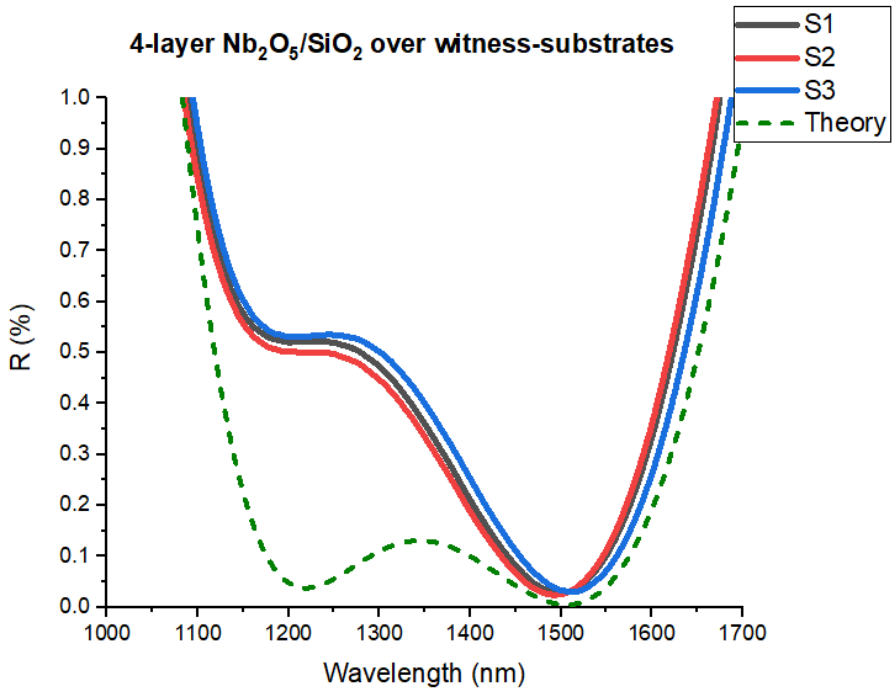

Figure 84 Results of reflectance characterization for the three iterations of the four-layer AR design deposited on the witness-substrates, and its comparison with theory. The witness substrates have one non-polished face to avoid backscattering and alter the reflectivity measurements.

Table 12 Comparison of values of reflectance for each iteration versus theory in 1310 and 1550nm.

Design	Wavelength	% R				
		Theory	S1	S2	S3	Uncoated Substrate
4-Layer AR coating (Nb_2O_5-SiO_2)	1310 nm	0.12	0.45	0.42	0.48	3.37
	1550 nm	0.05	0.1	0.11	0.07	

On the other hand, Figure 85 presents reflectance characterization results for the nine iterations deposited on the silica-substrates. The solid lines are the measured experimental data, while the orange-dashed line shows the theoretical results obtained from simulation. Besides, a comparative table with values of reflectivity is shown (Table 14).

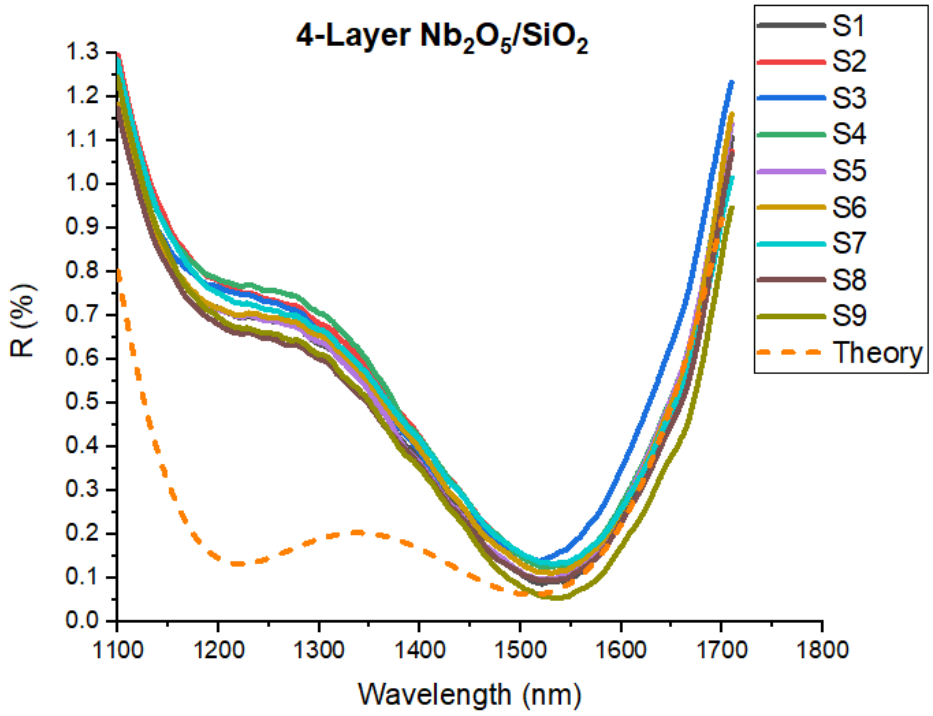

Figure 85 Results of reflectance characterization for the nine iterations of the four-layer AR design deposited on the silica-substrates, and its comparison with theory. These substrates have both faces polished.

Table 13 Comparison of values of reflectance for each iteration of Figure 85 versus theory in 1310 and 1550nm.

Design	Wavelength	% R										
		Theory	S1	S2	S3	S4	S5	S6	S7	S8	S9	Uncoated Substrate
4-Layer AR coating Nb_2O_5 - SiO_2	1310 nm	0.2	0.62	0.67	0.65	0.69	0.63	0.64	0.65	0.59	0.6	3.37
	1550 nm	0.08	0.09	0.13	0.18	0.13	0.11	0.12	0.14	0.1	0.07	

Thereby, this thesis has explored the possibility of use materials like SiO_x, Nb_2O_5, SiO, SiO_2, Al_2O_3, TiO_2, and MgF_2 on antireflective designs for optical communications. Besides, an approach to broaden the AR bandwidth by increasing the number of layers deposited on a substrate. In addition, two different techniques to deposit AR coatings were studied. If the target of these coating is the optical communication devices, they must accomplish several commercial standards. It is needed to define the correct synthesis parameters and the most suitable deposition technique, e. g. IBAD or IBS to obtain the results worthy of the current optical coatings' market.

Chapter 5. Conclusions and future work

When your stock of materials is short, and you need a wide range of different refractive indices, a modulation of the SiO_x may be a good option. Thus, you can obtain a range from 1.47 to 1.92, approximately. This work has studied the use of SiO_x thin films on AR coatings designed for several zones of the electromagnetic spectra: 850nm and a range from 1200 to 1600nm to cover the lines of 1310 and 1550 nm. Therefore, the three fiber optical communication lines (850, 1310, and 1500 nm) were included.

The need for different source materials with different refractive indices increases as the number of layers deposited on a substrate. For example, for triple-layer designs, you need at least a low-index material, a high-index, and an intermediate-index material. This is the reason the target refractive indices of SiO_x thin films were delimited by the maximum (~SiO, n=1.92), minimum (~SiO_2, n=1.47), and some approximate intermediate value (~Al_2O_3, n=1.65). For four-layer and five-layer designs, one can use either several refractive indices or only an alternation of high- and low-index, which was the case for this work.

Also, the contrast between the refractive indices is important to get low reflectance and wide bandwidth. The literature says that the higher the difference, the flatter the reflectance curve. Regarding SiO_x thin films, the maximum contrast is given by the silica (n=1.47) and silicon monoxide (n=1.92). For this reason, the simulation of the two-layer SiO-SiO_2 design has a better AR effect than the two-layer Al_2O_3-SiO_2 one.

Regarding AR designs, especially the simulation section showed that the non-multiple of $\lambda/4$ layers tend to have better antireflective results, mostly due to their non-self-limitation when seen from the admittance diagram. That means the sections of the circles can be shorted or increased in order to finish as close as the admittance of the incident media is possible. Thus, improve the AR effect.

Based on the experimental results presented, it has been found that when using the thermal evaporation technique and manipulating fabrication parameters like deposition rate, chamber pressure, and reactive atmosphere, it is possible to modulate the resulting refractive index of the deposited film. These SiO_x films have been widely studied before but never used on AR coatings. So, this thesis work has helped to establish some basic parameters to control and produce AR coatings based on SiO_x films; there is still a lot of work and research to do on this application. For example, increase the exploration of SiO_x thin films synthesized by thermal evaporation or another technique and use them on AR coating. So far, we have not found works with SiO_x thin films used for AR purposes.

Nevertheless, because of the nature of the thermal evaporation technique, there will be a columnar growth of the films, causing poor packaging density of the coating and the potential absorption of moisture

when it is present. From the results of the designs deposited in CICESE on the second face of the substrate, this phenomenon could be seen as a shift in the reference wavelength. For this reason, energetic techniques like IBAD used in Corning Reynosa disrupt the columnar structure of the films and increase the density of the films even at low temperatures; this was evident in the results presented of the four-layer design made of Nb_2O_5 and SiO_2 fabricated in Reynosa, each iteration of the deposit was remarkably similar to the previous one, and the values of reflectance, especially at 1550nm were pretty similar to the theoretical ones.

Therefore, it can be concluded that it is possible to use the SiO_x thin films on AR designs. It is possible to produce good optical performance (refractive index, thickness, and spectral transmittance) when they are synthesized by thermal evaporation. However, given the limitations of this technique, some mechanical features will be compromised, like low packaging density and abrasion, high tensile stress, and poor adhesion. As could be seen in the results presented here, increasing the substrate's temperature is another way to enhance the spectral transmittance. Still, maybe higher values, like 300°C or more may be needed to get substantial improvements. Several references say that performing annealing after the deposition by thermal evaporation can improve several of the mentioned mechanical characteristics. However, this is out of the scope of this thesis. Thus, another future recommended work for this project could use higher substrate temperatures and a study of annealing when using thermal evaporation. Also, the optimization of the whole set of fabricated designs, looking for better AR results.

Bibliography

Agrell, E., Karlsson, M., Chraplyvy, A. R., Richardson, D. J., Krummrich, P. M., Winzer, P., Roberts, K., Fischer, J. K., Savory, S. J., Eggleton, B. J., Secondini, M., Kschischang, F. R., Lord, A., Prat, J., Tomkos, I., Bowers, J. E., Srinivasan, S., Brandt-Pearce, M., Gisin, N. 2016. Roadmap of optical communications. Journal of Optics (United Kingdom), 18(6). doi:10.1088/2040-8978/18/6/063002

Azzam, R. M. A. 1995. Ellipsometry. In Handbook of Optics, Volume II (2nd ed.). from http://photonics.intec.ugent.be/education/IVPV/res_handbook/v2ch27.pdf

Bashir Khan, S., Wu, H., Pan, C., Zhang, Z. 2017. A Mini Review: Antireflective Coatings Processing Techniques, Applications and Future Perspective. Research & Reviews: Journal of Material Sciences, 05(06), 36–54. doi:10.4172/2321-6212.1000192

Carneiro, J. O., Machado, F., Rebouta, L., Vasilevskiy, M. I., Lanceros-Méndez, S., Teixeira, V., Costa, M. F., Samantilleke, A. P. 2019. Compositional, optical and electrical characteristics of SiOx thin films deposited by reactive pulsed DC magnetron sputtering. Coatings, 9(8). doi:10.3390/coatings9080468

Cox, J. T., Hass, G., Thelen, A. 1962. Triple-Layer Antireflection Coatings on Glass for the Visible and Near Infrared. Journal of the Optical Society of America, 52(9), 965. doi:10.1364/josa.52.000965

Dash, J. K., Chen, L., Topka, M. R., Dinolfo, P. H., Zhang, L. H., Kisslinger, K., Lu, T. M., Wang, G. C. 2015. A simple growth method for Nb2O5 films and their optical properties. RSC Advances, 5(45), 36129–36139. doi:10.1039/c5ra05074j

Dobrowolski, J. A. 1995. Optical Properties of Films and Coatings. In Handbook of Optics, Volume I (2nd ed.). from http://linkinghub.elsevier.com/retrieve/pii/S0925346701001768

Doshi, Y. 2017. Antireflective Coatings Market by Technology (Vacuum Deposition, Electronic Beam Evaporation, Sputtering, and Others) and Application (Eyewear, Electronics, Solar Panels, Automobile, and Others) - Global Opportunity Analysis and Industry Forecast, 2014-20. Consultado January 21, 2020, from Market Research Report website: https://www.alliedmarketresearch.com/anti-reflective-coatings-market

Durrani, S. M. A., Al-Kuhaili, M. F., Khawaja, E. E. 2003. Characterization of thin films of a-SiOx (1.1 < x < 2.0) prepared by reactive evaporation of SiO. Journal of Physics Condensed Matter, 15(47), 8123–8135. doi:10.1088/0953-8984/15/47/015

Gao, L., Lemarchand, R., Lequime, M. 2013. Refractive index determination of SiO2 layer in the UV/Vis/NIR range: Spectrophotometric reverse engineering on single and bi-layer designs. Journal of the European Optical Society, 8, 13010. doi:10.2971/jeos.2013.13010

Hass, G., Salzberg, C. 1954. Optical Properties of Silicon Monoxide in the Wavelength Region from 0.24 to 14.0 Microns. Journal of the Optical Society of America, 44, 181–187.

Hedayati, M. K., Elbahri, M. 2016. Antireflective coatings: Conventional stacking layers and ultrathin plasmonic metasurfaces, a mini-review. Materials, 9(6). doi:10.3390/ma9060497

Kaiser, N., Pulker, H. 2003. Optical Interference Coatings. In Optical Interference Coatings.

Larouche, S., Martinu, L. 2008. OpenFilters: Open-source software for the design, optimization, and synthesis of optical filters. Applied Optics, 47(13). doi:10.1364/AO.47.00C219

Lemarchand, F. 2013. Optical Constants of Nb2O5. from RefractiveIndex.INFO website: https://refractiveindex.info/?shelf=main&book=Nb2O5&page=Lemarchand

Lemarquis, F., Begou, T., Moreau, A., Lumeau, J. 2019. Broadband antireflection coatings for visible and infrared ranges. CEAS Space Journal, 11(4), 567–578. doi:10.1007/s12567-019-00266-8

Liou, Y. Y., Wei, Z., Wang, L. R., Liu, W. L., Liu, C. C. 2009. Optimization of broadband visible or near infrared antireflection coating design by scanning search method. Japanese Journal of Applied Physics, 48(1). doi:10.1143/JJAP.48.012502

Lizarraga-Medina, E. G., Oliver, A., Vázquez, G. V., Salas-Montiel, R., Márquez, H. 2015. Design of SiOx slab optical waveguides. Nanoengineering: Fabrication, Properties, Optics, and Devices XII, 9556(3918), 95560H. doi:10.1117/12.2187121

Lizarraga-Medina, Eder G., Salazar, D., Vázquez, G. V., Salas-Montiel, R., Nedev, N., Márquez, H. 2016. Study of SiOx (1<x<2) Thin Film Optical Waveguides. Journal of Lightwave Technology, PP(99), 4926–4932. doi:10.1109/JLT.2016.2610862

MacLeod, H. A. 2001. Thin-Film Optical Filters. In Thin-Film Optical Filters. doi:10.1201/9781420033236

Martín-Palma, R. J., Lakhtakia, A. 2013. Vapor-Deposition Techniques. In Engineered Biomimicry. doi:10.1016/B978-0-12-415995-2.00015-5

Martin, P. M. 2010. Ion Plating. In Handbook of Deposition Technologies for Films and Coatings (Third Edit). doi:10.1016/B978-0-8155-2031-3.00006-5

Materion. 2000. Silicon Dioxide SiO2 for Optical Coating. from Coating Materials News 2000 to 2010 website: https://materion.com/resource-center/newsletters/newsletter-archives/coating-materials-news-2000-to-2010/silicon-dioxide-sio2-for-optical-coating

Mattox, D. M. 2009. Handbook of Physical Vapor Deposition (PVD) Processing. doi:10.1016/B978-0-8155-2037-5.00025-3

O'Leary, M. J., Thomas, J. H. 1987. Characterization of reactively evaporated SiO x thin films . Journal of Vacuum Science & Technology A: Vacuum, Surfaces, and Films, 5(1), 106–109. doi:10.1116/1.574142

Ohlídal, I., Vohánka, J., Buršíková, V., Franta, D., Čermák, M. 2020. Spectroscopic ellipsometry of inhomogeneous thin films exhibiting thickness non-uniformity and transition layers. Optics Express, 28(1), 160. doi:10.1364/oe.28.000160

Pellicori, S. 1984. Materials & Deposition Technology for Coating Optical Surfaces. Materion Coating Materials News.

Piegari, A., Flory, F. 2013. Optical thin films and coatings: From materials to applications. In Optical Thin Films and Coatings: From Materials to Applications. doi:10.1016/C2016-0-02583-4

Regnima, G.-O., Koffi, T., Bagui, O., Kouacou, A., Kristensson, E., Zoueu, J., Berrocal, E. 2017. Quantitative measurements of turbid liquids via structured laser illumination planar imaging where absorption spectrophotometry fails. Applied Optics, 56(13), 3929. doi:10.1364/ao.56.003929

Salazar, D., Soto-Molina, R., Lizarraga-Medina, E. G., Felix, M. A., Radnev, N., Márquez, H. 2016. Ellipsometric Study of SiOx Thin Films by Thermal Evaporation. Open Journal of Inorganic Chemistry, 06(03), 175–182. doi:10.4236/ojic.2016.63013

Santecchia, E., Hamouda, A. M. S., Musharavati, F., Zalnezhad, E., Cabibbo, M., Spigarelli, S. 2015. Wear resistance investigation of titanium nitride-based coatings. Ceramics International, 41(9), 10349–10379. doi:10.1016/j.ceramint.2015.04.152

Shabalov, A. L., Feldman, M. S. 1983. Optical and dielectric properties of thin SiOx films of variable composition. Thin Solid Films, 110(3), 215–224. doi:10.1016/0040-6090(83)90239-0

Syed, W. A. A., Rafiq, N., Ali, A., Din, R. ud, Shah, W. H. 2017. Multilayer AR coatings of TiO2/MgF2 for application in optoelectronic devices. Optik, 136(February), 564–572. doi:10.1016/j.ijleo.2017.02.085

Thetford, A. 1968. Four-Layer Coating Design. University of Reading, UK Private Communication.

Thetford, A. 1969. A Method of Designing Three-layer Anti-reflection Coatings. Optica Acta, 16(1), 37–43. doi:10.1080/713818145

Usha, N., Sivakumar, R., Sanjeeviraja, C., Arivanandhan, M. 2015. Niobium pentoxide (Nb2O5) thin films: Rf Power and substrate temperature induced changes in physical properties. Optik, 126(19), 1945–1950. doi:10.1016/j.ijleo.2015.05.036